

AD-A260 003



ESL-TR-90-32

2

# THREE-DIMENSIONAL MODELING OF ROCKET PROPELLANT DISPERSION

T. YAMADA, S. BUNKER

LOS ALAMOS NATIONAL LABORATORY  
P. O. BOX 1663  
LOS ALAMOS NM 87545

SEPTEMBER 1991

FINAL REPORT

MAY 1988 - APRIL 1991

APPROVED FOR PUBLIC RELEASE. DIS-  
TRIBUTION UNLIMITED.

DTIC  
ELECTE  
FEB 1 1993  
S C D



394 665  
AFESC/ESL  
93-01770



AIR FORCE ENGINEERING & SERVICES CENTER  
ENGINEERING & SERVICES LABORATORY  
TYNDALL AIR FORCE BASE, FLORIDA 32403

NOTICE

PLEASE DO NOT REQUEST COPIES OF THIS REPORT FROM  
HQ AFESC/RD (ENGINEERING AND SERVICES LABORATORY).  
ADDITIONAL COPIES MAY BE PURCHASED FROM:

NATIONAL TECHNICAL INFORMATION SERVICE  
5285 PORT ROYAL ROAD  
SPRINGFIELD, VIRGINIA 22161

FEDERAL GOVERNMENT AGENCIES AND THEIR CONTRACTORS  
REGISTERED WITH DEFENSE TECHNICAL INFORMATION CENTER  
SHOULD DIRECT REQUESTS FOR COPIES OF THIS REPORT TO:

DEFENSE TECHNICAL INFORMATION CENTER  
CAMERON STATION  
ALEXANDRIA, VIRGINIA 22314

## REPORT DOCUMENTATION PAGE

Form Approved  
OMB No 0704-0184

1a. REPORT SECURITY CLASSIFICATION <b>Unclassified</b>			1b. RESTRICTIVE MARKINGS		
2a. SECURITY CLASSIFICATION AUTHORITY			3. DISTRIBUTION/AVAILABILITY OF REPORT Approved for Public Release Distribution Unlimited		
2b. DECLASSIFICATION/DOWNGRADING SCHEDULE					
4. PERFORMING ORGANIZATION REPORT NUMBER(S)			5. MONITORING ORGANIZATION REPORT NUMBER(S)  ESL-TR-90-32		
6a. NAME OF PERFORMING ORGANIZATION Los Alamos National Laboratory		6b. OFFICE SYMBOL (if applicable)	7a. NAME OF MONITORING ORGANIZATION Air Force Engineering and Services Center		
6c. ADDRESS (City, State, and ZIP Code) P. O. Box 1663 Los Alamos, New Mexico 87545			7b. ADDRESS (City, State, and ZIP Code) H. Q. AFESC/RDVS Tyndall Air Force Base, FL 32403-6001		
8a. NAME OF FUNDING/SPONSORING ORGANIZATION		8b. OFFICE SYMBOL (if applicable)	9. PROCUREMENT INSTRUMENT IDENTIFICATION NUMBER		
8c. ADDRESS (City, State, and ZIP Code)			10. SOURCE OF FUNDING NUMBERS		
			PROGRAM ELEMENT NO.	PROJECT NO.	TASK NO.
			WORK UNIT ACCESSION NO.		
11. TITLE (Include Security Classification)  Three-Dimensional Modeling of Rocket Propellant Dispersion					
12. PERSONAL AUTHOR(S) Yamada, T., Bunker S.					
13a. TYPE OF REPORT Final		13b. TIME COVERED FROM May 88 TO Apr 91		14. DATE OF REPORT (Year, Month, Day) September 1991	
15. PAGE COUNT					
16. SUPPLEMENTARY NOTATION  Availability of this report is specified on reverse of front cover					
17. COSATI CODES			18. SUBJECT TERMS (Continue on reverse if necessary and identify by block number) Dispersion on Coastal Complex, Emergency Response Modeling, Three-Dimensional Forecast Models, HOTMAC, RAPTAD		
FIELD	GROUP	SUB-GROUP			
19. ABSTRACT (Continue on reverse if necessary and identify by block number)  The purpose of this study was to demonstrate the feasibility of using a small computer to operate a three-dimensional atmospheric model to forecast the transport and dispersion of airborne hazardous materials at Vandenberg Air Force Base (VAFB). The contractor investigated the feasibility of using the three-dimensional atmospheric models HOTMAC (Higher Order Turbulence Model for Atmospheric Circulations) and RAPTAD (Random Puff Transport and Diffusion) to meet the objective of the project. HOTMAC is a mesoscale atmospheric model that can forecast three-dimensional distributions of wind speed, wind direction, turbulence, temperature, and water vapor. RAPTAD is a Lagrangian puff code based on the Monte Carlo statistical diffusion process. The center location and standard deviation of concentration distribution for each puff are computed by use of wind and turbulence modeled by HOTMAC. Then concentration at any location is computed by summation of concentrations contributed					
20. DISTRIBUTION/AVAILABILITY OF ABSTRACT <input type="checkbox"/> UNCLASSIFIED/UNLIMITED <input checked="" type="checkbox"/> SAME AS RPT. <input type="checkbox"/> DTIC USERS			21. ABSTRACT SECURITY CLASSIFICATION Unclassified		
22a. NAME OF RESPONSIBLE INDIVIDUAL Captain Michael Moss			22b. TELEPHONE (Include Area Code) 904-283-4234		22c. OFFICE SYMBOL HQ AFESC/RDVS

by all the puffs. To test the feasibility of operating HOTMAC/RAPTAD with the VAFB terrain, we selected data from the Mountain Iron (MI) diffusion experiments, which were conducted at VAFB during 1965 and 1966. Conclusions of this study include: HOTMAC and RAPTAD predictions were as good as those obtained by diagnostic models and they were the best practical solution where wind data were not available. The HOTMAC and RAPTAD modeling system would be a useful addition to enhance current VAFB emergency response management capabilities. It is feasible to incorporate the positive and negative source buoyancy effects in HOTMAC and RAPTAD. Our approach can minimize the ambiguities and inconsistencies introduced in a simple plume-rise model.

## EXECUTIVE SUMMARY

DATA QUALITY INSPECTED 3

### OBJECTIVE

The purpose of this study was to demonstrate the feasibility of using a small computer to operate a three-dimensional atmospheric model to forecast the transport and dispersion of airborne hazardous materials at Vandenberg Air Force Base (VAFB).

### BACKGROUND

Air Force (AF) models, designed to calculate atmospheric transport and dispersion at VAFB, assume that the wind field over the geographical area of interest can be adequately represented by the wind speed and direction measured at a single point or by a vertical profile of wind speed and direction over a single site. While such an assumption is acceptable over flat terrain and over a short time, the complex terrain and meteorology at VAFB and the reduction in personal exposure limits for the AF chemicals of interest require that more accurate methods be used to make these calculations.

Current efforts to improve VAFB's modeling capability also assume the three-dimensional wind field can be represented by a single wind value. The complexity of the terrain and meteorology at VAFB require a model that takes into account the three-dimensional wind field over the entire VAFB region.

Recent advancements in computer hardware technology, however, have the potential to allow much more sophisticated models to be operated in much less time than previously considered possible. The contractor investigated the feasibility of using the three-dimensional atmospheric models HOTMAC (Higher Order Turbulence Model for Atmospheric Circulations) and RAPTAD (Random Puff Transport and Diffusion) to meet the objective of the project.

### TASKS

The specific tasks are described in Section II. The first task was to prepare input files for HOTMAC and RAPTAD. The input data included digitized terrain elevations, initial wind and potential temperature distributions, and the surface condition. The main task was to operate HOTMAC/RAPTAD with VAFB terrain data and compare output with the observations and that obtained by AF models. The contractor operated the HOTMAC/RAPTAD model on a MicroVax and a Sun work station. Finally, the contractor investigated the feasibility of incorporating positive and negative source buoyancy effects in HOTMAC and RAPTAD.

### METHODOLOGY

Section III reviewed briefly the model equations, boundary conditions, and numerical schemes used in HOTMAC and RAPTAD. A detailed model description is given in Appendix A.

HOTMAC is a mesoscale atmospheric model that can forecast three-dimensional distributions of wind speed, wind direction, turbulence, temperature, and water vapor. The basic

equations for HOTMAC are the conservation equations for mass, momentum, internal energy, mixing ratio of water vapor, and turbulence kinetic energy.

RAPTAD is a Lagrangian puff code based on the Monte Carlo statistical diffusion process. The center location and standard deviation of concentration distribution for each puff are computed by use of wind and turbulence modeled by HOTMAC. Then, concentration at any location is computed by summation of concentrations contributed by all the puffs. RAPTAD can be used under extreme conditions with highly heterogeneous wind and turbulence distributions where a convectional Gaussian plume model may fail.

## TEST DESCRIPTION

To test the feasibility of operating HOTMAC/RAPTAD with the VAFB terrain, we selected data from the Mountain Iron (MI) diffusion experiments, which were conducted at VAFB during 1965 and 1966. The objective of the MI program was to establish quantitative diffusion predictions for use as range safety tools in the South Vandenberg (SV) ballistic and space vehicle operations area.

Meteorological masts were deployed to measure wind speeds and wind directions. These wind data were used to examine the performance of HOTMAC. Vertical profiles of wind speed, wind direction, and wet and dry temperature up to 2000 meters above the ground were measured by rawinsondes at four sites, and wind profiles were taken by a wiresonde at the tracer release site. The vertical profiles of winds and temperatures were used to initialize the model variables and test the model predictions.

Fluorescent particles were released to aid the understanding of transport and diffusion processes and the derivation of an empirical formula for the pollutant concentration distribution in the SV area.

A total of 113 tracer releases were made, from which we selected the MI87, MI90, and MI91 cases to evaluate the performance of HOTMAC and RAPTAD.

## RESULTS

### MI87 Simulation

The meteorological condition for the MI87 case was characterized as "weak ambient and sea-breeze flow, with little distinction between wind vectors, but sharp cooling with fog rolling in."

The initial HOTMAC potential temperature profile was determined by averaging four upper air soundings at 1300 local standard time (1st). The potential temperature profile was approximately  $0.044^{\circ}\text{C}/\text{m}$  from the sea surface to 460 meters above mean sea level (msl),  $0.0142^{\circ}\text{C}/\text{m}$  between 460 meters and 960 meters above msl, and  $0.0045^{\circ}\text{C}/\text{m}$  above 960 meters above msl. Initial wind speed and direction were determined by examining five upper air soundings at 1300 1st. Initial upper air wind speed and wind direction above the boundary layer were estimated to be 2 m/s and 225 degrees, respectively.

The computational domain was  $40 \times 48 \text{ km}^2$  with a horizontal grid spacing of 1 km. To resolve the details of topography in the vicinity of the tracer release site, we nested a fine-resolution grid  $15 \times 16 \text{ km}^2$  with a horizontal grid spacing of 0.5 km.

Integration started at 0500 lst, June 13, 1966, and continued for over 12 hours. The plume was released at 1310 lst for 30 minutes as was done in the experiment. The plume was followed for 4 hours in the model computation. By that time, the plume was transported far away from the sampling areas.

The modeled horizontal wind vectors at 10 meters above the ground at 1300 lst, June 13, 1966 were in good agreement with the observed winds in the surface layer, although observed wind vectors show considerable variation in direction and magnitude compared with modeled winds.

Less satisfactory results were obtained when vertical profiles of the modeled wind speed and wind direction were compared with observations. Wind speed and wind direction become highly variable in space and time when wind speed is small. It should be noted that the observations were instantaneous values whereas the modeled results were ensemble averages.

The ground-level exposure values were computed by integrating concentration with time until the concentration became negligible. Although the modeled plume direction did not exactly match the observed one, the modeled ground-level exposures along the plume axis were in good agreement with observations.

#### MI90 Simulation

Meteorological conditions for the MI90 case were significantly different from those for the MI87 case. The prevailing wind speed for MI90 was close to 13.5 m/s compared with 2 m/s for MI87. In addition, for MI90 a deep, well-mixed layer existed for the first 500 meters above the ground, which probably resulted from strong mixing caused by turbulence generated by high winds. The potential temperature profiles for MI87 exhibited shallow (100 meters) mixed-layer depths that are typical on the west coast as a result of large-scale subsidence.

The initial potential temperature profile was determined from the sounding at the Building 22 site. The potential temperature lapse rate was almost neutral ( $0.0002 \text{ }^\circ\text{C/m}$ ) from the surface to 670 meters above msl,  $0.0611 \text{ }^\circ\text{C/m}$  between 670 meters and 880 meters above msl, and  $0.0070 \text{ }^\circ\text{C/m}$  above 880 meters above msl. Initial wind speed (13.5 m/s) and direction (332 degrees) were determined by examination of three upper air soundings.

Integration started at 0600 lst, June 21, 1966 and continued for 24 hours until 0600 lst the following day. The plume was released for 30 minutes starting at 2300 lst, June 21, 1966. The plume was sampled for 2 hours in the model computation. By this time the plume had left the computational domain, and the surface concentration values were practically zero.

With the wind and turbulence distributions computed by HOTMAC, RAPTAD simulated the ground-level exposure values which were in good agreement with the observations. The observed exposures at 1870 and 5620 meters from the source were  $5.08 \times 10^{-6}$

and  $4.97 \times 10^{-7} \text{ s/m}^3$ , respectively. The corresponding modeled values at 1895 and 5603 meters from the source were  $1.83 \times 10^{-6}$  and  $3.45 \times 10^{-7} \text{ s/m}^3$ , respectively.

### MI91 Simulation

The MI91 release was at 0203 lst, June 22, 1966 which was only 3 hours after the MI90 release. However, the wind direction changed considerably to northerly, as much as 30 degrees from the MI90 case. Based on the MI91 data log, the wind direction veering from northwest to north occurred around midnight June 21, 1966, and was most evident in the layers between 300 and 1300 meters above msl.

Wind directions at the grid levels between 300 and 1300 meters above msl were nudged toward the observed wind directions. We started the HOTMAC computation with wind direction nudging, using the output at 2300 from the MI 90 simulation to initialize the model variables.

The modeled horizontal wind vectors clearly indicated that the wind directions shifted from the corresponding values for the MI90 case. The nudging was not applied to the layers in the first 300 meters above the ground but the surface layer winds were clearly influenced by the nudging. This good communication between the surface and upper level winds apparently resulted from the strong vertical mixing resulting from extraordinary large turbulence for a nocturnal period. The high prevailing wind speed (13.5 m/s) was responsible for the large turbulence values.

### Model Comparisons

There were a few attempts in the past to simulate the MI wind and concentration data. Hunter (Reference 12) investigated the performance of a diagnostic wind model WOCSS for eight cases of the MI data. Thykier—Nielsen et al. (Reference 13) tested a diagnostic wind model (LINCOM) and a puff model (RIMPUFF) for two cases of the MI data. The data common to both studies were the MI87 and MI90 cases. Therefore, we used these two cases to compare the performances of WOCSS, LINCOM, RIMPUFF, HOTMAC, and RAPTAD, and discussed the strengths and weaknesses of each model.

### Application on Desktop Computers

Recent advances in desktop computer capabilities, particularly those of an engineering workstation, are astonishing. A high-performance workstation has reportedly exceeded a super-computer in certain scalar operations. The affordability and portability of the desktop computer have opened the door to many applications that were previously considered impossible.

One logical application is upgrading toxic-hazard modeling capabilities for emergency response management. Scientists at Los Alamos National Laboratory are in the process of developing three-dimensional forecasting models that run on a desktop computer.

In this section we discussed our experience in running HOTMAC and RAPTAD on a Sun Microsystems workstation and a MicroVax computer.



## Buoyant Plumes

In this section, we investigated the feasibility of incorporating positive and negative source buoyancy effects in HOTMAC and RAPTAD.

The most widely used method to treat a buoyant plume is to use a plume rise theory advanced by Briggs (Reference 14). One can estimate the height where the plume levels off. This height is referred to as an effective stack height. Therefore, the simplest way to deal with a buoyant plume is to apply the Brigg's formula in the initial stage when the buoyancy effect is significant. When the plume becomes neutrally buoyant, RAPTAD can be applied as before except that a stack height is replaced by an effective stack height.

Our approach is quite different from that of a plume rise model. We specify a heat source as a boundary condition, then the governing equations in HOTMAC compute wind, temperature, and turbulence distributions. RAPTAD uses these HOTMAC variables to determine the centroid location and size of each puff. Unlike a plume rise model, a puff in RAPTAD is a tracer that follows precisely the turbulent fluid motion. Our approach, in this study, is referred to as a "dynamic plume model." The advantage of a dynamic plume model is that the fluid motions and turbulent processes are consistent with the physical laws expressed by the governing equations. In other words, we can minimize the ambiguities and inconsistencies introduced in a passive plume model. For example, methods used in a passive plume model to parameterize turbulent entrainment processes are based on simple and idealized conditions. A passive plume model, by definition cannot provide feedback to the ambient flow conditions. For example, vertical motions resulting from a plume rise do not affect the distribution of horizontal wind components in the background flow. Of course, this is inconsistent with mass continuity.

## CONCLUSIONS

- It is feasible to operate the three-dimensional atmospheric models HOTMAC and RAPTAD to forecast the transport and dispersion of airborne materials at VAFB.
- HOTMAC and RAPTAD predictions were at least as good as those obtained by diagnostic models and the MI model where wind data were available.
- HOTMAC and RAPTAD predictions were far better than those obtained by diagnostic models and they were the best practical solution where wind data were not available.
- It is feasible to operate HOTMAC and RAPTAD on a desktop computer. HOTMAC took 4 hours 11 minutes and 22 hours 10 minutes CPU time, respectively, on a Sun 4/110 workstation, and a MicroVax 2000 computer for a 28 hours forecast with 21 x 25 x 16 grid points. RAPTAD took 26 minutes and 3 hours 45 minutes CPU time, respectively, on a Sun 4/110 workstation, and a MicroVax 2000 computer for a 20 hour simulation.
- The affordability and portability of the desktop computer has opened the door to upgrading toxic-hazard modeling capabilities for emergency response management at VAFB.

- The HOTMAC and RAPTAD modeling system would be a useful addition to enhance current VAFB emergency response management capabilities.
- It is feasible to incorporate the positive and negative source buoyancy effects in HOTMAC and RAPTAD. Our approach can minimize the ambiguities and inconsistencies introduced in a simple plume rise model.

## RECOMMENDATIONS

- Become familiar with background theories and operating procedures of HOTMAC and RAPTAD. Install the models on a mainframe computer and repeat the simulations discussed in this report.
- Consider upgrading computer capabilities for emergency response applications at VAFB. MicroVax computers may not be fast enough to operate HOTMAC and RAPTAD.
- Modify HOTMAC to run all the time and store wind and turbulence data for the next 24 hours. When an emergency occurs, RAPTAD can be used immediately with the wind data stored on a disk. The RAPTAD computation is much faster than that of HOTMAC. Thus, this approach meets better the time constraint imposed under emergency situations.
- Develop a method to integrate tower data into HOTMAC. The wind data can be used to initialize and correct the wind distribution in HOTMAC. These may be accomplished by a dynamical initialization technique and a four-dimensional data assimilation method.
- Develop a method to predict concentration variances which can be used to estimate uncertainties associated with predictions. A short time averaging value is required for predicting concentration of toxic materials. Such a value normally exhibits great variations in time and space.
- Add model physics necessary to simulate the evolution of fog formation and dissipation processes. Fog is frequently observed at VAFB and it affects the heat energy balance at the ground.
- Continue to investigate the feasibility of incorporating positive and negative source buoyancy effects in HOTMAC and RAPTAD and test the scheme with observations.

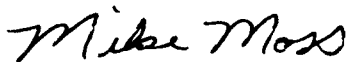
## PREFACE

This report was prepared by the Los Alamos National Laboratory, P. O. Box 1630, Los Alamos, NM 87545, under the DOE/USAF Funding Document, MIPR Number N88-26, for the Air Force Engineering and Services Center (AFESC), Engineering and Services Laboratory, Tyndall Air Force Base, Florida 32403.

This report summarizes work done between May 1, 1988 and April 30, 1991. Captains Michael Moss and Lawrence Key were the AFESC/RDVS Project Officers.

This report has been reviewed by the Public Affairs Office and is releasable to the National Technical Information Service (NTIS). At NTIS, it will be available to the general public, including foreign nationals.

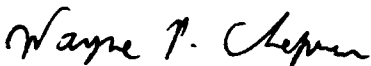
This technical report has been reviewed and is approved for publication.



MICHAEL T. MOSS, Capt, USAF  
Senior Research Meteorologist



NEIL J. LAMB, Col, USAF, BSC  
Chief, Environics Division



WAYNE P. CHEPREN, Capt, USAF  
Chief, Environmental Compliance R&D



FRANK P. GALLAGHER III, Col, USAF  
Director, Engineering and Services  
Laboratory

## TABLE OF CONTENTS

Section	Title	Page
I	INTRODUCTION . . . . .	1
	A. Objective . . . . .	2
	B. Background . . . . .	2
	C. Scope . . . . .	3
II	TASKS . . . . .	4
	A. PHASE I . . . . .	4
	1. VAFB Terrain Data . . . . .	4
	2. Model Runs . . . . .	4
	3. Model Comparisons . . . . .	4
	B. PHASE II . . . . .	4
	1. HOTMAC/RAPTAD on MicroVax Computer . . . . .	4
	C. PHASE III . . . . .	5
III.	MODEL DESCRIPTION . . . . .	6
IV.	MOUNTAIN IRON DIFFUSION DATA SIMULATIONS . . . . .	8
	A. MOUNTAIN IRON DIFFUSION EXPERIMENTS . . . . .	8
	B. SIMULATIONS AND DISCUSSIONS . . . . .	12
	1. MI87 Simulation . . . . .	14
	2. MI90 Simulation . . . . .	26
	3. MI91 Simulation . . . . .	28
V.	MODEL COMPARISONS . . . . .	51
	A. WIND MODEL . . . . .	51
	B. DIFFUSION MODEL . . . . .	58
VI.	APPLICATIONS ON DESKTOP COMPUTERS . . . . .	63
	A. SUN 4/110 WORKSTATION . . . . .	63
	B. MICROVAX 2000 . . . . .	74

# TABLE OF CONTENTS (Continued)

Section	Title	Page
VII.	BUOYANT PLUMES . . . . .	85
	A. POSITIVE BUOYANT SOURCE . . . . .	88
	B. NEGATIVE BUOYANT SOURCE . . . . .	96
VIII.	CONCLUSIONS AND RECOMMENDATIONS . . . . .	108
	A. CONCLUSIONS . . . . .	108
	B. RECOMMENDATIONS . . . . .	109
APPENDIX		
A.	DESCRIPTION OF MODELS AND NUMERICAL PROCEDURES . . . . .	111

## LIST OF FIGURES

Figure	Title	Page
1	The Study Area, South Vandenberg, is Located Approximately 160 km West-northeast of Los Angeles . . . . .	9
2	Terrain Feature in South Vandenberg . . . . .	10
3	Sites for Meteorological Masts and Upper Air Soundings . . . . .	11
4	Sites for Air Samplers of Fluorescent Particles and the Primary Source VIP1 . . . . .	13
5	Modeled Horizontal Wind Vectors for the MI87 Cast at 10 meters above the Ground at 1300 lst, June 13, 1966. Wind vectors at every other grid points are plotted . . . . .	16
6	Same as in Fig. 5 except Observed Wind Vectors in the Surface Layer are Shown . . . . .	17
7	Vertical Profiles of the Modeled Wind Speed, Direction, and Potential Temperature for the MI87 Case at 1300 lst, June 13, 1966 . . . . .	18
8	Modeled Ground Level Exposure Values of Fluorescent Particles for the MI87 Case . . . . .	24
9	Same as in Figure 8 except the Observed Values are Contoured . . . . .	25
10	Same as in Figure 5 except in the Larger Computational Domain . . . . .	27
11	Modeled Horizontal Wind Vectors for the MI90 Case at 10 meters above the ground at 2300 lst, June 21, 1966 . . . . .	29
12	Same as in Figure 11 except Observed Wind Vectors in the Surface Layer are Shown . . . . .	30
13	Vertical Profiles of the Modeled Wind Speed, Direction, and Potential Temperature for the MI90 Case at 2300 lst, June 21, 1966 . . . . .	31
14	Modeled Ground Level Exposures of Fluorescent Particles for the MI90 Case . . . . .	36

# LIST OF FIGURES (Continued)

Figure	Title	Page
15	Same as in Figure 14 except the Observed Values are Contoured . . .	37
16	Modeled Horizontal Wind Vectors for the MI91 Case at 10 meters above the Ground at 0200 1st, June 22, 1966 . . . . .	39
17	Vertical Profiles of the Modeled Standard Deviation of Vertical Wind Component, Turbulence Kinetic Energy, and Standard Deviation of Potential Temperature at VIP1 at 0200 1st, June 22, 1966 . . . . .	40
18	Same as in Figure 16 except Observed Wind Vectors in the Surface Layer are Shown . . . . .	41
19	Vertical Profiles of the Modeled Wind Speed, Direction, and Potential Temperatue for the MI91 Case at 0200 1st, June 17, 1966 . . . . .	43
20	Modeled Ground Level Exposures of Fluorescent Particles for the MI91 Case . . . . .	48
21	Same as in Figure 20 except the Observed Values are Contoured . . .	49
22	Modeled Horizontal Wind Vectors for the MI87 Case at 4 meters above Ground Level by Using WOCSS Diagnostic Wind Model . . . . .	53
23	Modeled Horizontal Wind Vectors for the MI87 Case at 10 meters above Ground Level by Using LINCOM Diagnostic Wind Model . . . . .	54
24	Same as in Figure 22 except for the MI90 Case . . . . .	56
25	Same as in Figure 23 except for the MI90 Case . . . . .	57
26	Exposure Distribution of Fluorescent Particles at Ground Level Modeled by RIMPUFF for the MI87 Case . . . . .	59
27	Same as in Figure 26 except for the MI90 Case . . . . .	60
28	Scatter Diagram of the Predicted and Observed Fluorescent Particle Concentration (nondimesional) at Ground Level . . . . .	62

# LIST OF FIGURES (Continued)

Figure	Title	Page
29	Modeled Horizontal Wind Vectors at 14 meters above the Ground .	65
30	Modeled Trajories of Puff Centers Projected on the Surface . . .	69
31	Concentration Distribution (in arbitrary units) of Fluorescent Particles at Ground Level . . . . .	75
32	Modeled Trajectories of Puff-Centers Projected on the Surface at 1100 1st, June 13, 1966. Puffs were released continuously for 20 hours starting at 0600 1st, June 13, 1966. The results were obtained by a MicroVax 2000 . . . . .	81
33	Concentration Distribution (in arbitrary units) of Fluorescent Particles at Ground Level at 1100 1st, June 13, 1966. The results were obtained by a MicroVax 2000 . . . . .	82
34	Same as in Figure 30, but the Results were Obtained by a Sun 4/110 Workstation . . . . .	83
35	Same as in Figure 31, but the Results were Obtained by a Sun 4/110 Workstation . . . . .	84
36	Horizontal Wind Vector Distribution at 30 meters above the Ground. The heated area is indicated by a rectangle . . . . .	89
37	Wind Vectors in East-West Vertical Cross Sections along (a) the Southern Boundary and (b) the Central Axis of the Fire . . . . .	91
38	Wind Vectors in North-South Vertical Cross Sections along (a) $x = 14.5$ km (b) $x = 16$ km, and (c) $x = 17$ km . . . . .	93
39	Vertical Profiles of Standard Deviation of Vertical Velocity, $\sigma_w$ ; Twice Turbulence Kinetic Energy, $q^2$ ; and Standard Deviation of Potential Temperature, $\sigma_t$ . . . . .	97



# LIST OF FIGURES (Continued)

Figure	Title	Page
40	Three-Dimensional Projections of Puff Centroids . . . . .	98
41	Horizontal Wind Vectors at 10 meters above the Ground at 0400 1st. The cold area is indicated by a rectangle . . . . .	102
42	Projections of Puff Centroids on the Ground . . . . .	103
43	Suface Concentration Contours (in arbitrary units) . . . . .	106
A-1	Relative Locations of Mean and Turbulence Variables in the Computational Grid. . . . .	133

## LIST OF TABLES

Table	Title	Page
1	COMPARISON BETWEEN THE MODELED AND OBSERVED EXPOSURES FOR MI87 CASE . . . . .	23
2	COMPARISON BETWEEN THE MODELED AND OBSERVED EXPOSURES FOR MI91 CASE . . . . .	42
3	CPU COMPARISON BETWEEN SUN 4/110 AND MICROVAX 2000 . . . . .	80
A-1	COEFFICIENTS $K_1, K_2, K_3, A$ , AND $F$ IN EQ. (A-58) . . . .	129
A-2	COEFFICIENTS $A_t, B_t, C_t$ and $D_t$ FOR EQ. (A-69) . . . . .	131

(The reverse of this page is blank)

## SECTION I

### INTRODUCTION

Air Force (AF) models designed to calculate the atmospheric transport and dispersion of pollutants at Vandenberg Air Force Base (VAFB) include the Rocket Exhaust Effluent Dispersion Model (REEDM) system (Reference 1; Reference 2) and the Ocean Breeze/Dry Gulch (OB/DG) equation (Reference 3), Mountain Iron (MI) equation (Reference 4; Reference 5), and Sudden Ranch (SR) equation (Reference 6). REEDM was designed to model the transport and dispersion of buoyant plumes of rocket exhaust during normal launch and fireball rise and subsequent dispersion in the event of an explosive accident. OB/DG, MI, and SR are empirical equations designed to calculate toxic hazard corridors resulting from accidental spills of toxic chemicals. These models assume that the wind field over the geographical area of interest can be adequately represented by the wind speed and direction measured at a single point (or, in the case of REEDM, a vertical profile of wind speed and direction over a single point). These models also assume that the toxic plume or puff released to the atmosphere is uniformly distributed around a centerline determined from the wind direction measured at the single observation site.

While the model and equations listed above have been acceptable in the past, the complex terrain and meteorology at VAFB, increased amounts of toxic chemicals stored there, increases in the surrounding civilian population, higher anticipated launch rates, and the reduction in personal exposure limits for the AF chemicals of interest (nitrogen tetroxide and Aerozine-50) require more accurate methods. Current efforts to improve VAFB's modeling capability include development of the Air Force Toxic (AFTOX) Chemical Dispersion model (Reference 7) by the Air Force Geophysics Laboratory (AFGL). AFTOX, in its current form, however, also assumes the three-dimensional wind field can be represented by a single wind value. Efforts have been

made to couple AFTOX with a surface layer wind flow model; however, the complexity of the terrain and meteorology at VAFB require a model that takes into account the three-dimensional wind field over the entire VAFB region.

Previous AF efforts to improve toxic hazard models have been limited by available computer power. Recent developments in computer hardware technology, however, have the potential to allow much more sophisticated models to be operated in much less time than previously considered possible.

#### A. OBJECTIVE

The purpose of this study is to demonstrate the feasibility of using a small computer to operate three-dimensional hydrodynamic and diffusion models to describe the transport and dispersion of atmospheric pollutants at VAFB. This effort will use the Los Alamos National Laboratory (LANL) HOTMAC (Higher Order Turbulence Model for Atmospheric Circulations) and RAPTAD (Random Puff Transport and Diffusion) models (Reference 8) on a desktop computer to accomplish the objective.

#### B. BACKGROUND

HOTMAC and RAPTAD are significantly different from any AF models mentioned above. HOTMAC is referred to as a prognostic model and solves a set of time-dependent physical equations such as conservation equations of momentum, internal energy, mixing ratio of water vapor, and turbulence variables. HOTMAC forecasts three-dimensional distributions of wind speed, wind direction, temperature, and moisture. The current AF models use a single wind value or a vertical profile of wind speed and direction at a single location. Clearly, a single value or a single profile of wind cannot provide realistic wind distributions for diffusion computations because the terrain and meteorology in the VAFB area are highly heterogeneous.

HOTMAC provides to RAPTAD both mean and turbulence variables to simulate transport and diffusion processes of airborne materials. Only a few mesoscale atmospheric models can forecast three-dimensional variations of atmospheric turbulence. Other mesoscale models are being modified to incorporate second-moment turbulence closure equations similar to those first implemented in HOTMAC. HOTMAC and RAPTAD predictions have been tested extensively with observations and they have been running successfully on a desktop computer. Therefore, HOTMAC and RAPTAD offer a highly advanced forecasting capability, compared with simple emergency response management models.

An operational, three-dimensional, predictive modeling system that meets all the requirements for the emergency response management at VAFB is a challenge. We believe that the recent advancements in scientific workstations will result in a practical operational modeling system much earlier than we expected.

### C. SCOPE

Section II discusses the tasks required to accomplish the project goals, and Section III reviews the model equations, boundary conditions, and numerical schemes used in HOTMAC and RAPTAD. In Section IV we review the MI diffusion experiment and present modeling results for MI87, MI90, and MI91 cases. In Section V, we compare our model results with those obtained from current AF models and RIMPUFF/LINCOM (Reference 9) models developed at RISO National Laboratory, Roskilde, Denmark.

Our experience with running HOTMAC/RAPTAD on a Sun workstation is discussed in Section VI. We studied the feasibility of incorporating positive and negative buoyancy effects in HOTMAC and RAPTAD, and the results are presented in Section VII. Finally, conclusions and recommendations for future work are given in Section VIII.

## SECTION II

### TASKS

#### A. PHASE I

##### 1. VAFB Terrain Data

The contractor will enter digitized terrain data/surface condition information for VAFB into the HOTMAC/RAPTAD model. The AF project officer will ensure that the contractor receives the needed VAFB data.

##### 2. Model Runs

The contractor will operate HOTMAC/RAPTAD with VAFB terrain data for two cases representing seasonal average meteorology at VAFB, simulating ground-level releases of a neutrally buoyant gas. The AF project officer will designate the cases to be run.

##### 3. Model Comparisons

The contractor will compare output from HOTMAC/RAPTAD for each of the simulated ground-level releases with that of AFTOX and either OB/DG, MI, or SR. The AF project officer will designate which of these models will be used.

#### B. PHASE II

##### 1. HOTMAC/RAPTAD on MicroVax Computer

Upon approval by the AF project officer, the contractor will operate the HOTMAC/RAPTAD model on a MicroVax computer resident at LANL. The contractor will perform the model runs as listed in paragraphs in II.A.2 and II.A.3.

### C. PHASE III

The contractor will investigate incorporating positive and negative source buoyancy effects in RAPTAD and determining the feasibility of incorporating these effects.

Upon approval of the AF project officer, these effects will be incorporated into the version of HOTMAC/RAPTAD resident at LANL. Upon incorporation of these changes, the contractor will operate HOTMAC/RAPTAD using a test case to determine the performance of the model.

## SECTION III

### MODEL DESCRIPTION

Significant advances in engineering workstation technologies have had a phenomenal impact on computational fluid dynamics. We have been using a Sun 4 Workstation to successfully run state-of-the-art, three-dimensional, atmospheric transport and diffusion models which were originally developed on a supercomputer.

Our modeling system is composed of two numerical codes, HOTMAC and RAPTAD (Reference 8). Only brief reviews of HOTMAC and RAPTAD are given here. A detailed description of the model equations, boundary conditions, and numerical scheme is given in Appendix A.

HOTMAC is a mesoscale atmospheric model that can forecast three-dimensional distributions of wind speed, wind direction, turbulence, temperature, and water vapor. The basic equations for HOTMAC are the conservation equations for mass, momentum, internal energy, mixing ratio of water vapor, and turbulence kinetic energy (Reference 8).

Surface boundary conditions are constructed from the empirical formulas by Dyer and Hicks (Reference 10) for nondimensional wind and temperature profiles. The temperatures in the soil layer are obtained by solution of the heat conduction equation. Appropriate boundary conditions are the heat energy balance at the soil surface and specification of the soil temperature at a certain depth. The lateral boundary values are obtained by integration of the corresponding governing equations except that variations in the horizontal directions are all neglected.

An initial wind profile at a reference site in the computational domain is first constructed with the assumption of a logarithmic variation from the ground up to the level where the wind speed reaches an ambient value. Initial wind profiles at other grid locations are obtained from



the winds determined above and the conditions  $\partial U/\partial x = 0$  and  $\partial V/\partial y = 0$ .

The governing equations are integrated by use of the Alternating Direction Implicit method (Reference 11). A time increment is chosen to be 90 percent of the minimum value of  $\Delta x_i/U_i$ , where  $\Delta x_i$  is a grid spacing and  $U_i$  is the velocity in the  $i$ th direction (Courant-Freidrich-Lewy criteria). To increase the accuracy of finite-difference approximations, mean and turbulence variables are defined at grids staggered in both the horizontal and vertical directions. Mean winds, temperature, and water vapor vary most with height near the surface. Nonuniform grid spacings are used in the vertical direction to resolve these variations without introducing an excessive computational burden.

RAPTAD is a Lagrangian puff code based on the Monte Carlo statistical diffusion process. The center location and standard deviation of concentration distribution for each puff are computed by use of wind and turbulence modeled by HOTMAC. Then, concentration at any location is computed by summation of concentrations contributed by all the puffs. RAPTAD can be used under extreme conditions with highly heterogeneous wind and turbulence distributions where a conventional Gaussian plume model may fail.

## SECTION IV

### MOUNTAIN IRON DIFFUSION DATA SIMULATIONS

#### A. MOUNTAIN IRON DIFFUSION EXPERIMENTS

To test the feasibility of operating HOTMAC/RAPTAD with the VAFB terrain (Tasks II.A.1 and II.A.2), we selected data from the Mountain Iron diffusion experiments (Reference 4), which were conducted at VAFB during 1965 and 1966. The objective of the MI program was to establish quantitative diffusion predictions for use as range safety tools in the "South Vandenberg" (SV) ballistic and space vehicle operations area (Reference 4). South Vandenberg is located along the California coast approximately 160 km west-northwest of Los Angeles (Figure 1). The coastline is oriented in approximately a north-south direction along the western side of SV (Figure 1), but changes abruptly at Point Arguello to an east-west direction. The coastline gradually changes to north-south toward Point Conception and then changes again to an east-west direction. The Santa Ynez Mountains form an east-west barrier along the coastline far south of SV.

Another prominent terrain feature in the experimental area (Figure 2) is Honda Canyon (HC), walled by Target Ridge on the north and Honda Ridge on the south. The distance between the two ridges is generally less than 2.5 km. The elevation difference between the bottom of the canyon (less than 120 meters above mean sea level, msl) and the average height of the ridges is approximately 200 meters.

Meteorological masts 10, 50, 100, and 300 feet high were deployed (Figure 3) to measure wind speeds and wind directions. Temperature differences between 6 and 54 feet above ground level and standard deviations of horizontal wind directions were also measured at the tracer release points. The wind data are used to examine the performance of HOTMAC in Section IV.B.

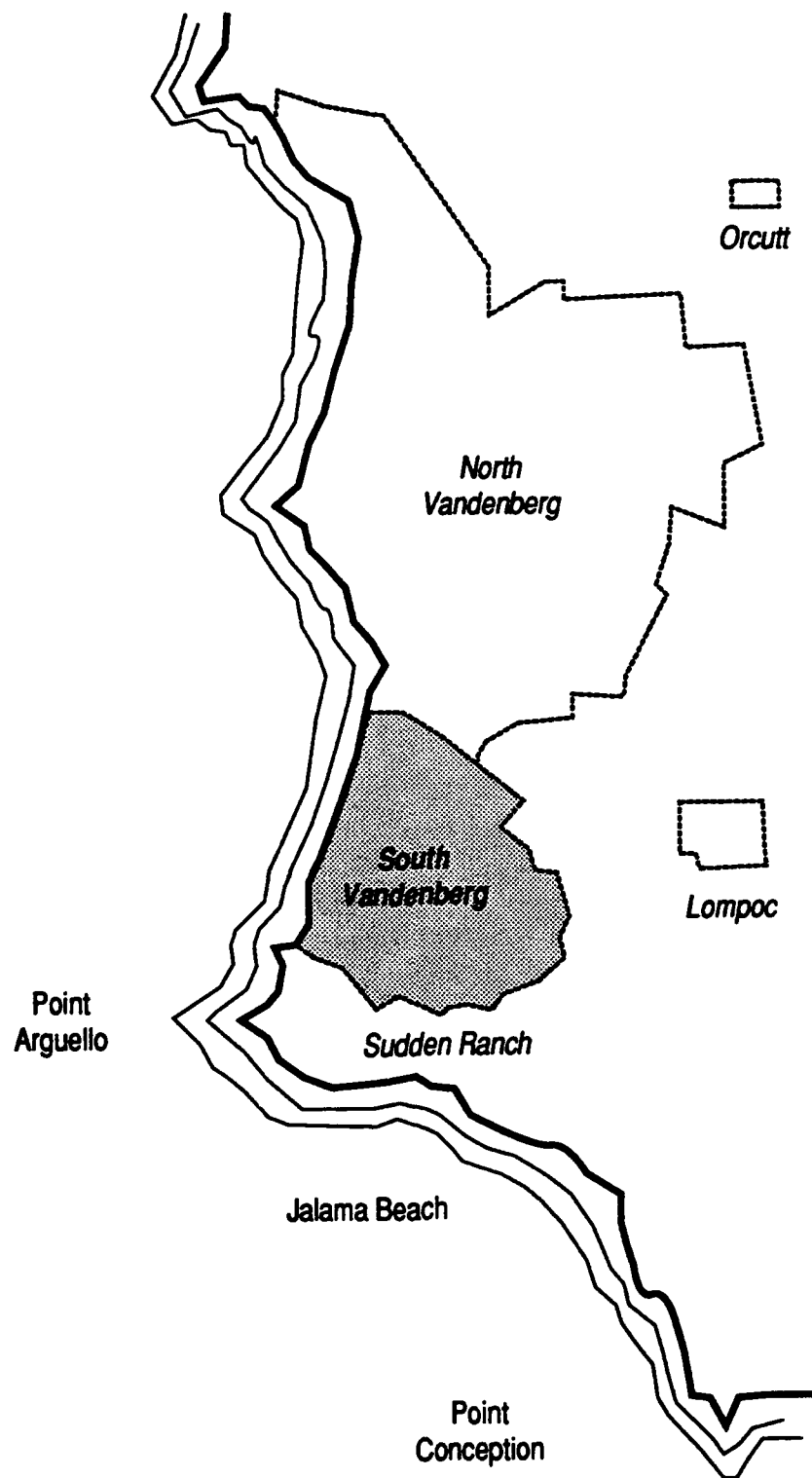


Figure 1 The Study Area, South Vandenberg, is Located Approximately 160 km West-Northwest of Los Angeles.

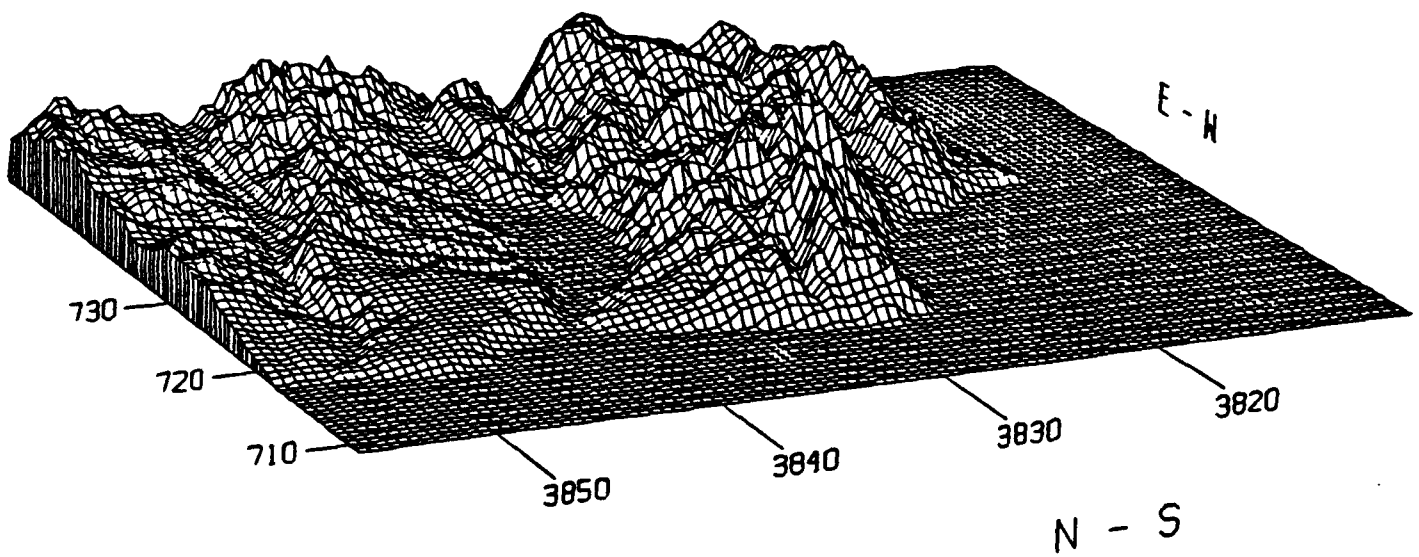


Figure 2. Terrain Features on South Vandenberg.

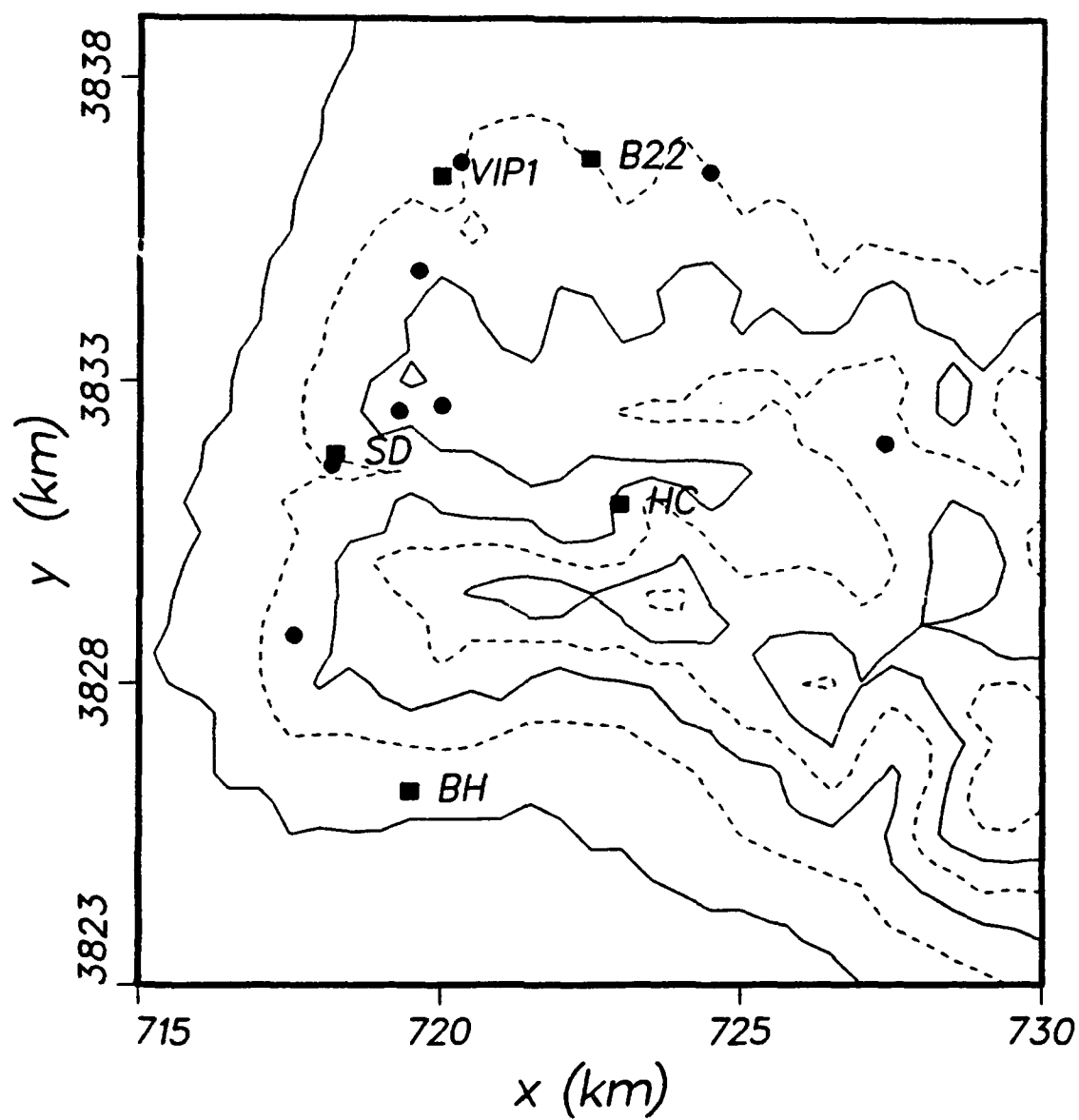


Figure 3. Sites for Meteorological Masts (•) and Upper Air Soundings (■).

Vertical profiles of wind speed, wind direction, and wet and dry temperature up to 2000 meters above the ground were measured by rawinsondes at four sites, and wind profiles were taken by a wiresonde at the tracer release site. The soundings were taken hourly for 3 to 4 hours starting at 1 hour before the tracer release. The vertical profiles of winds and temperatures are used to initialize the model variables and test the model predictions.

Fluorescent pigment zinc sulfide particles with a geometric mean of  $2.5 \mu\text{m}$  were released to aid the understanding of transport and diffusion processes and the derivation of an empirical formula for the pollutant concentration distribution in the SV area. The effective release height was 2 to 6 meters above the ground. The primary sampler used was a membrane filter inserted in a disposable polyethylene holder. The bulk samples from the field were assayed by use of the Rankin counter, which uses an alpha emitter to activate the fluorescent pigment deposited on the membrane filter (Reference 5).

Accessibility in the rugged terrain dictated the design of the sampling grid: existing roads and Jeep trails provided a suitable and convenient network of sampling routes. The roads, in general, follow creek banks and ridge tops. The chosen sampler sites are shown in Figure 4. The sampling distances from the primary source point (VIP1) with northwest and north-northwest prevailing winds were 1.5, 2.5, 4, 6, and 7 km. The samplers along the routes were spaced 1/10 mile (160 meters) apart near the source, 2/10 mile (320 meters) apart midway, and 4/10 mile (640 meters) apart along the coastline far south of SV (Figure 4).

## B. SIMULATIONS AND DISCUSSIONS

A total of 113 tracer releases were made from which 8 cases were selected (Reference 12) for detailed studies based on the flow-field categorization in the Plume Dispersion Handbook.

The wind data from these eight cases were used to evaluate the performance of the diagnostic wind model WOCSS, Winds on Critical Streamline Surfaces (Reference 12). More

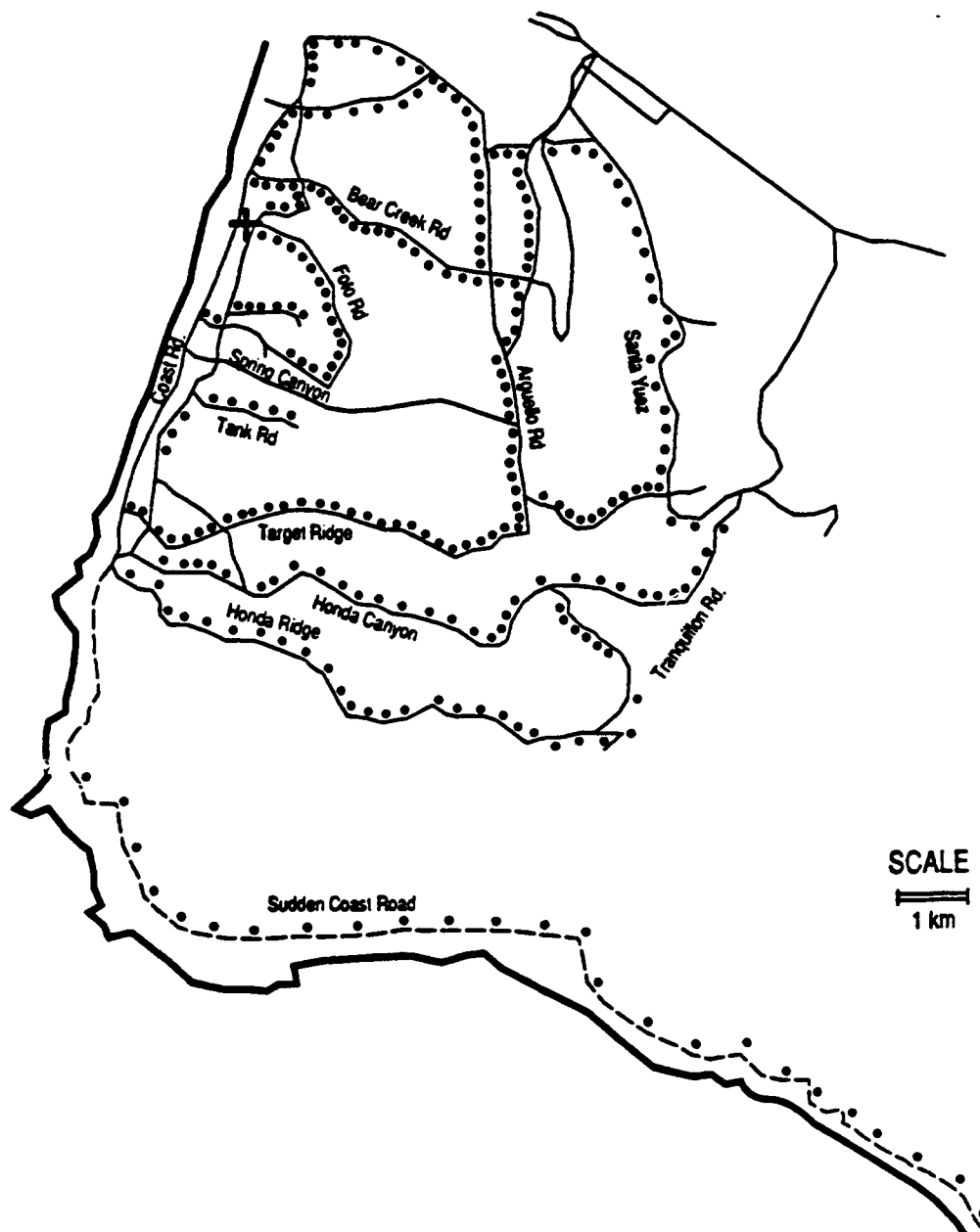


Figure 4. Sites for Air Samplers for Fluorescent Particles (●) and the Primary Source, VIP (+).

recently, Riso National Laboratory wind and diffusion models LINCOM and RIMPUFF were evaluated by use of the MI87 and MI90 data sets (Reference 13).

Based on these previous studies, we selected the MI87, MI90, and MI91 cases to evaluate the performance of HOTMAC and RAPTAD. The following sections describe in detail each simulation result for the MI87, MI90, and MI91 cases.

## 1. MI87 Simulation

The meteorological condition for the MI87 case was characterized (Reference 12) as "weak ambient and sea-breeze flow, with little distinction between wind vectors, but sharp cooling with fog rolling in." Fog was observed all morning at the Boat House (BH) site, but none at HC until after 1500 local standard time (lst). Fog progressed into the release site (VIP1), probably an hour before the 1310 lst release time (Reference 12).

The initial potential temperature profile was determined by averaging the four upper air soundings at 1300 lst at BH, Scout D (SD), HC, and Building 22 (B22) (Figure 3). The potential temperature lapse rate was approximately  $0.044^{\circ}\text{C/m}$  from the sea surface to 460 meters above msl,  $0.0142^{\circ}\text{C/m}$  between 460 and 960 meters above msl, and  $0.0045^{\circ}\text{C/m}$  above 960 meters above msl. Wind speed and direction were determined by examining five upper air soundings (four locations mentioned above plus VIP1) at 1300 lst. Initial upper air wind speed and wind direction above the boundary layer were estimated to be 2 m/s and 225 degrees, respectively.

The computational domain is  $40 \times 48 \text{ km}^2$  with a horizontal grid spacing of 1 km. To resolve the details of topography in the vicinity of the release site, we decided to nest a fine-resolution grid  $15 \times 16 \text{ km}^2$  with a horizontal grid spacing of 0.5 km.

Integration started at 0500 lst, June 13, 1966, and continued for over 12 hours. The plume was released at 1310 lst for 30 minutes as was done in the experiment. The plume



was followed for 4 hours in the model computation. By that time, the plume had moved far from the sampling areas.

Figure 5 shows the modeled horizontal wind vectors in the inner computational grid at 10 meters above the ground at 1300 lst, June 13 (Julian date 164). Although the upper air wind direction is 225 degrees (southwest), upslope flows develop in the surface layer as a result of heating at the sloped surfaces.

The modeled wind distribution (Figure 5) agrees with the observation (Figure 6). The observed winds show much more variation in space than the modeled winds. Observations near each other show considerable variation in direction and magnitude. On the other hand, the modeled wind field varies more slowly in space than the observed wind field since the model neglects subgrid-scale variations of the surface (the grid resolution is 500 meters). Nevertheless, the simulations successfully reproduced many observed features.

Less satisfactory results are obtained in comparison of the vertical profiles of the modeled wind speed and wind direction with observations (Figure 7). Wind speed and wind direction vary greatly in space and time when the wind speed is small. The observations are instantaneous values whereas the modeled results are ensemble averages. On the other hand, potential temperature profiles are relatively stationary unless synoptic-scale disturbances such as fronts pass through the measurement area.

Significant changes in the modeled wind direction occurred at around 600 meters above the ground. These changes are caused by the mass conservation constraint to compensate for the divergence and convergence of the wind distributions in the boundary layer (Figure 5). Observed wind direction profiles appear to support such variations, but the changes appear to occur at heights much closer to the ground than those modeled.

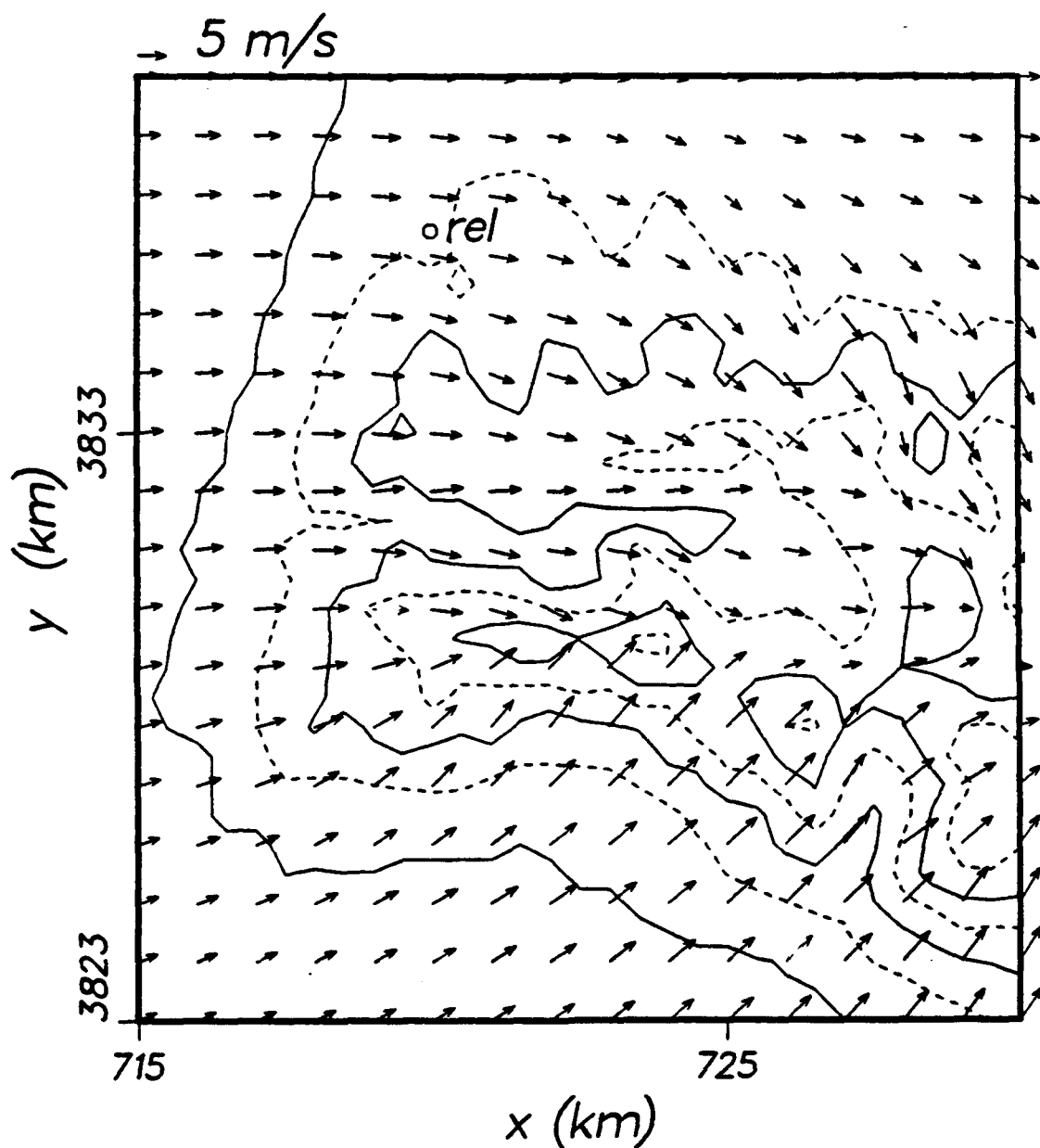


Figure 5. Modeled Horizontal Wind Vectors for the MI87 Case at 10 meters above the Ground at 1300 lst, June 13, 1966. Wind vectors at every other grid point are plotted. Terrain is contoured by solid lines with an increment of 200 meters. Dashed lines indicate contours halfway between the solid contours.

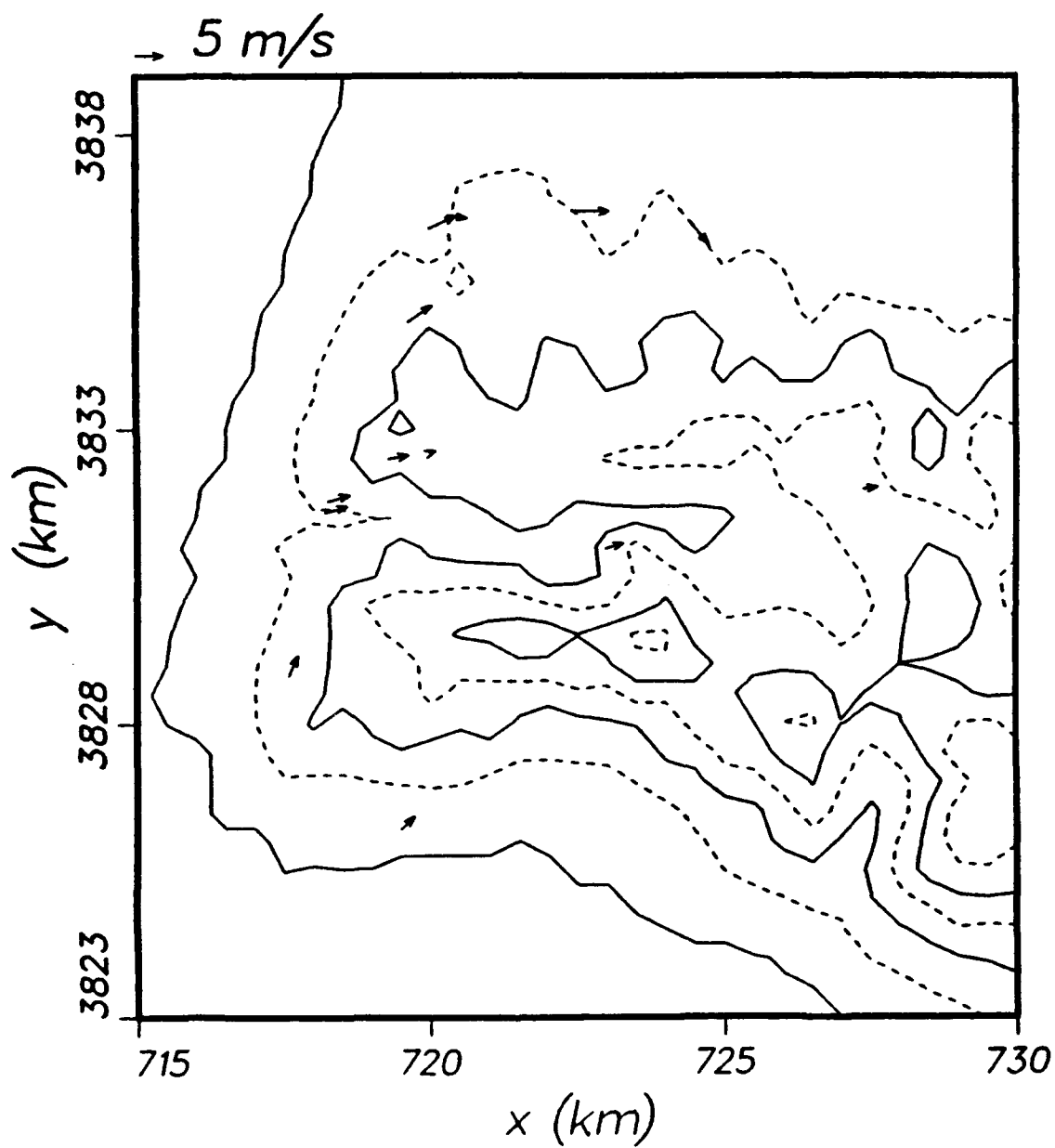


Figure 6. Same as in Figure 5 except Observed Wind Vectors in the Surface Layer are Shown.

MI87 BH 1300

(a)

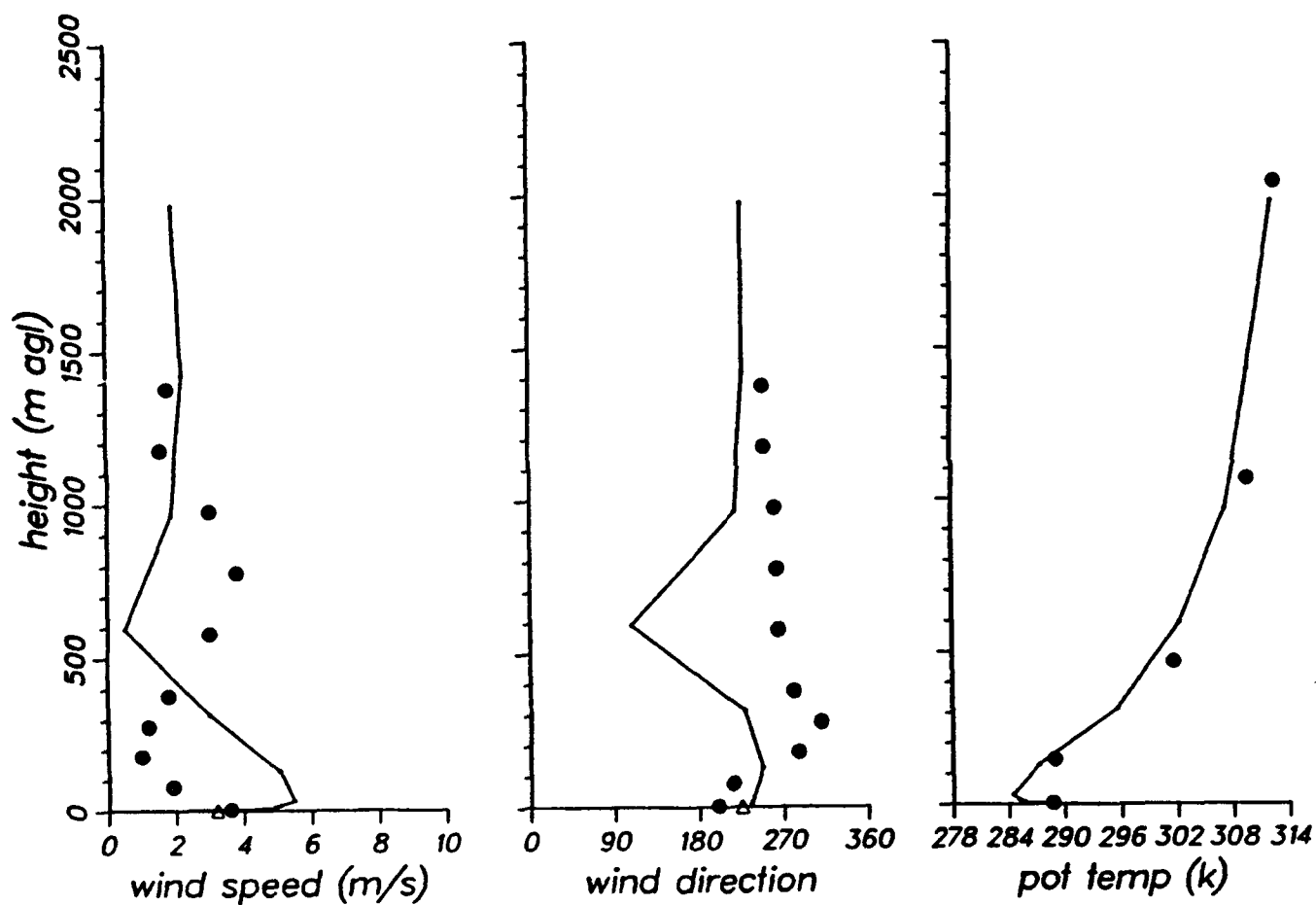


Figure 7. Vertical Profiles of the Modeled Wind Speed, Direction, and Potential Temperature for the MI87 Case at 1300 lst, June 13, 1966 at (a) BH, (b) HC, (c) SD, (d) VIP1, and (e) B22. Solid circles indicate observations.

MI87 HC 1300

(b)

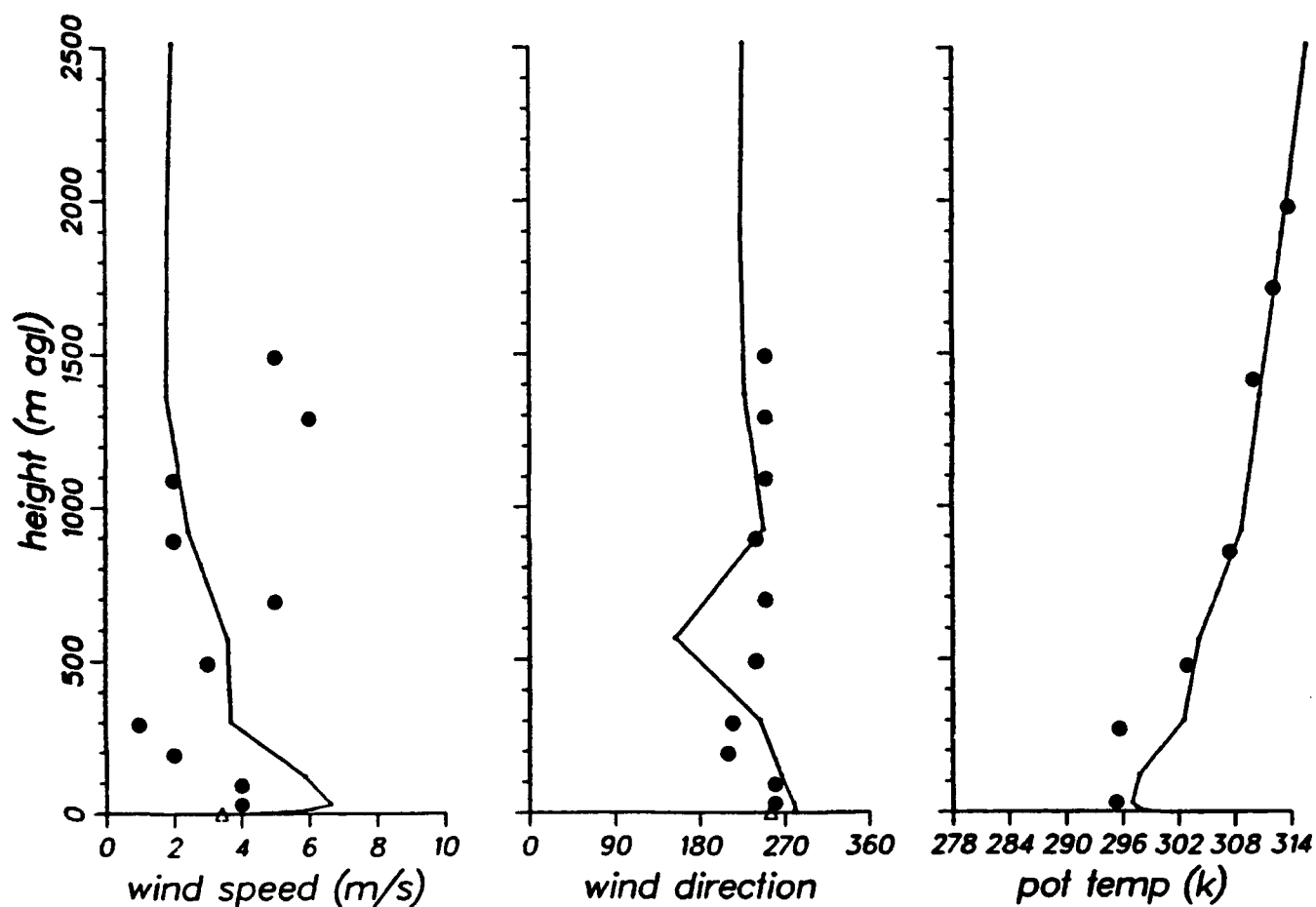


Figure 7. Vertical Profiles of the Modeled Wind Speed, Direction, and Potential Temperature for the MI87 Case at 1300 lst, June 13, 1966 at (a) BH, (b) HC, (c) SD, (d) VIP1, and (e) B22. Solid circles indicate observations.

MI87 SD 1300

(c)

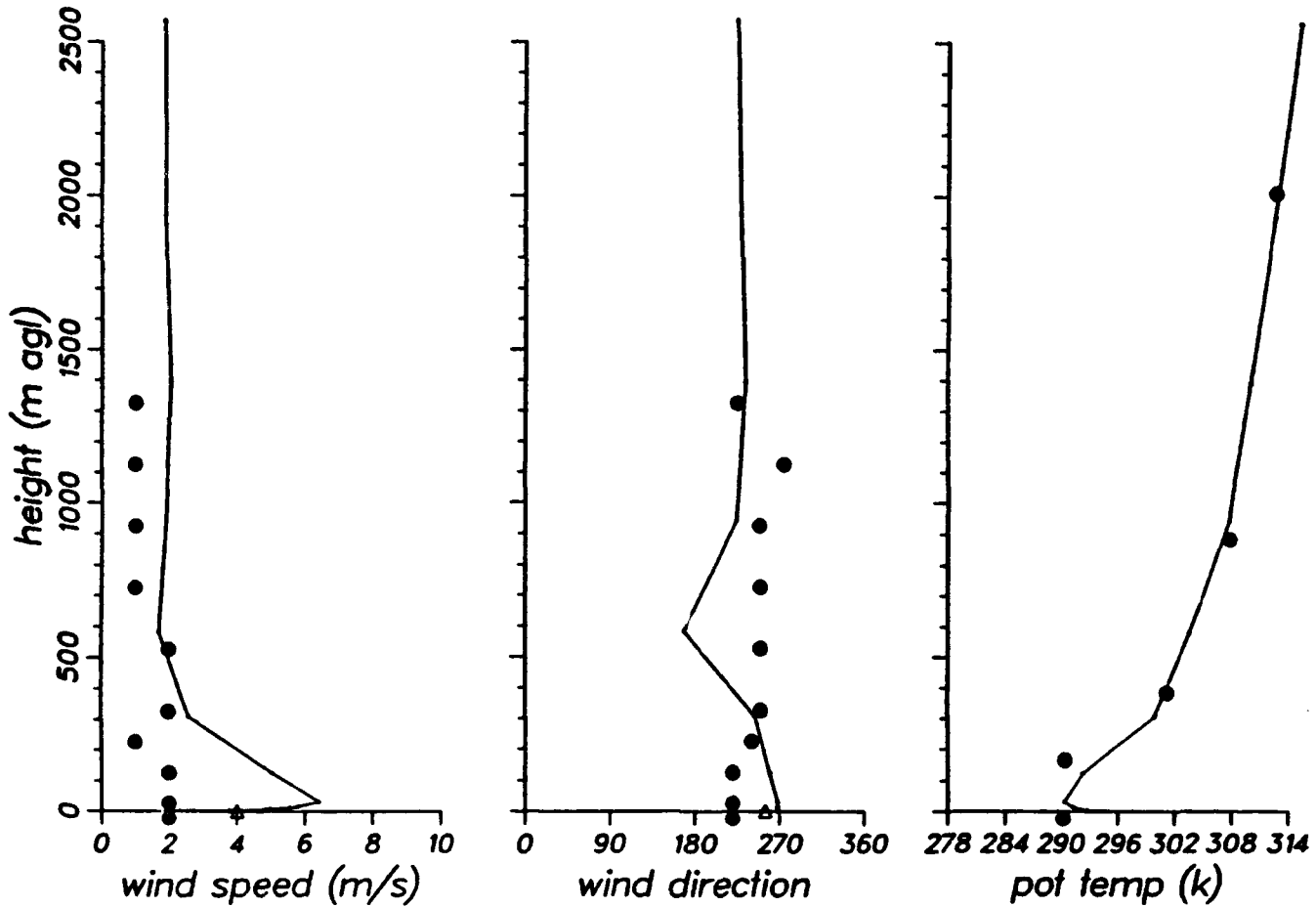


Figure 7. Vertical Profiles of the Modeled Wind Speed, Direction, and Potential Temperature for the MI87 Case at 1300 lst, June 13, 1966 at (a) BH, (b) HC, (c) SD, (d) VIP1, and (e) B22. Solid circles indicate observations.

MI87 VIP1 1300

(d)

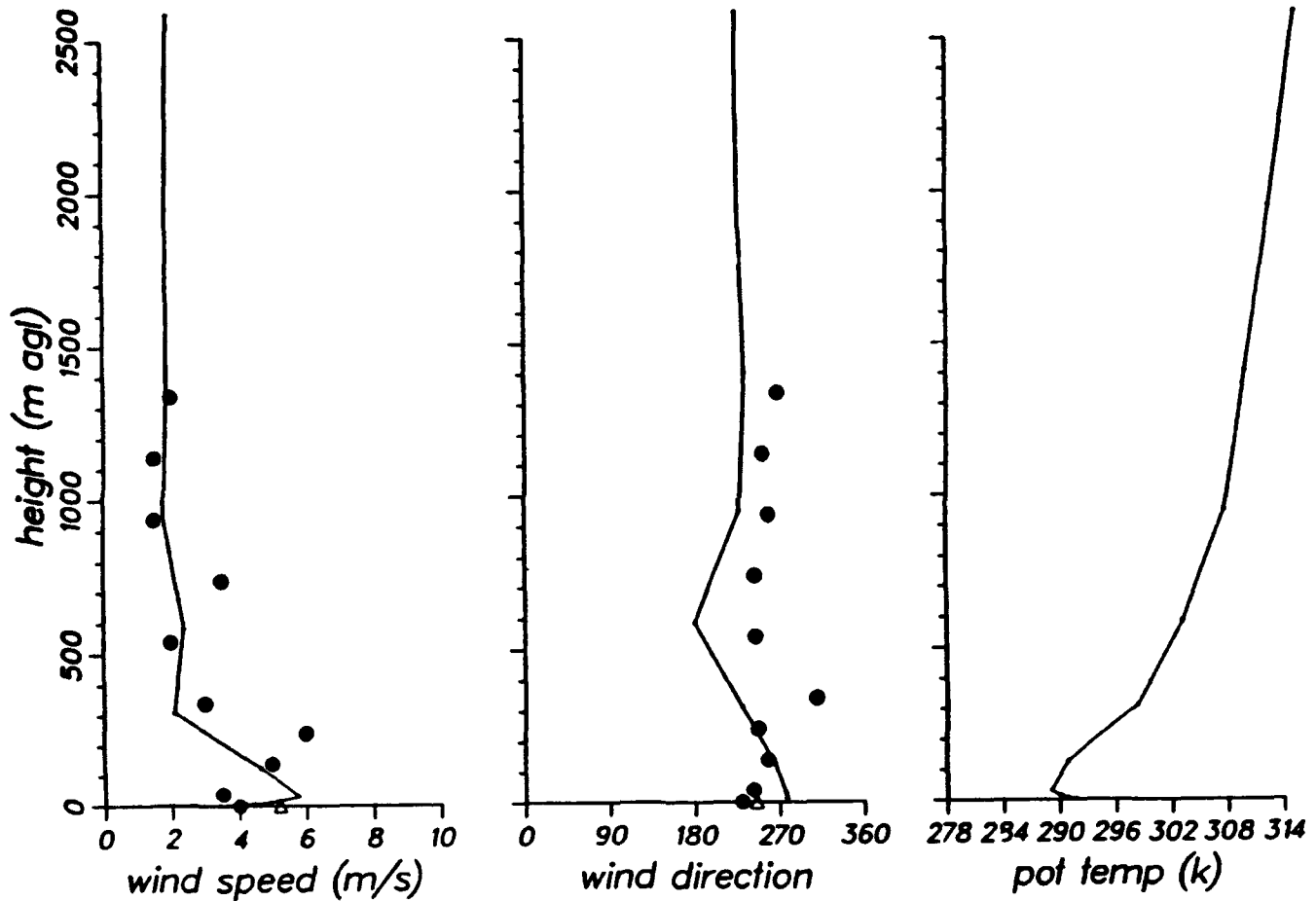


Figure 7. Vertical Profiles of the Modeled Wind Speed, Direction, and Potential Temperature for the MI87 Case at 1300 lst, June 13, 1966 at (a) BH, (b) HC, (c) SD, (d) VIP1, and (e) B22. Solid circles indicate observations.

MI87 B22 1300

(e)

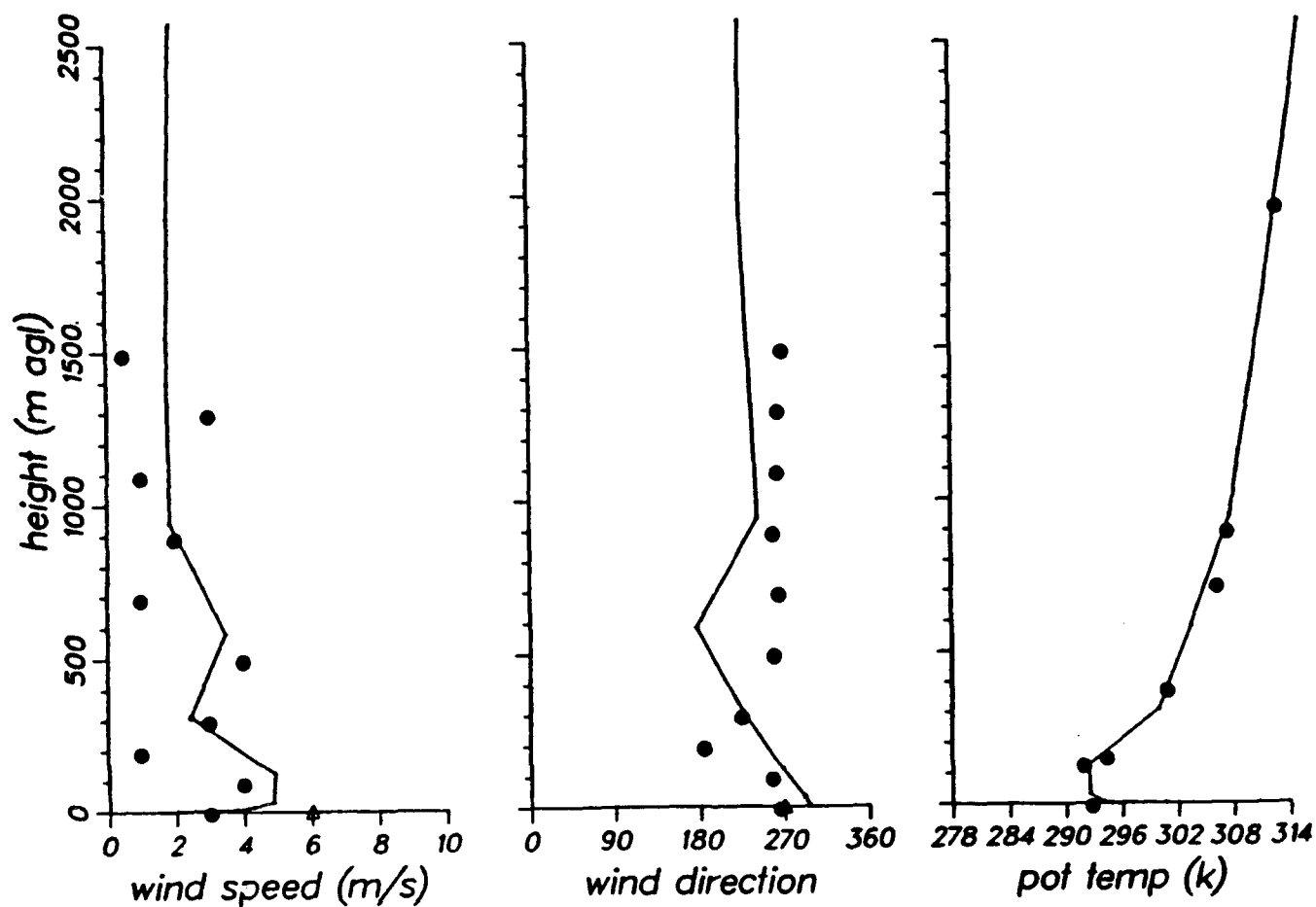


Figure 7. Vertical Profiles of the Modeled Wind Speed, Direction, and Potential Temperature for the MI87 Case at 1300 lst, June 13, 1966 at (a) BH, (b) HC, (c) SD, (d) VIP1, and (e) B22. Solid circles indicate observations.



Figure 8 shows the modeled ground-level exposure contours and Figure 9 shows the corresponding observation. An exposure value is computed by integrating concentration with time until the change in concentration becomes negligible. Then it is divided by the total amount of the materials released. The unit of exposure value is  $\text{s/m}^3$ . Figure 9 also shows the observed wind speeds and wind directions at the ground stations. The observed wind direction close to the release site is west-southwesterly, but it changes to westerly at the station slightly north of the release site. Our simulation (Figure 5) indicates that the wind direction is close to westerly at the release site. The observed plume apparently transported to the east-northeast direction despite the fact that wind directions measured at the ground stations suggest the plume should be transported to the east-southeast, which is the case for the modeled plume.

Although the modeled plume direction did not match the observed one, the modeled ground-level concentrations along the plume axis are in good agreement with observations, as shown in Table 1. It is not known why the observation at 3310 meters from the source shows the largest value among the observations.

TABLE 1: COMPARISON BETWEEN THE MODELED AND OBSERVED EXPOSURES FOR MI87 CASE

Modeled		Observed	
Distance from the source (m)	Exposure ( $\text{s/m}^3$ )	Distance from the source (m)	Exposure ( $\text{s/m}^3$ )
716	$8.04 \times 10^{-6}$	720	$3.97 \times 10^{-6}$
1253	$2.55 \times 10^{-6}$	1260	$1.08 \times 10^{-6}$
3312	$9.6 \times 10^{-7}$	3310	$5.39 \times 10^{-6}$
4403	$7.8 \times 10^{-7}$	4400	$3.02 \times 10^{-7}$

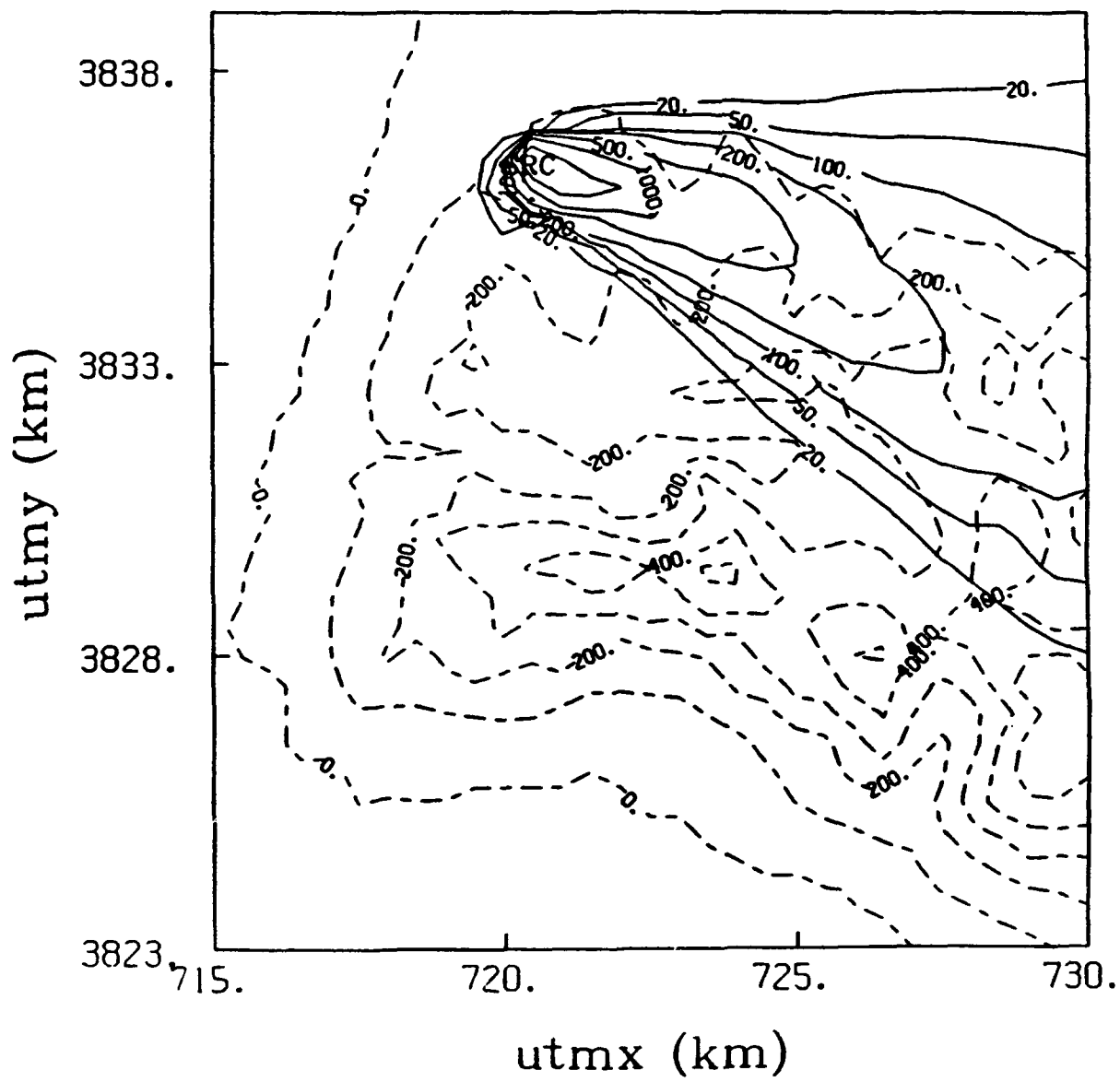


Figure 8. Modeled Ground Level Exposure Values of Fluorescent Particles for the MI87 Case. Units are  $\text{s/m}^3$ .

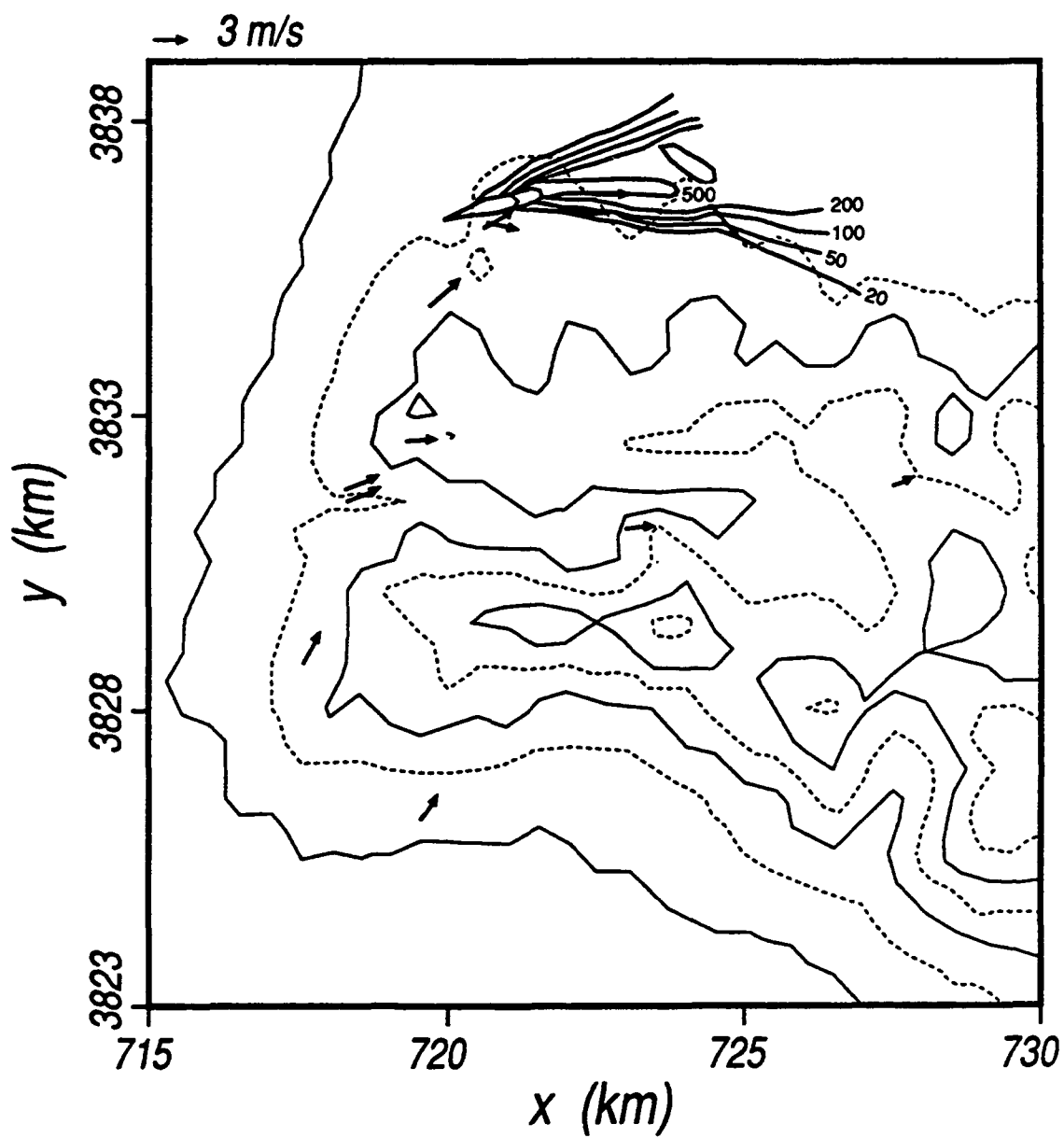


Figure 9. Same as in Figure 8 except the Observed Values are Contoured.

Finally, the modeled horizontal wind vectors in the outer grid at 14 meters above the ground at 1300 lst are shown in Figure 10 which indicates that a sea-breeze front penetrates deep inland since the sea breeze is enhanced by the flows developed over the slopes located near the eastern boundary of the study area.

## 2. MI90 Simulation

Meteorological conditions for the MI90 case are significantly different from those for the MI87 case. First, the prevailing wind speed for MI90 was close to 13.5 m/s compared with 2 m/s for MI87. Second, for MI90, a deep, well-mixed layer existed for the first 500 meters above the ground, which probably resulted from strong mixing caused by turbulence generated by high winds. On the other hand, the potential temperature profiles for MI87 exhibited shallow (100 meters ) mixed-layer depths, typical on the west coast as a result of large-scale subsidence.

The initial potential temperature profile was determined from the sounding at B22 site. The potential temperature lapse rate was almost neutral ( $0.0002^{\circ}\text{C}/\text{m}$ ) from the surface to 670 meters above msl,  $0.0611^{\circ}\text{C}/\text{m}$  between 670 and 880 meters above msl, and  $0.0070^{\circ}\text{C}/\text{m}$  above 880 meters above msl. Initial wind speed and direction were determined by examination of three upper air soundings (HC, SD, and B22) at 2300 lst. The wind profile at BH showed an extremely high wind speed (25 m/s) compared with those (13 m/s) at other sites. Thus, the BH profile was not considered in the determination of initial wind speed of 13.5 m/s and wind direction of 332 degrees which were used in the model.

The initial relative humidity profile was determined from the composite profiles at four sites (BH, HC, SD, and B22). The relative humidity was 80 percent at the ground and increased linearly with height to 92 percent at 670 meters above msl. Then, it decreased rapidly to 38 percent at 880 meters above msl. A constant value (38 percent) was used in the layers above 880 meters above msl.

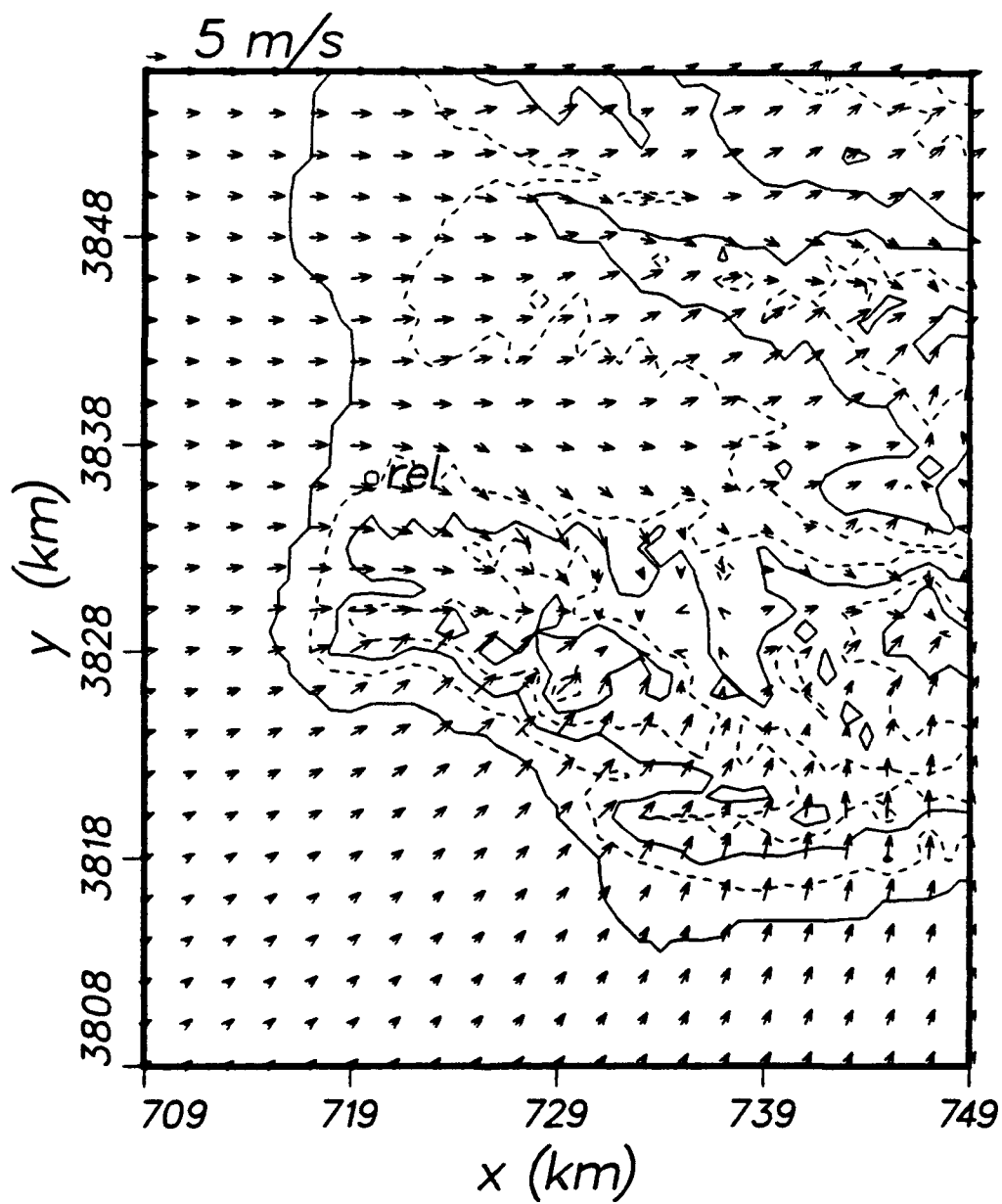


Figure 10. Same as in Figure 5 except in the Larger Computational Domain.

The computational domain is exactly the same as for the MI87 case:  $40 \times 48 \text{ km}^2$  with a horizontal grid spacing of 1 km, and the corresponding values for the nested inner grid are  $15 \times 16 \text{ km}^2$  and 0.5 km, respectively.

Integration started at 0600 1st, June 21, 1966, and continued for 24 hours until 0600 1st the following day. The plume was released for 30 minutes starting at 2300 1st, June 21, 1966. The plume was sampled for 2 hours in the model computation. By the end of 2 hours of sampling, the plume had left the computational domain, and the surface concentration values were practically zero.

The modeled horizontal wind vectors (Figure 11) at 10 meters above the ground at 2300, June 21, 1966 (Julian date 172), show very little variation because the prevailing wind is strong enough (13.5 m/s) to eliminate differential forcing generated by the topography. The observed horizontal wind vectors (Figure 12), on the other hand, show considerable spatial variations partly because the measurement heights at each site are different.

Vertical profiles of the modeled wind speed, wind direction, and potential temperature (Figures 13) are in fair agreement with observations. The observed wind speed profiles at HC and BH are quite different from those at B22 and VIP1, which exhibit normal variations. We are unable to find physical reasons for the extraordinary wind profiles at HC and BH, which were consistent over the time period between 2200 1st, June 21, and 0300 1st, June 22, 1966.

With the wind and turbulence distributions computed by HOTMAC, RAPTAD simulated the ground-level concentration contours (Figure 14), which are in good agreement with the observations (Figure 15). The observed exposures at 1870 and 5620 meters from the source were  $5.08 \times 10^{-6}$  and  $4.97 \times 10^{-7} \text{ s/m}^3$ , respectively. The corresponding modeled values at 1895 and 5603 meters from the source are  $1.83 \times 10^{-6}$  and  $3.45 \times 10^{-7} \text{ s/m}^3$ , respectively.

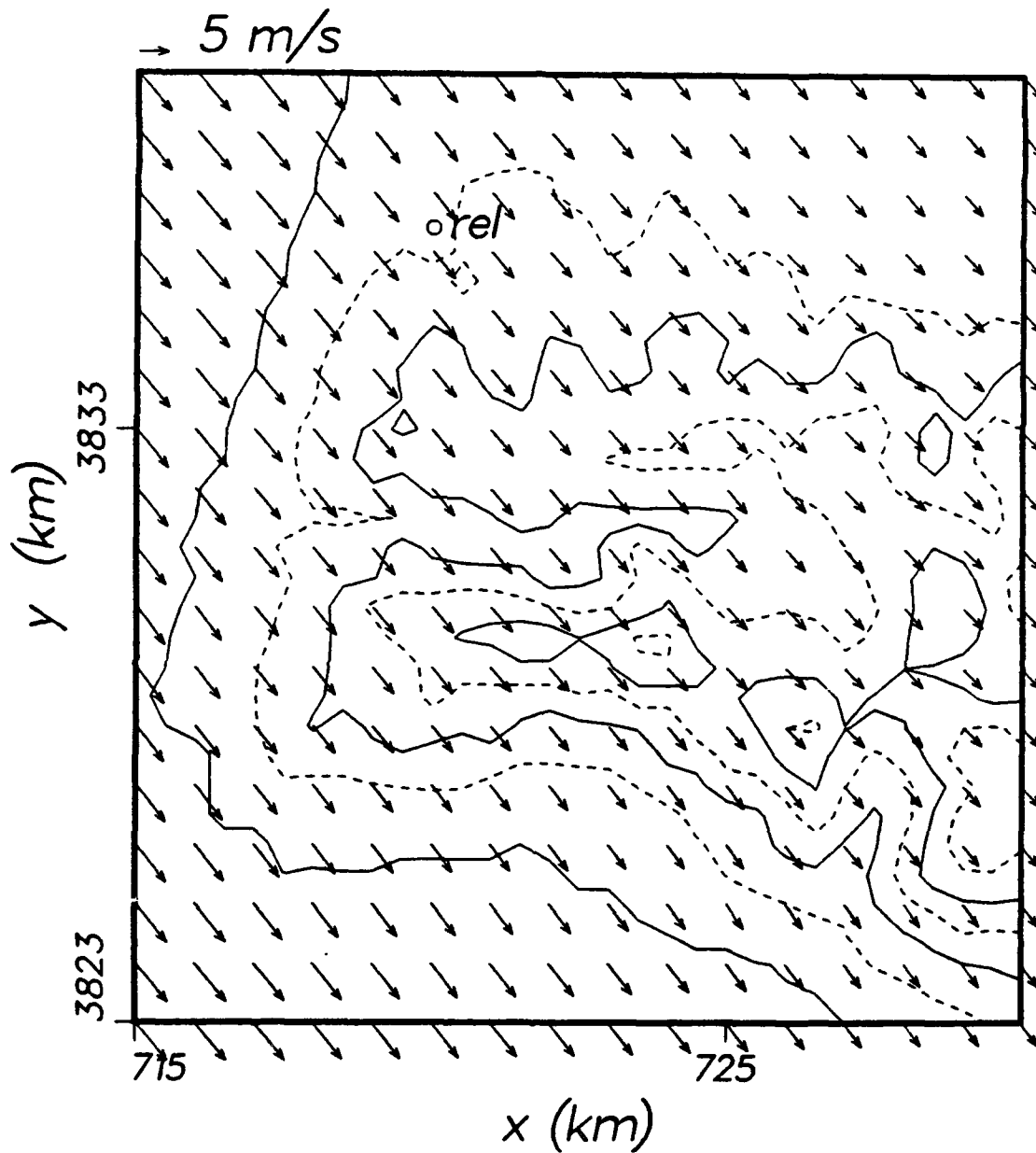


Figure 11. Modeled Horizontal Wind Vectors for the MI90 Case at 10 meters above the Ground at 2300 lst, June 21, 1966. Wind vectors at every other grid points are plotted. Terrain is contoured by solid lines with an increment of 200 meters. Dashed lines indicated contours halfway between the solid contours.

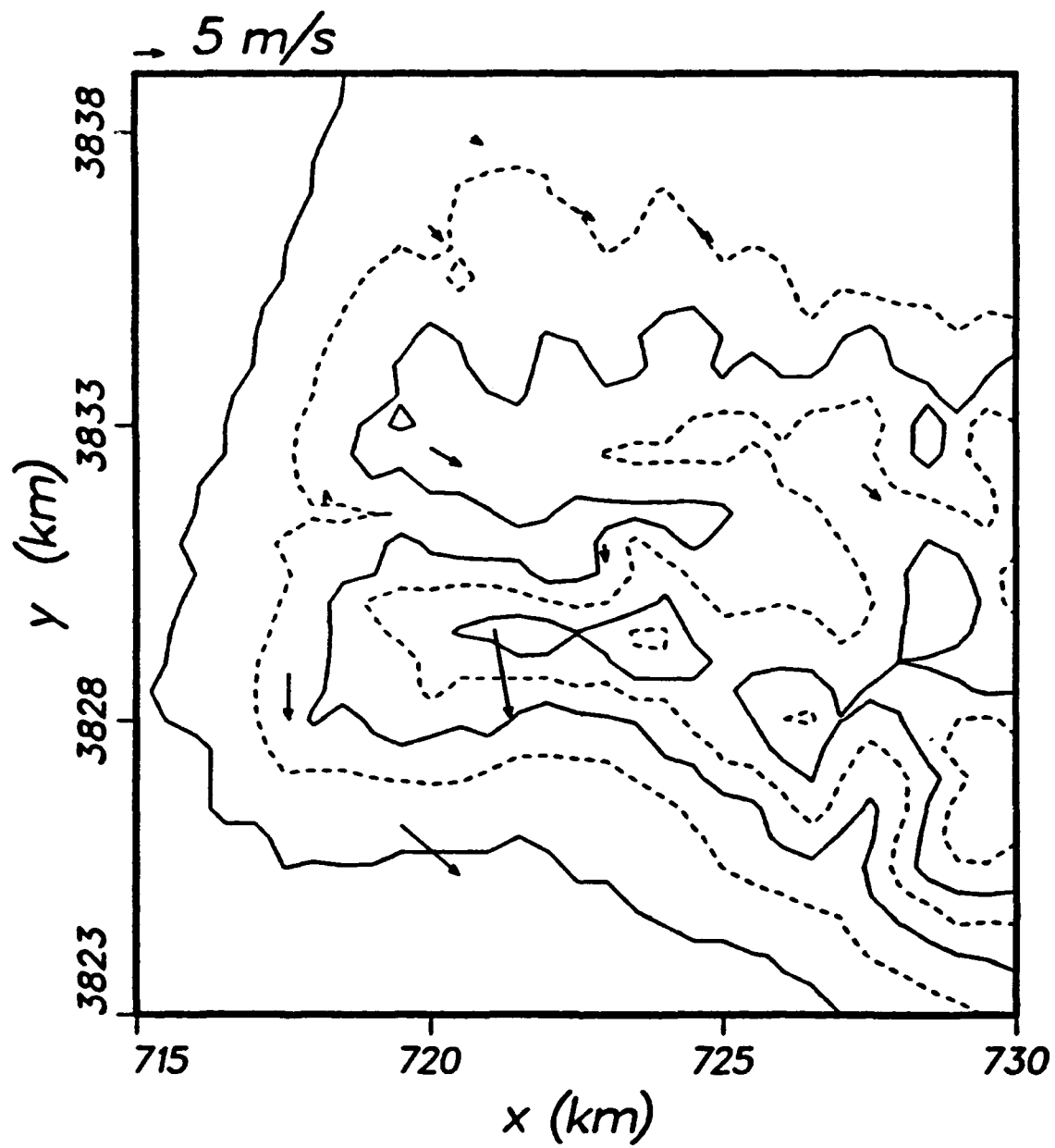


Figure 12. Same as in Figure 11 except Observed Wind Vectors in the Surface Layer are Shown.



MI90 BH 2300

(a)

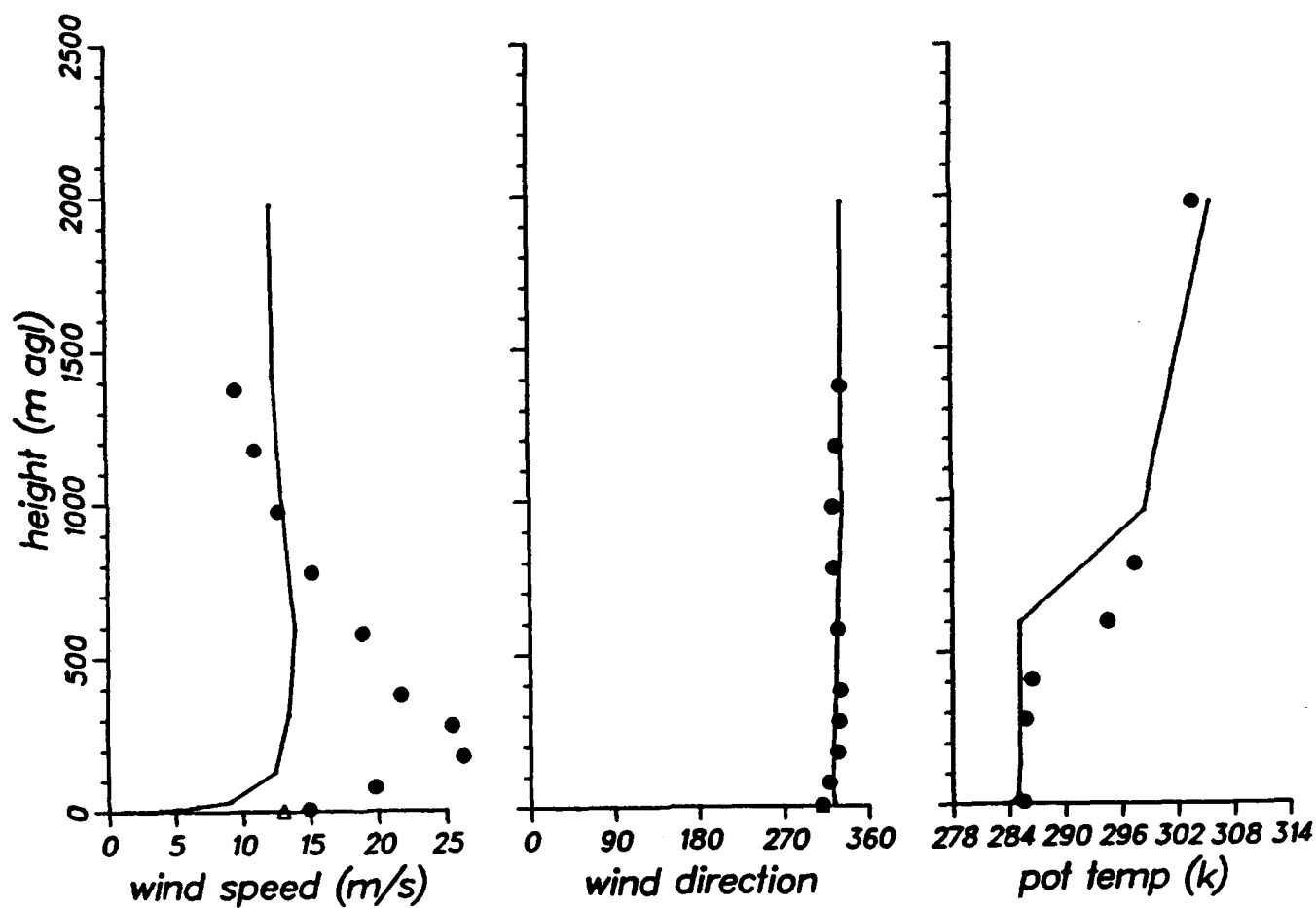


Figure 13. Vertical Profiles of the Modeled Wind Speed, Direction, and Potential Temperature for the MI90 Case at 2300 lst, June 21, 1966 at (a) BH, (b) HC, (c) SD, (d) VIP1 and (e) B22. Solid circles indicate observations.

MI90 HC 2300

(b)

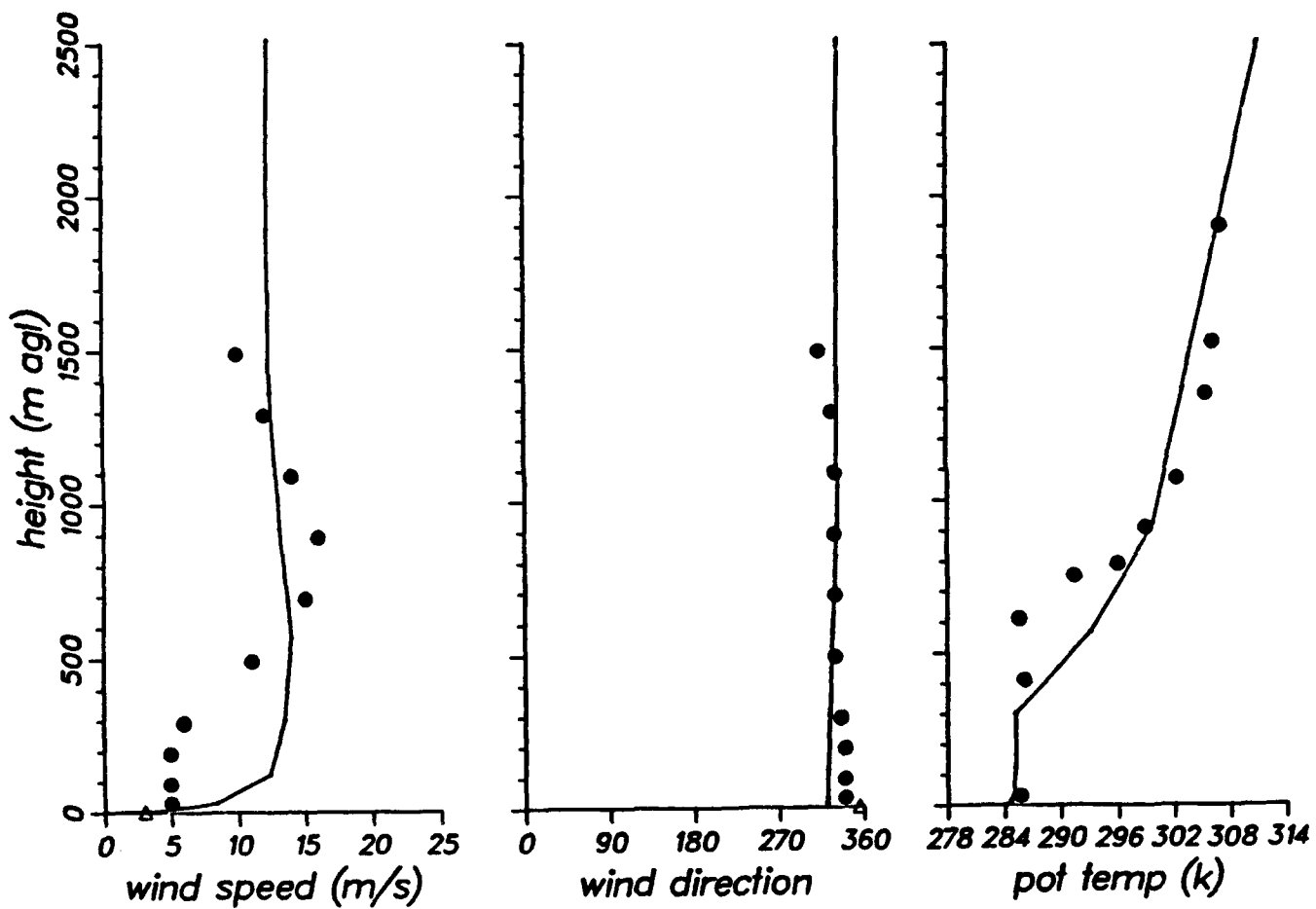


Figure 13. Vertical Profiles of the Modeled Wind Speed, Direction, and Potential Temperature for the MI90 Case at 2300 lst, June 21, 1966 at (a) BH, (b) HC, (c) SD, (d) VIP1 and (e) B22. Solid circles indicate observations.

MI90 SD 2300

(c)

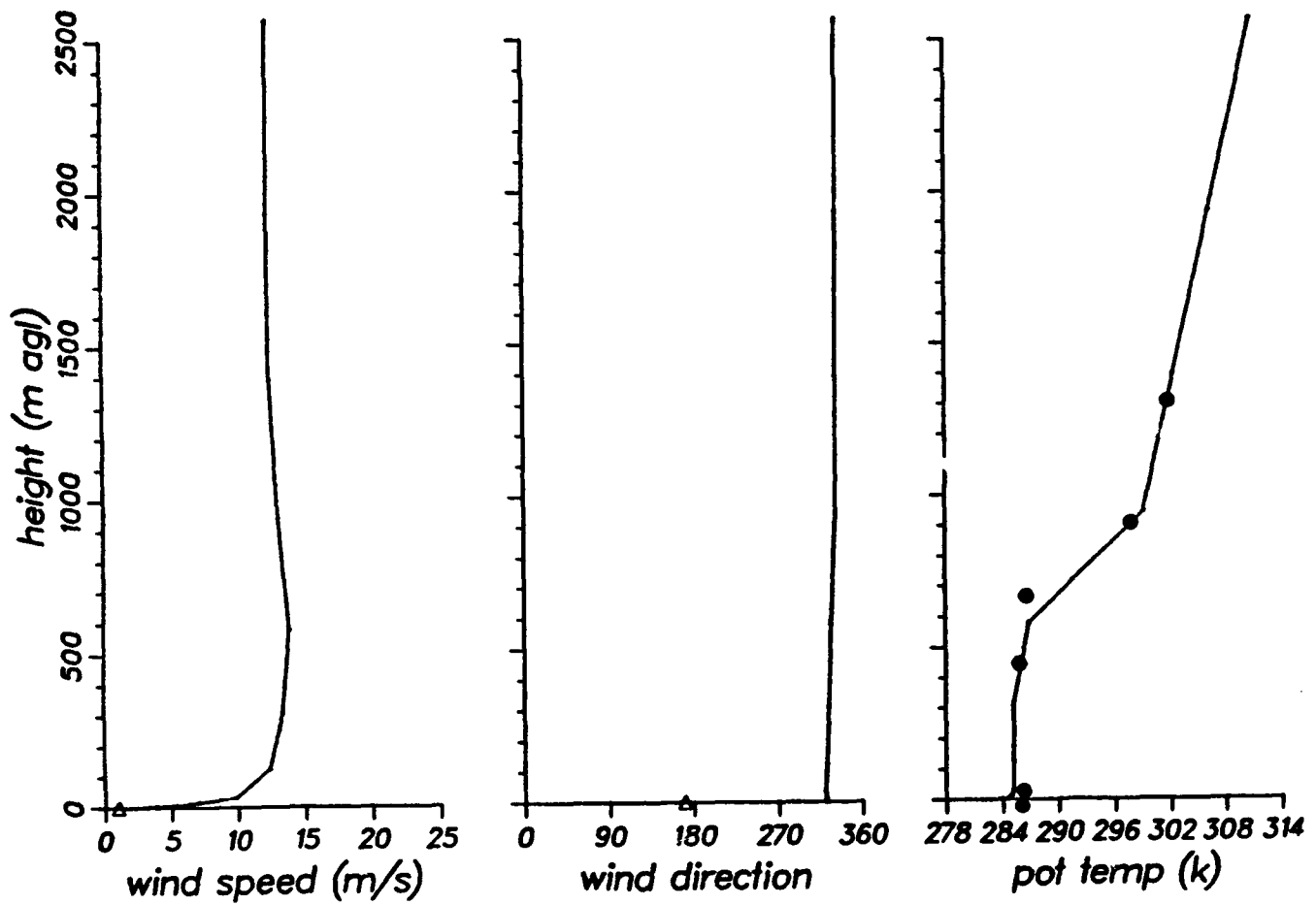


Figure 13. Vertical Profiles of the Modeled Wind Speed, Direction, and Potential Temperature for the MI90 Case at 2300 lst, June 21, 1966 at (a) BH, (b) HC, (c) SD, (d) VIP1 and (e) B22. Solid circles indicate observations.

MI90 VIP1 2300

(d)

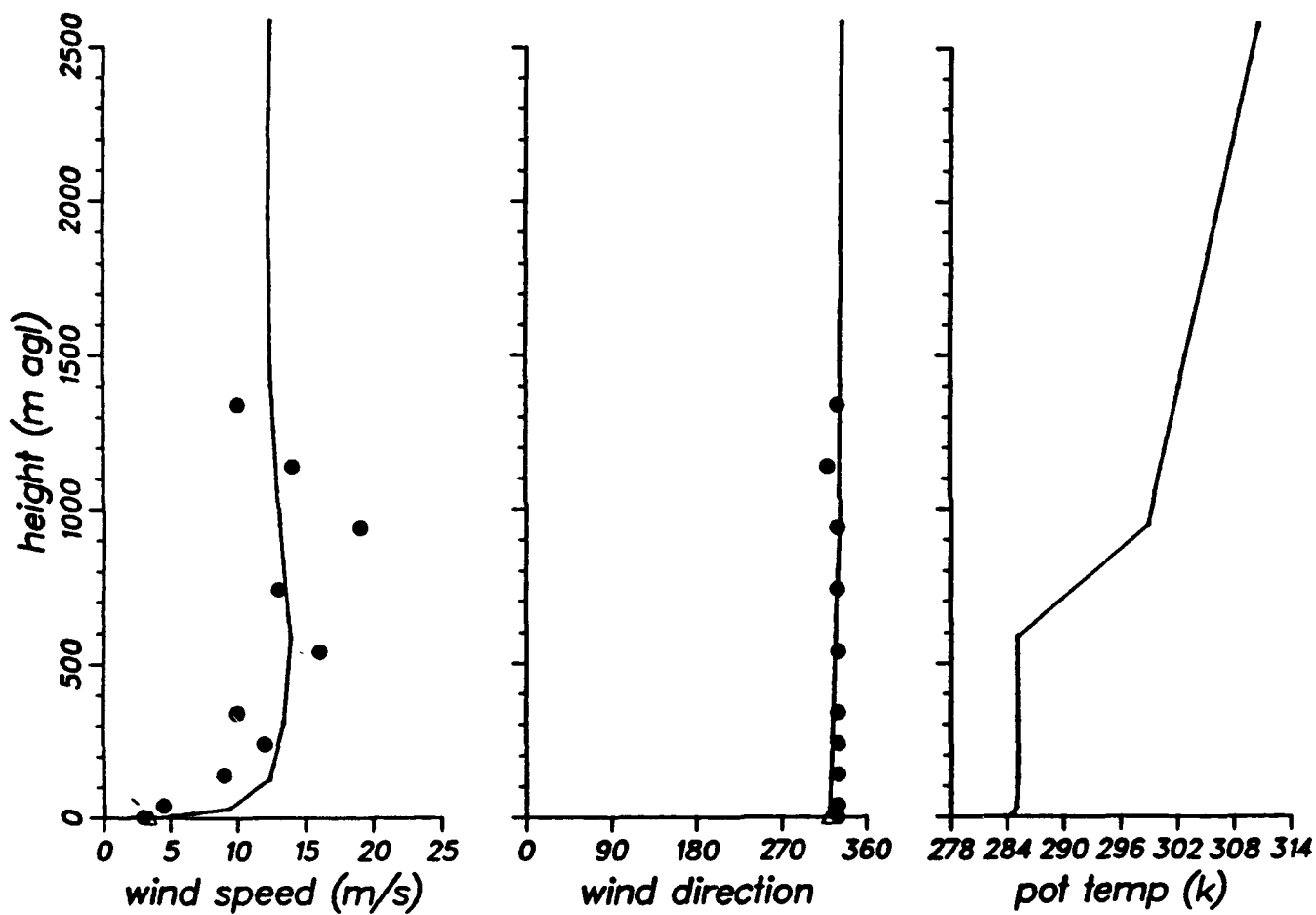


Figure 13. Vertical Profiles of the Modeled Wind Speed, Direction, and Potential Temperature for the MI90 Case at 2300 lst, June 21, 1966 at (a) BH, (b) HC, (c) SD, (d) VIP1 and (e) B22. Solid circles indicate observations.

MI90 B22 2300

(e)

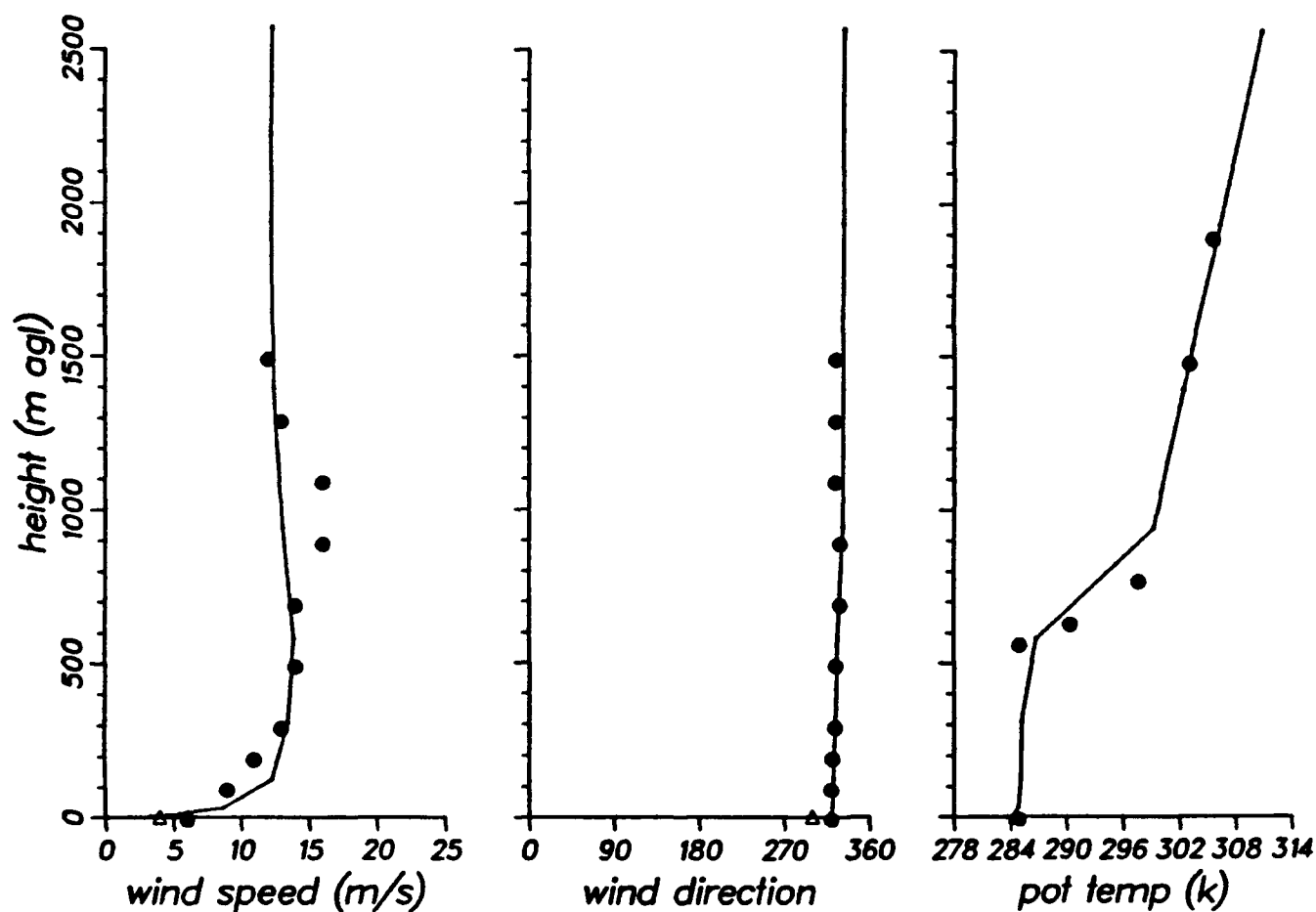


Figure 13. Vertical Profiles of the Modeled Wind Speed, Direction, and Potential Temperature for the MI90 Case at 2300 lst, June 21, 1966 at (a) BH, (b) HC, (c) SD, (d) VIP1 and (e) B22. Solid circles indicate observations.

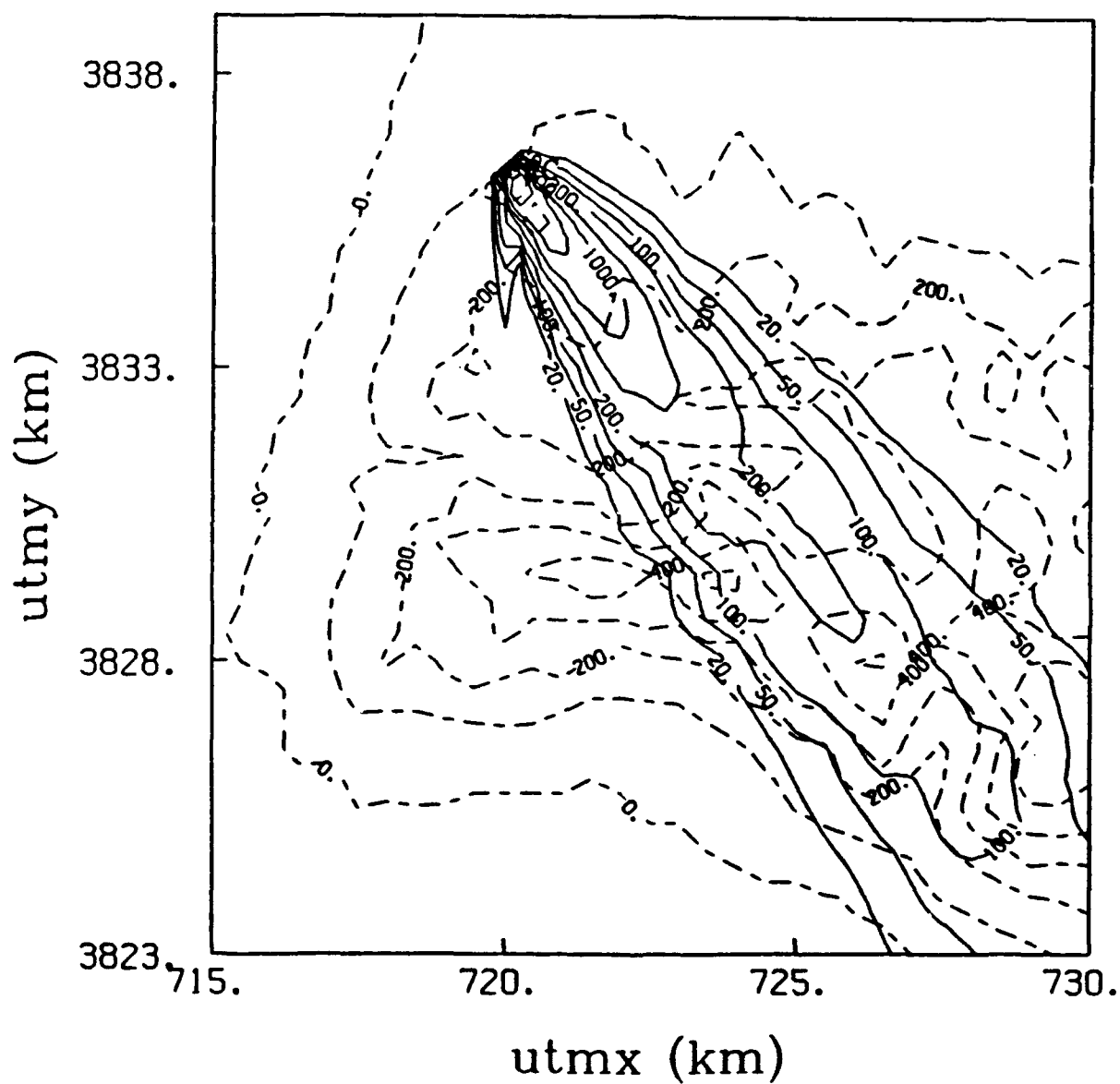


Figure 14. Modeled Ground Level Exposures of Fluorescent Particles for the MI90 Case.  
Units are  $\text{s/m}^3$ .

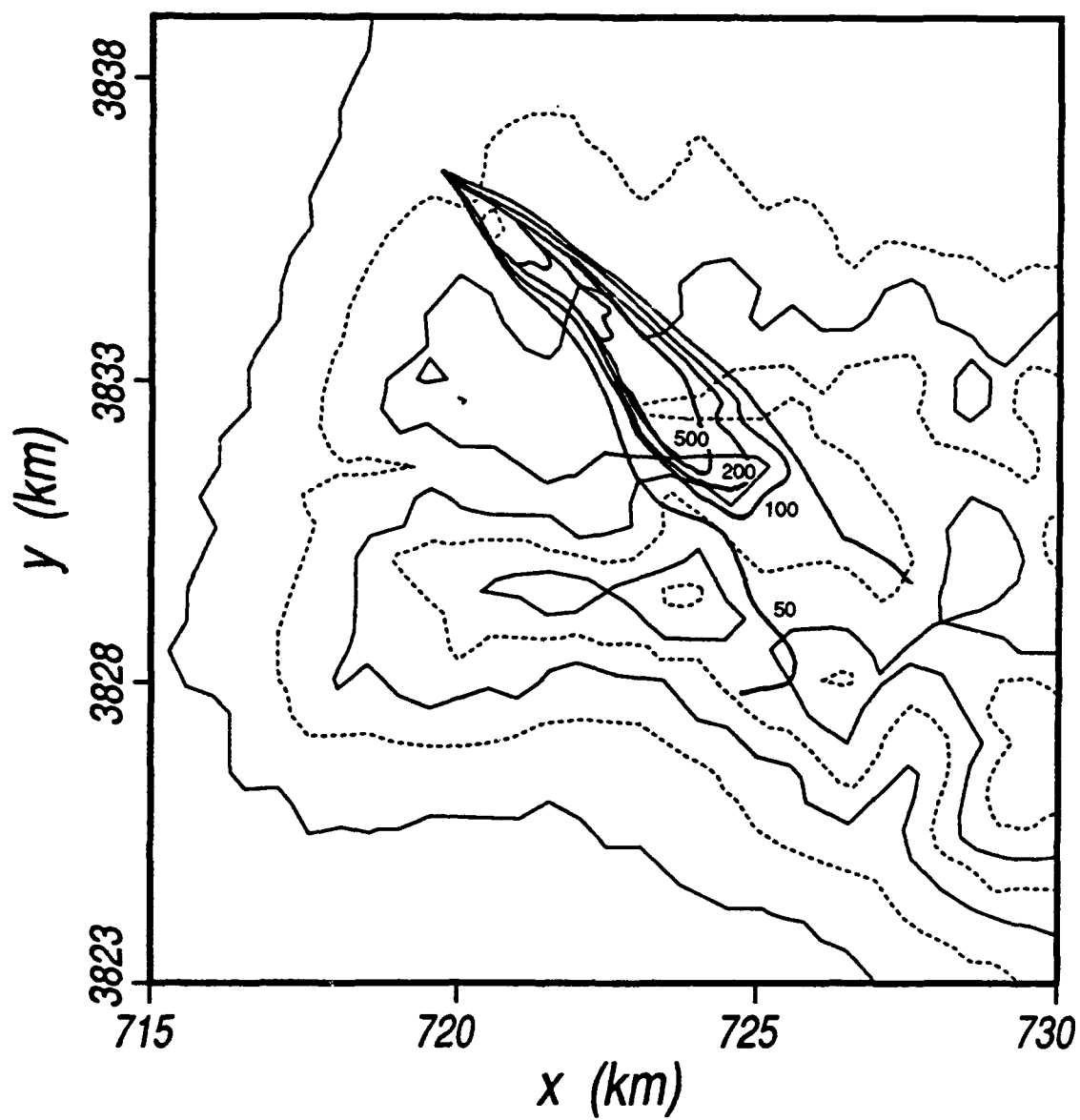


Figure 15. Same as in Figure 14 except the Observed Values are Contoured.

### 3. MI91 Simulation

The MI91 release was at 0203 lst, June 22, 1966 which is only 3 hours after the MI90 release. However, the wind direction changed considerably to northerly, as much as 30 degrees from the MI90 case. Based on the MI91 data log, the wind direction veering from northwest to north occurred around midnight June 21, 1966 and was more evident in the layers between 300 and 1300 meters above msl. At the present time, there is no valid documentation to explain how the sudden wind direction shift occurred except that the MI90 data log suggested a possible postfrontal (i.e., synoptically forced) effect.

The maximum wind veering occurred at around 800 meters above msl, and a sine curve appears to represent well the vertical profiles of the wind direction change between 300 and 1300 meters above msl. Thus, wind directions at the grid levels between 300 and 1300 meters above msl were nudged toward the observed wind directions. We started the HOTMAC computation with the wind direction nudging. The output at 2300 from the MI90 simulation was used to initialize the model variables.

The modeled horizontal wind vectors (Figure 16) clearly indicate that the wind directions have shifted from the corresponding values for the MI90 case (Figure 11). The nudging was not applied to the layers in the first 300 meters above the ground, but the surface layer winds (Figure 16) are clearly influenced by the nudging. This good communication between the surface and upper level winds apparently resulted from the strong vertical mixing resulting from extraordinary large turbulence (Figure 17) for a nocturnal period. The high prevailing wind speed (13.5 m/s) is responsible for the large turbulence values.

Unlike the modeled horizontal wind vectors at 10 meters above the ground (Figure 16), the observed surface wind distribution for MI91 (Figure 18) is not much different from the corresponding distribution for MI90 (Figure 12).



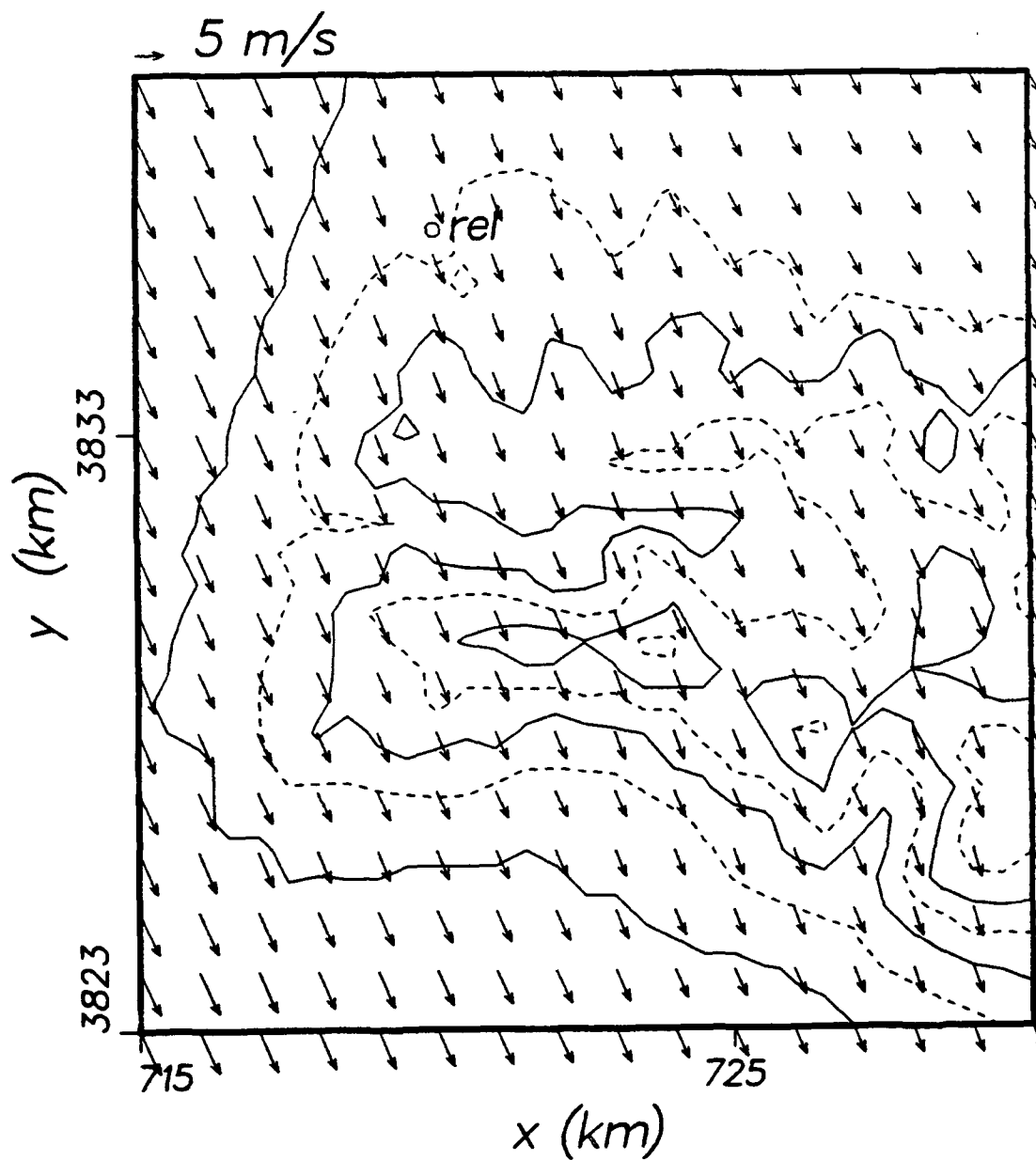


Figure 16. Modeled Horizontal Wind Vectors for the MI91 Case at 10 meters above the Ground at 0200 lst, June 22, 1966. Wind vectors are plotted at every other grid point. Terrain is contoured by solid lines with an increment of 200 meters. Dashed lines indicate contours halfway between the solid contours.

site vip1 day 173 200 lst grid 2

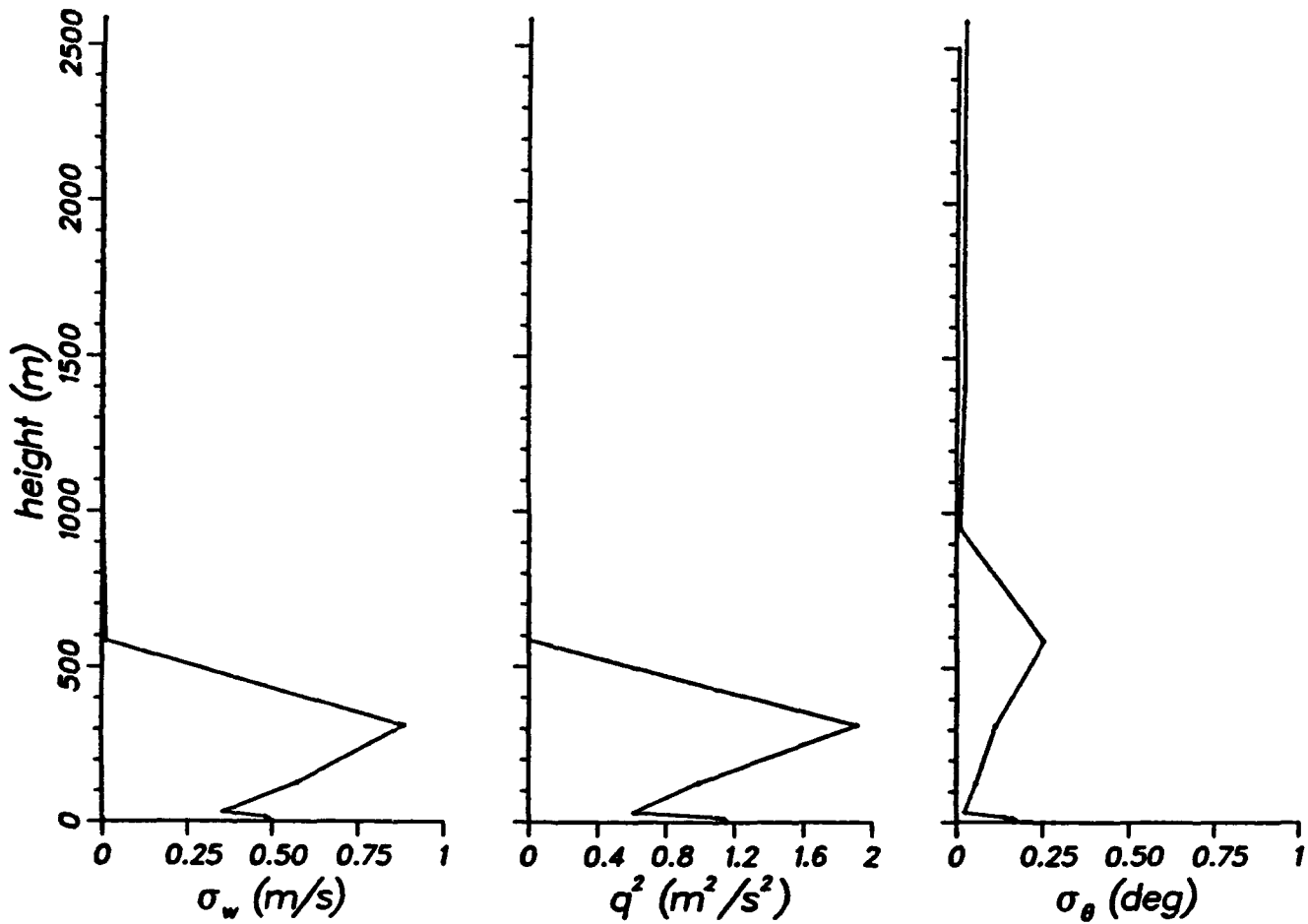


Figure 17. Vertical Profiles of the Modeled Standard Deviation of Vertical Wind Component, Turbulence Kinetic Energy, and Standard Deviation of Potential Temperature at VIP1 at 0200 lst, June 22, 1966.

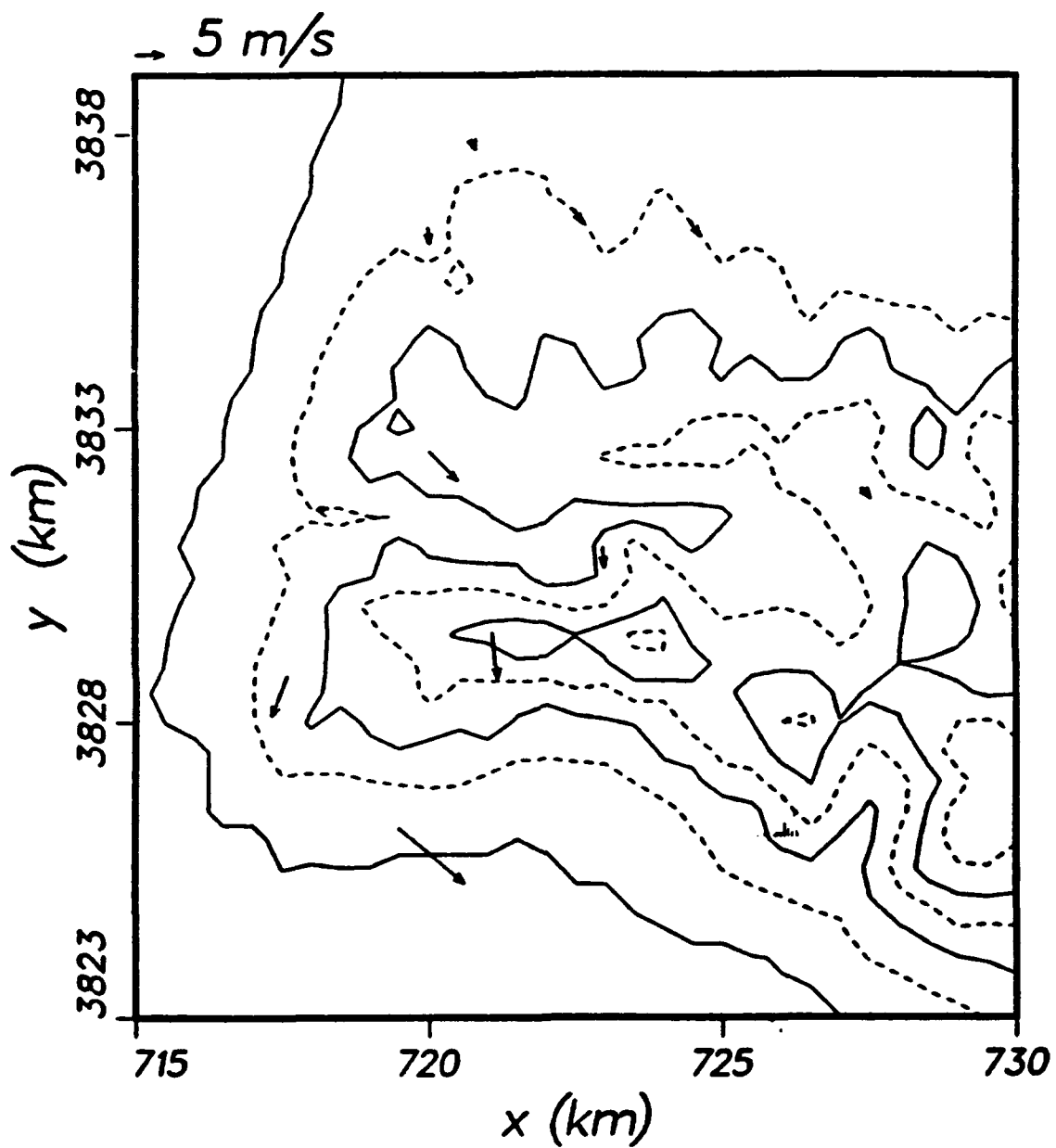


Figure 18. Same as in Figure 16 except Observed Wind Vectors in the Surface Layer are Shown.

Vertical profiles of the modeled wind speed, wind direction, and potential temperature (Figure 19) are in fair agreement with observations: the modeled wind direction with the nudging are in good agreement with measurements, but wind speed and temperature profiles are quite different from the observations. The MI91 data log hinted that the postfrontal disturbance might have caused the veering and strong warming in the boundary layer, but the description was not good enough for us to implement the large-scale variations in HOTMAC.

Using the wind and turbulence distributions computed by HOTMAC, RAPTAD simulated ground-level concentration contours (Figure 20) which are in good agreement with the observations (Figure 21). The observations appear to indicate a minimum value in Honda Canyon, and the plume axis is more northerly than the modeled plume axis. The modeled exposures along the plume axis are in good agreement with the observations at nearby locations as shown in Table 2.

TABLE 2: COMPARISON BETWEEN THE MODELED AND OBSERVED EXPOSURES FOR MI91 CASE.

Modeled		Observed	
Distance from the source (m)	Exposure (s/m <sup>3</sup> )	Distance from the source (m)	Exposure (s/m <sup>3</sup> )
1254	$3.30 \times 10^{-6}$	1270	$4.09 \times 10^{-6}$
2672	$1.03 \times 10^{-6}$	2670	$1.54 \times 10^{-6}$
4253	$6.98 \times 10^{-7}$	4220	$9.11 \times 10^{-7}$
5005	$5.45 \times 10^{-7}$	4950	$2.42 \times 10^{-7}$
7139	$3.15 \times 10^{-7}$	7130	$2.02 \times 10^{-7}$
10030	$1.06 \times 10^{-7}$	10000	$5.07 \times 10^{-8}$

MI91 BH 200

(a)

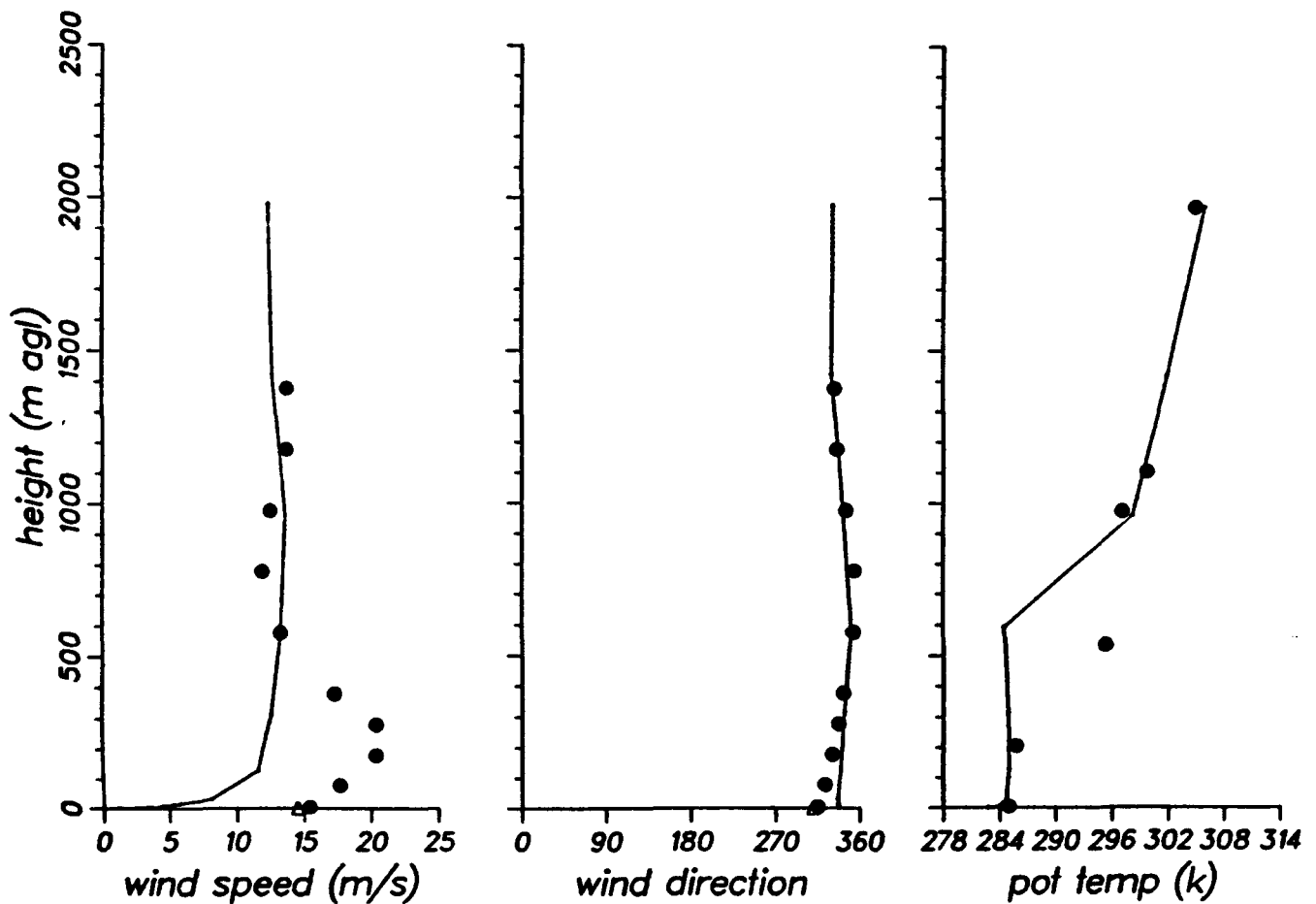


Figure 19. Vertical Profiles of the Modeled Wind Speed, Direction, and Potential Temperature for the MI91 Case at 0200 lst, June 17, 1966 at (a) BH, (b) HC, (c) SD, (d) VIP1, and (e) B22. Solid circles indicate observations.

MI91 HC 200

(b)

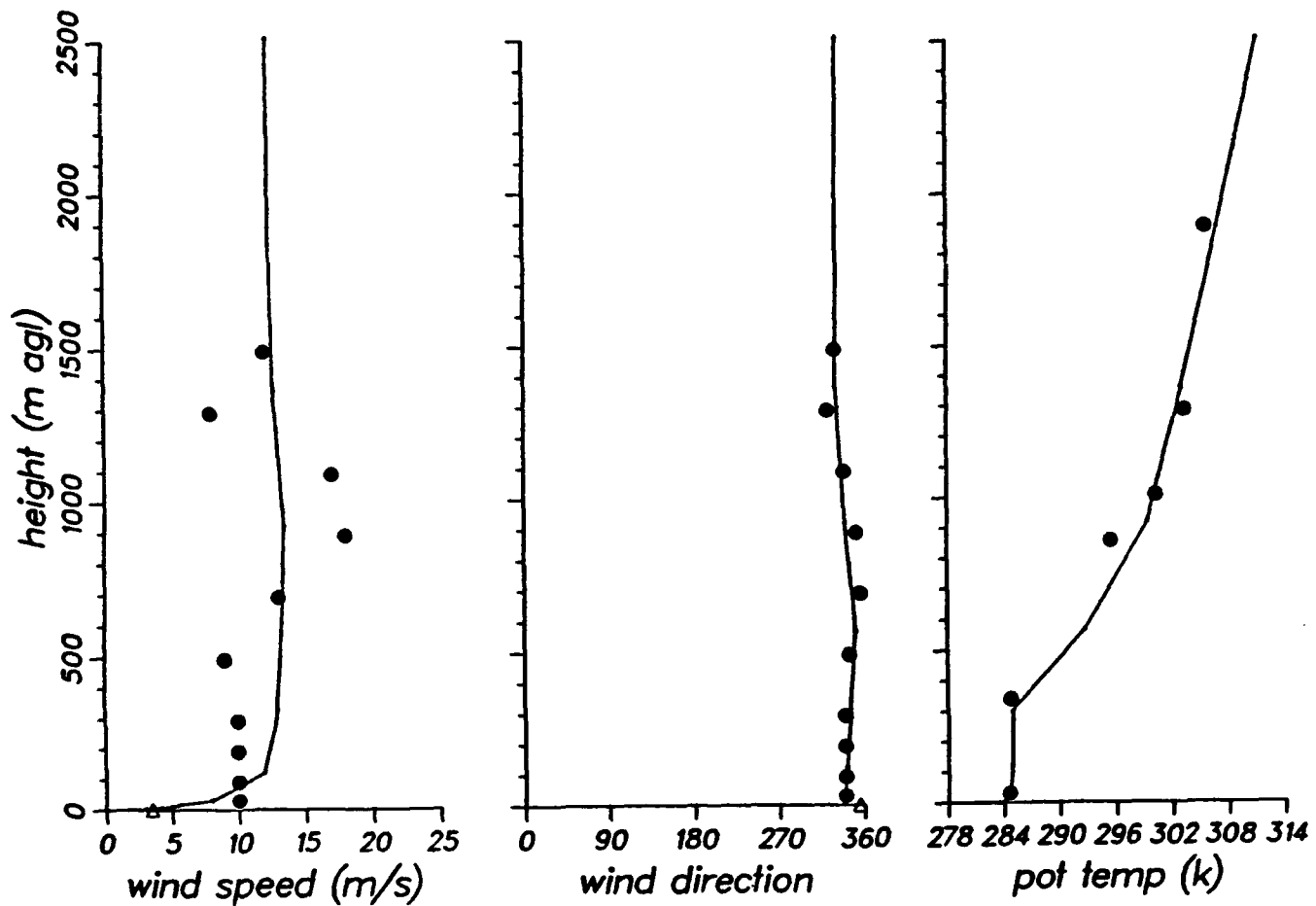


Figure 19. Vertical Profiles of the Modeled Wind Speed, Direction, and Potential Temperature for the MI91 Case at 0200 lst, June 17, 1966 at (a) BH, (b) HC, (c) SD, (d) VIP1, and (e) B22. Solid circles indicate observations.

MI91 SD 200

(c)

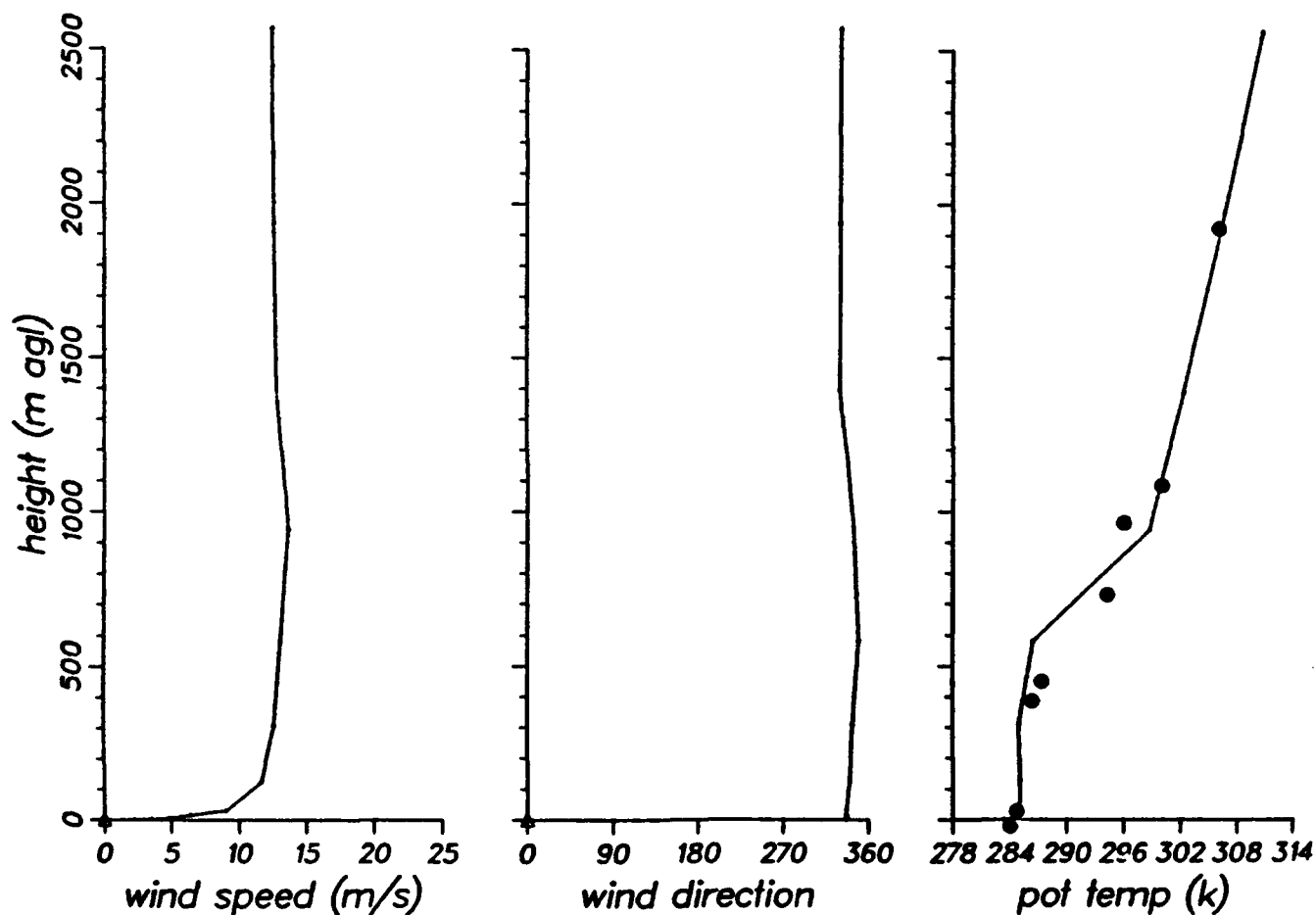


Figure 19. Vertical Profiles of the Modeled Wind Speed, Direction, and Potential Temperature for the MI91 Case at 0200 lst, June 17, 1966 at (a) BH, (b) HC, (c) SD, (d) VIP1, and (e) B22. Solid circles indicate observations.

MI91 VIP1 200

(d)

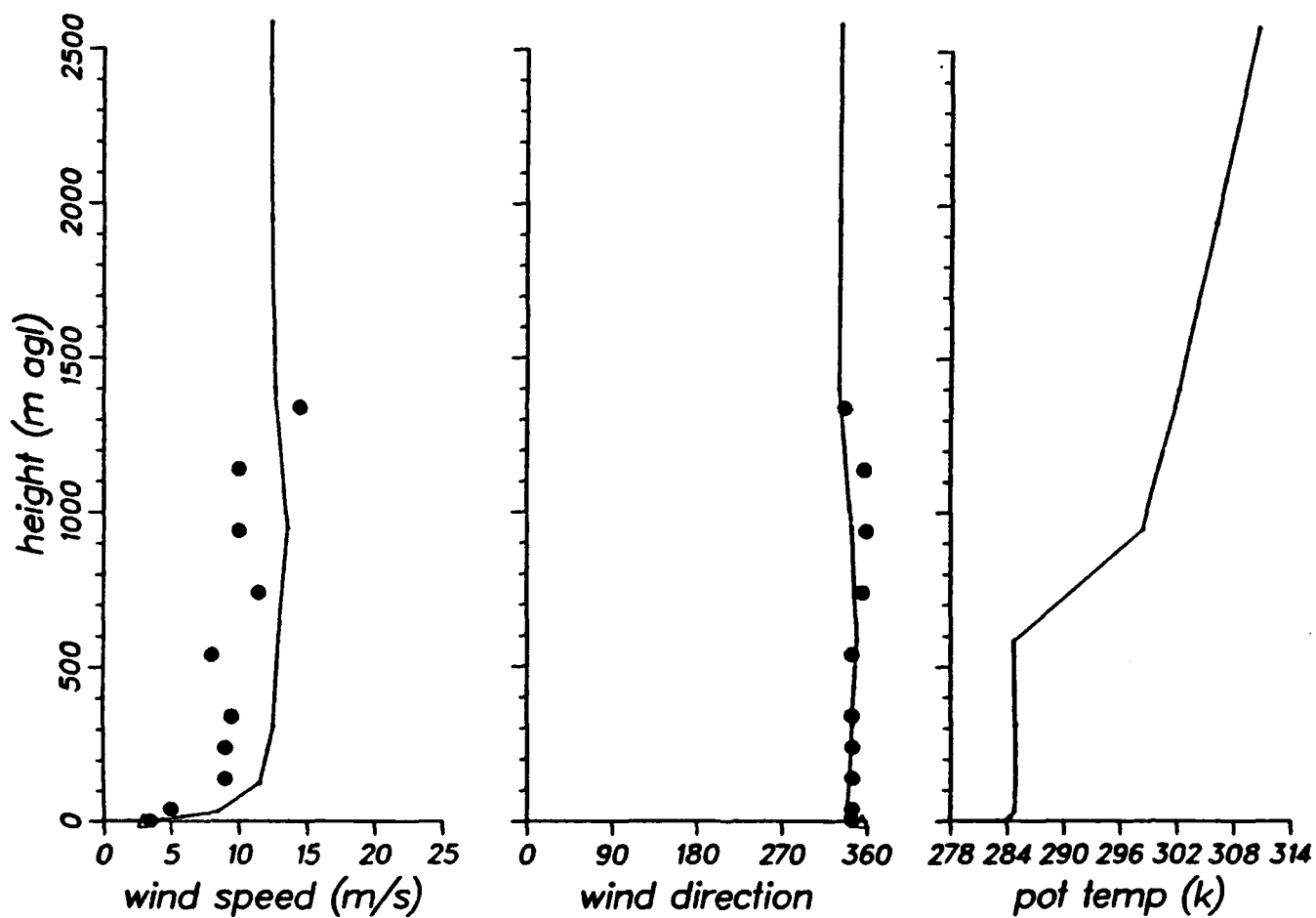


Figure 19. Vertical Profiles of the Modeled Wind Speed, Direction, and Potential Temperature for the MI91 Case at 0200 lst, June 17, 1966 at (a) BH, (b) HC, (c) SD, (d) VIP1, and (e) B22. Solid circles indicate observations.



MI91 BD22 200

(e)

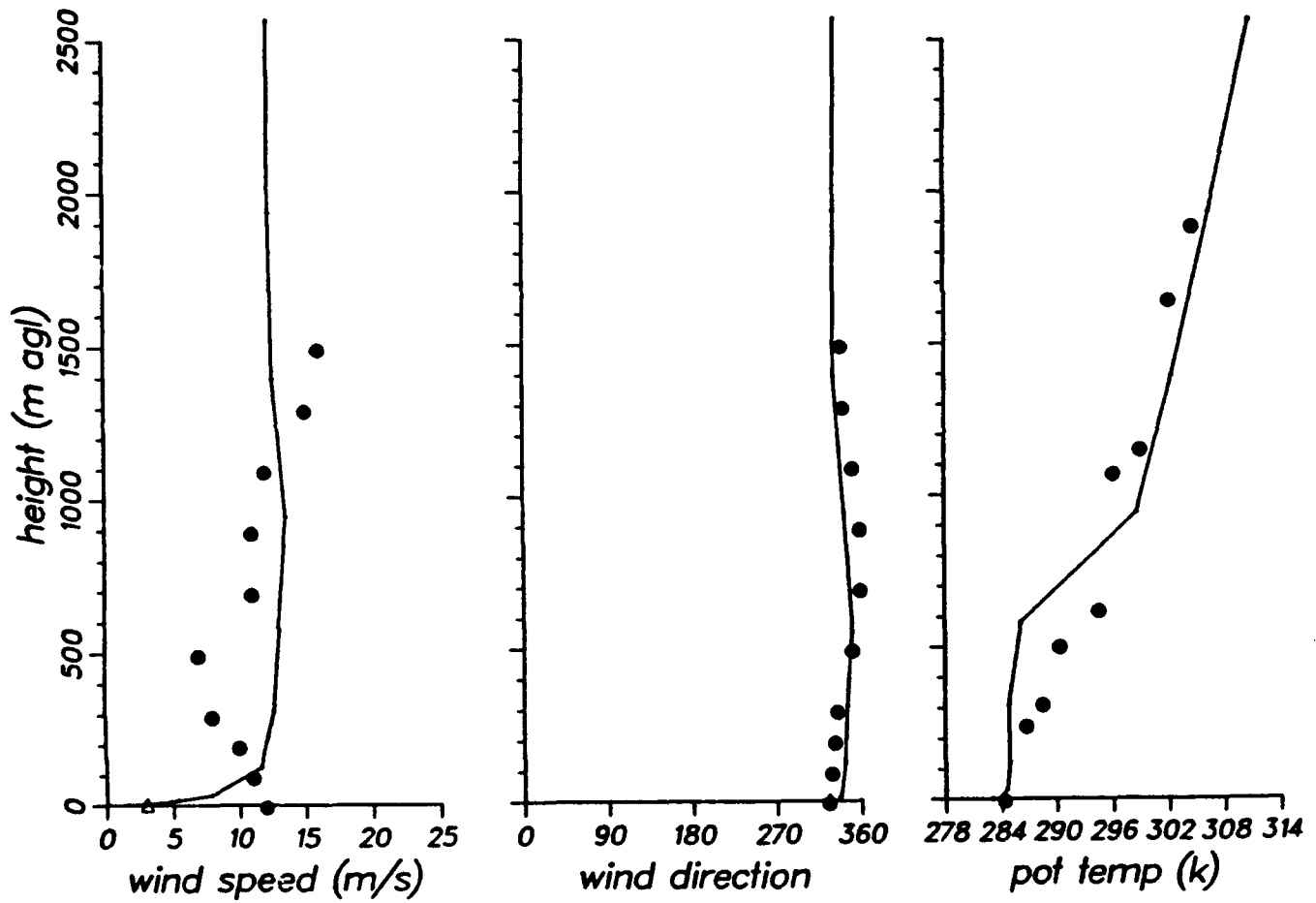


Figure 19. Vertical Profiles of the Modeled Wind Speed, Direction, and Potential Temperature for the MI91 Case at 0200 lst, June 17, 1966 at (a) BH, (b) HC, (c) SD, (d) VIP1, and (e) B22. Solid circles indicate observations.

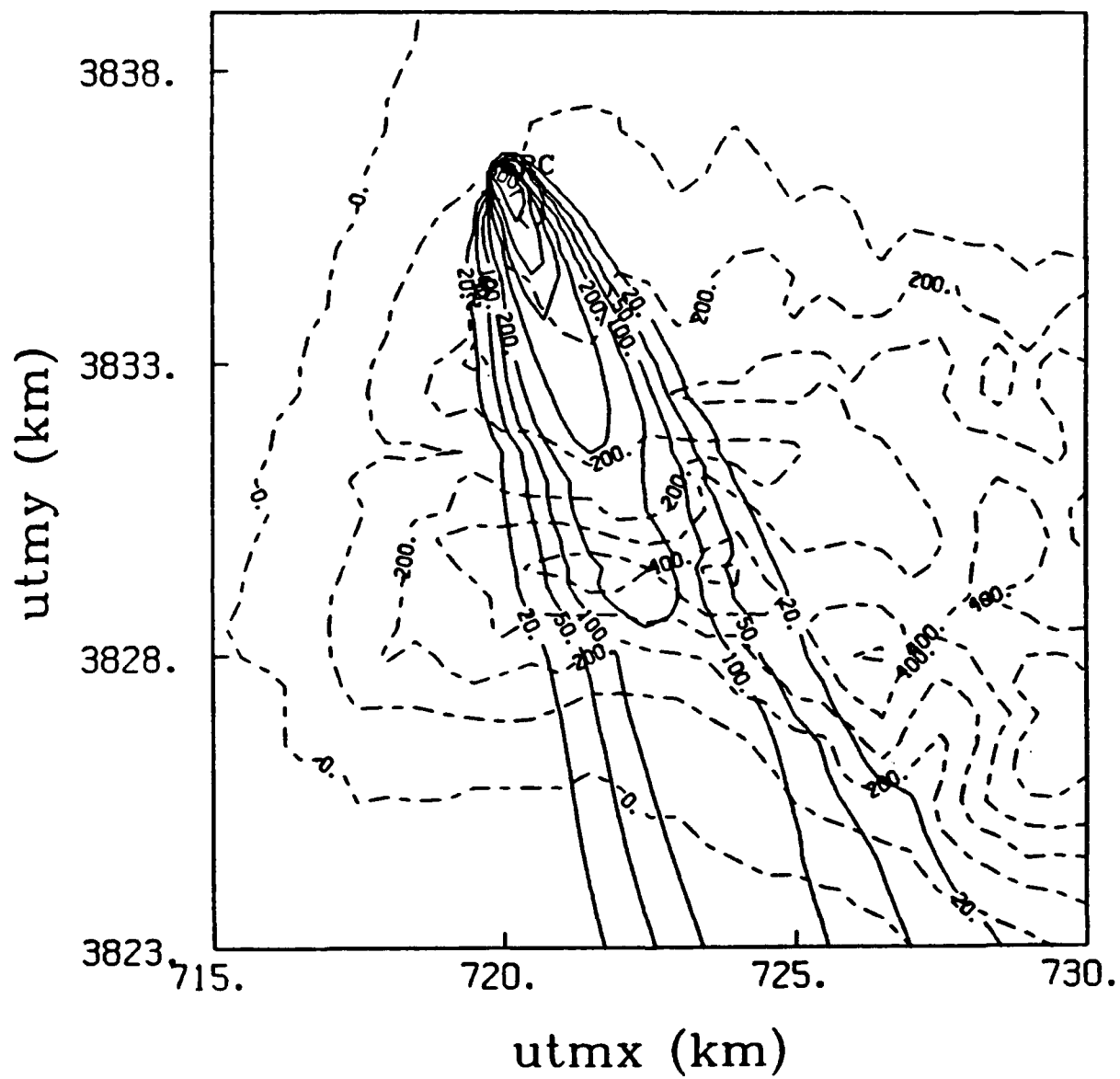


Figure 20. Modeled Ground Level Exposures of Fluorescent Particles for the MI91 Case.  
Units are  $\text{s/m}^3$

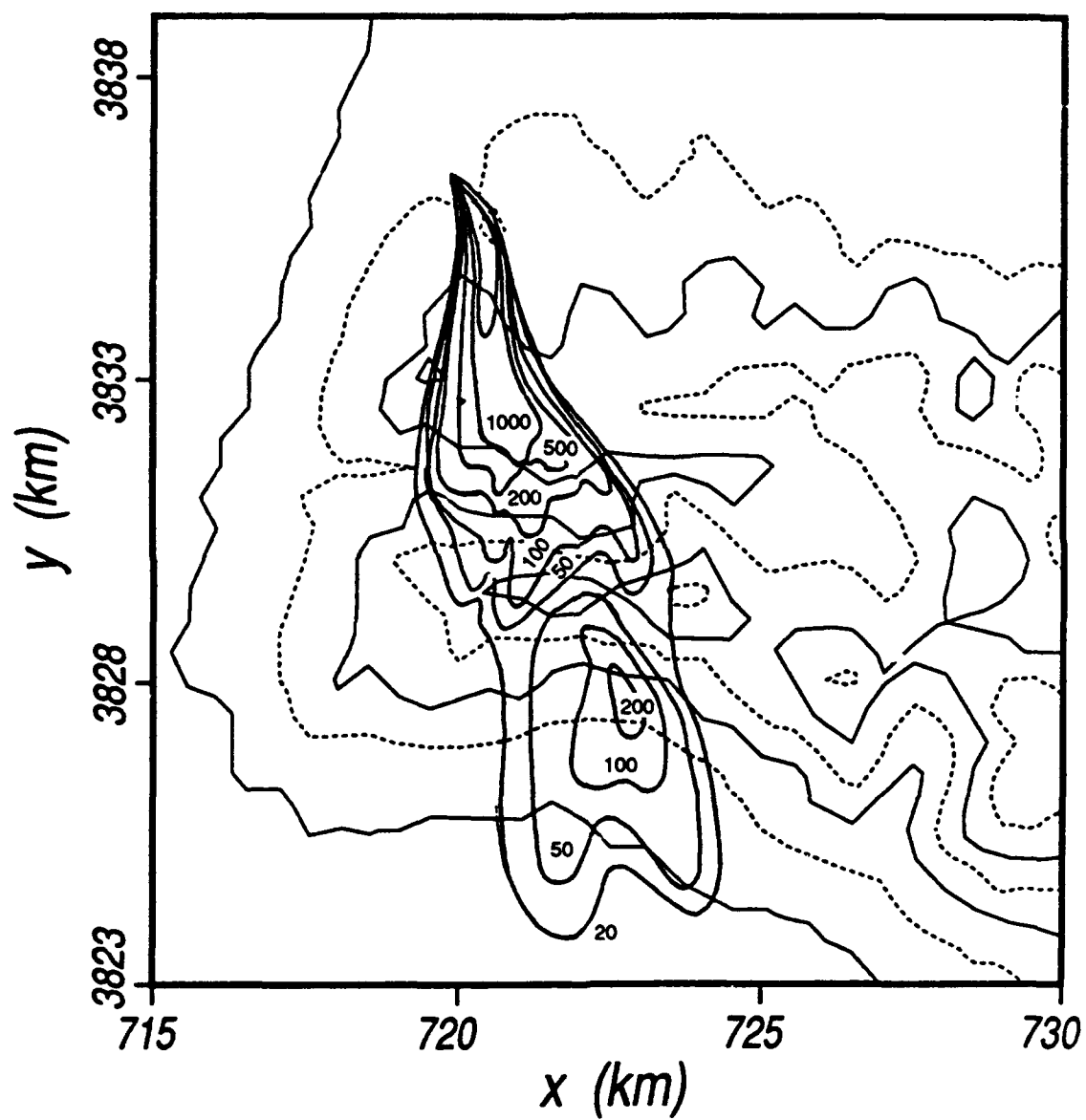


Figure 21. Same as in Figure 20 except the Observed Values are Contoured.

The HOTMAC and RAPTAD modeling system produced surface exposures along the plume axis at least as good as those obtained by diagnostic models and an empirical formula specifically adjusted to the MI data. The real strength of a prognostic model such as HOTMAC is realized where wind data are not available. Under such conditions, only prognostic models can provide a realistic solution which considers complex surface conditions. In the following section, the HOTMAC and RAPTAD results are compared with those obtained by diagnostic models and AF models currently used at VAFB.

## SECTION V

### MODEL COMPARISONS

There were a few attempts in the past to simulate the MI wind and concentration data. Hunter (Reference 12) investigated the performance of a diagnostic wind model WOCSS for eight cases of the MI data. Thykier—Nielsen et al. (Reference 13) tested a diagnostic wind model (LINCOM) and a puff model (RIMPUFF) for two cases of the MI data. The data common to both studies were the MI87 and MI90 cases. Therefore, we use these two cases to compare the performances of WOCSS, LINCOM, RIMPUFF, HOTMAC, and RAPTAD, and discuss the strengths and weaknesses of each model. The present comparisons are qualitative and informal because none of the model results presented here has experienced the formal review normally required for journal publication.

#### A. WIND MODEL

There are two classes of wind models: diagnostic and prognostic. Diagnostic wind models are based on measurements and interpolation. Most of these models adjust initially interpolated wind fields to satisfy a mass conservation equation. The accuracy of the model results is greatly dependent upon the quality and representativeness of measurements.

Diagnostic wind models have been used almost exclusively for emergency response management because they are simple and fast. The critical weakness of this class of models, however, is the lack of predictive capability. Plume models based on a diagnostic wind model must assume that the current wind field will persist until it is updated by future measurements. The assumption of persistency is adequate if the measurements are made frequently and if no abrupt change in wind field is expected. However, such conditions limit the area of concern to the immediate vicinity of the source and exclude predictions during the transitional periods.

The question of the representativeness of measurements further limits the applications of diagnostic wind models to simple terrains, because complex surface boundaries require a prohibitively large number of wind measurements.

Prognostic models, on the other hand, solve a set of time-dependent physical equations, such as conservation equations of momentum, internal energy, and mixing ratio of water vapor. Prognostic models forecast three-dimensional distributions of wind field that become the input to transport and diffusion models.

At present, prognostic models are not used in emergency response systems because a large amount of computation time is required. The situation should be improved considerably in the near future, because the capabilities of engineering workstations are expected to advance at an astonishing rate.

Figure 22 shows the modeled horizontal wind vectors for the MI87 case at 4 meters above ground level (agl) at 1310 lst by using WOCSS diagnostic wind model (Reference 12). An array of 50 x 80 x 6 with 500 meter grid spacing and the terrain data of a 500 meter resolution were used. Wind vectors at every fourth grid point are shown in Figure 22.

Figure 23 shows the modeled wind vectors for the MI87 case at 10 meters agl at 1310 lst by using LINCOM (Reference 13), which is a linear, diagnostic, spectral, and potential-flow wind model.

Both WOCSS and LINCOM used the same tower data and wind fields were adjusted to satisfy mass consistency. Indeed, wind distributions shown in Figures 22 and 23 are in close agreement with each other, although LINCOM (Figure 23) produced slightly more spatial variations than WOCSS (Figure 22).

As mentioned earlier, a diagnostic wind model is no more than a scheme for interpolation of observed winds at specified grid points. For this reason, the spatial variations of wind

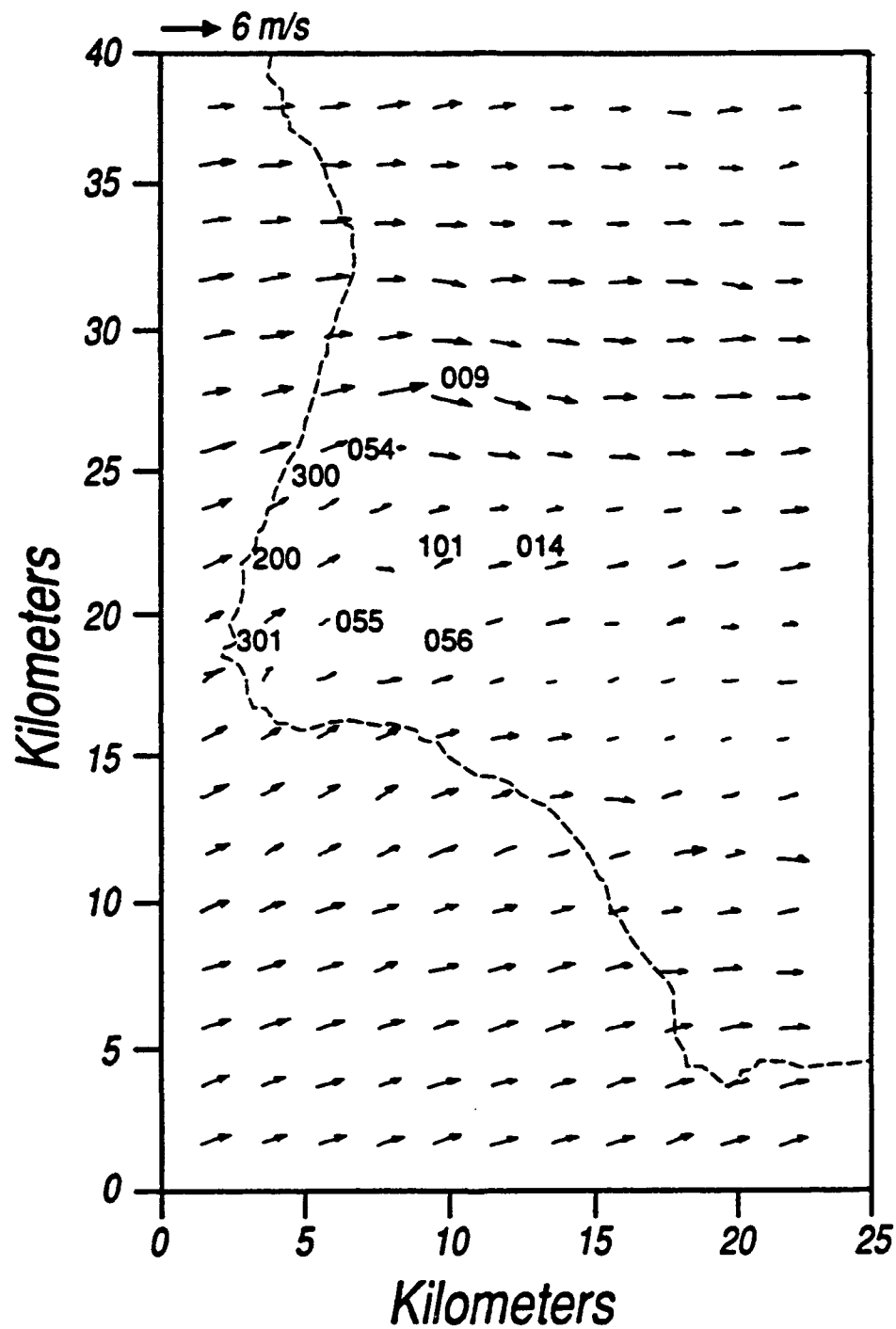


Figure 22. Modeled Horizontal Wind Vectors for the MI87 Case at 4 meters above Ground Level by Using WOCSS Diagnostic Wind Model. Meteorological measurement stations are identified by numbers.

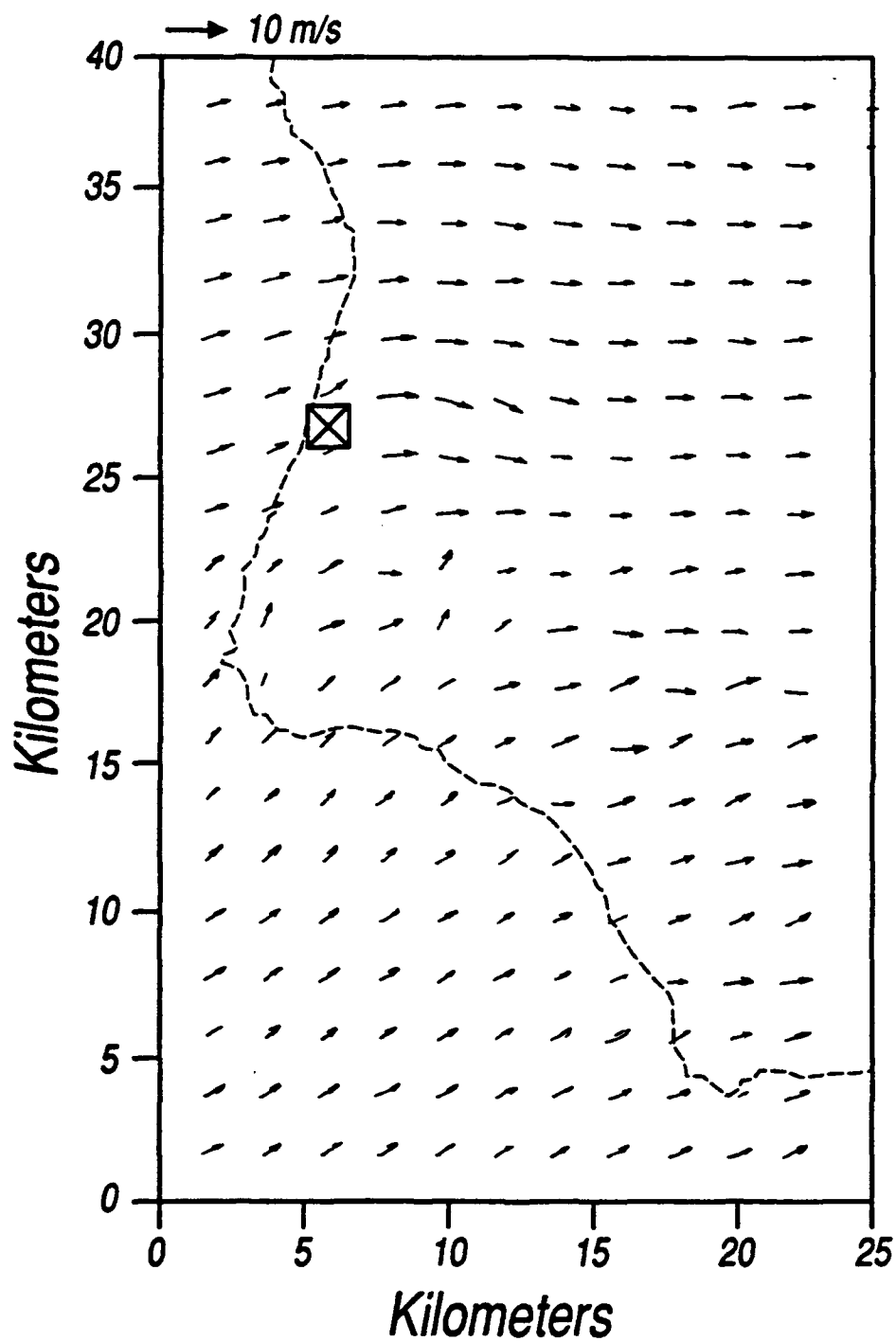


Figure 23. Modeled Horizontal Wind Vectors for the MI87 Cast at 10 meters above Ground Level by Using LINCOM Diagnostic Wind Model.



vectors in Figures 22 and 23 are confined mainly to the regions where data are available. Mass consistency and other physical constraints used in diagnostic wind models can affect the wind vectors away from the measurement sites.

A prognostic wind model, on the other hand, is based on a set of physical equations and does not require the measurement of surface winds for forecast. Observations are used to verify the predictions.

The prognostic model results (Figure 5) generally agree with the diagnostic model results (Figures 22 and 23) in the area where wind measurements are available. Wind vectors in the prognostic model are determined from the balance among the pressure force, turbulent mixing, and Coriolis force. Therefore, prognostic models can provide wind distributions in regions where no measurements are available. Our wind vectors (Figure 10) in the outer grid are quite different from the wind fields computed by WOCSS (Figure 22) and LINCOM (Figure 23) in the areas where topographic features are prominent. The diagnostic models do not incorporate the pressure forces generated by the sloped surfaces. Therefore, the variations of wind distributions based on a diagnostic wind model must come from the wind data that reflect the surface inhomogeneity.

Figures 24 and 25 are the wind vectors for the MI90 case modeled by WOCSS and LINCOM, respectively. The wind directions are uniform (northwesterly) except in the areas where tower wind data were available.

Wind vectors simulated by HOTMAC (Figure 11) show very little variations in space because the strong (13.5 m/s) prevailing wind overpowered the perturbations generated by differential cooling over the sloped surface. Figure 11 is quite different from Figure 5, in which the prevailing wind was small (2 m/s) and the modeled surface wind vectors were perturbed significantly by differential heating over the sloped surfaces. The comparison between

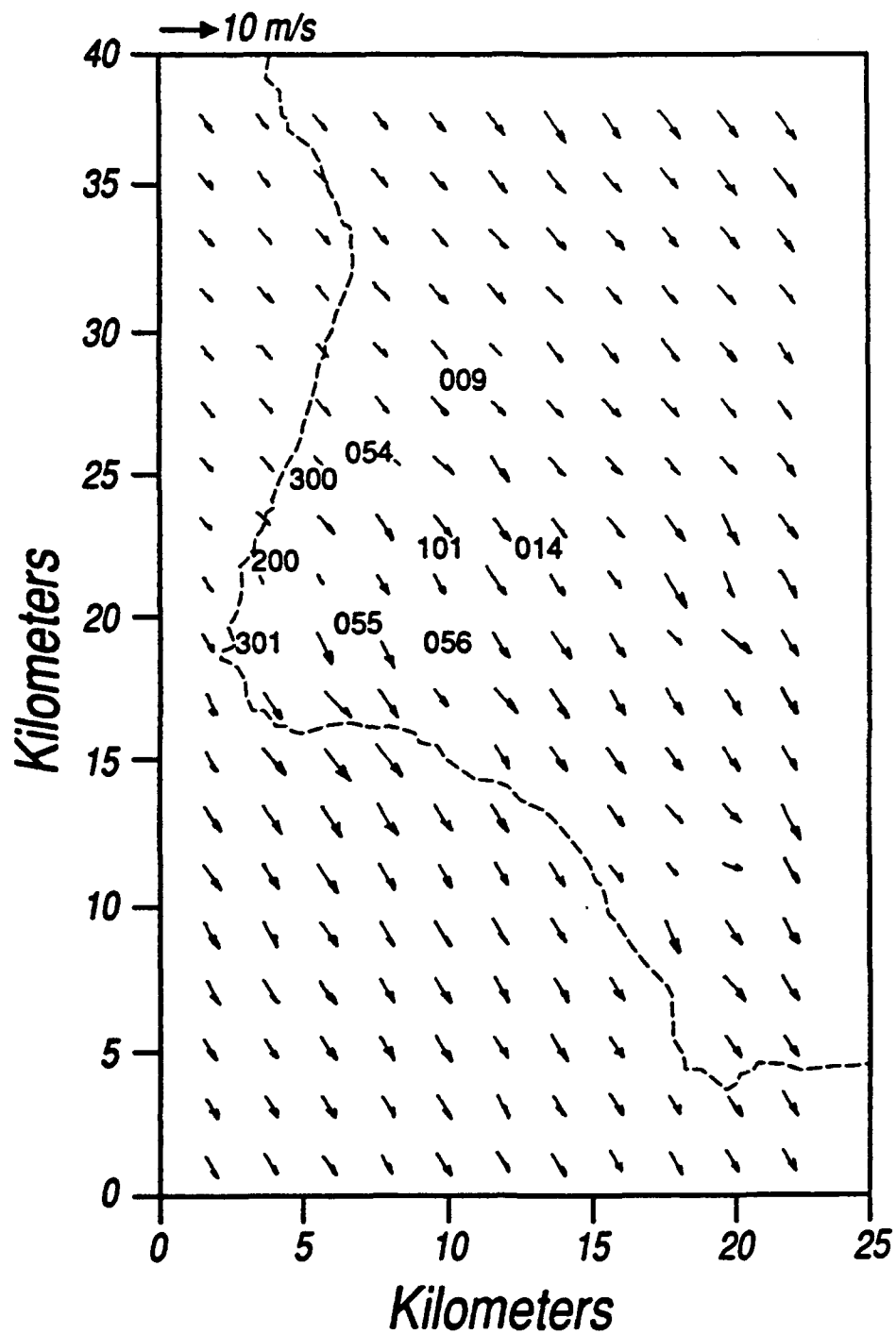


Figure 24. Same as in Figure 22 except for the MI90 Case.

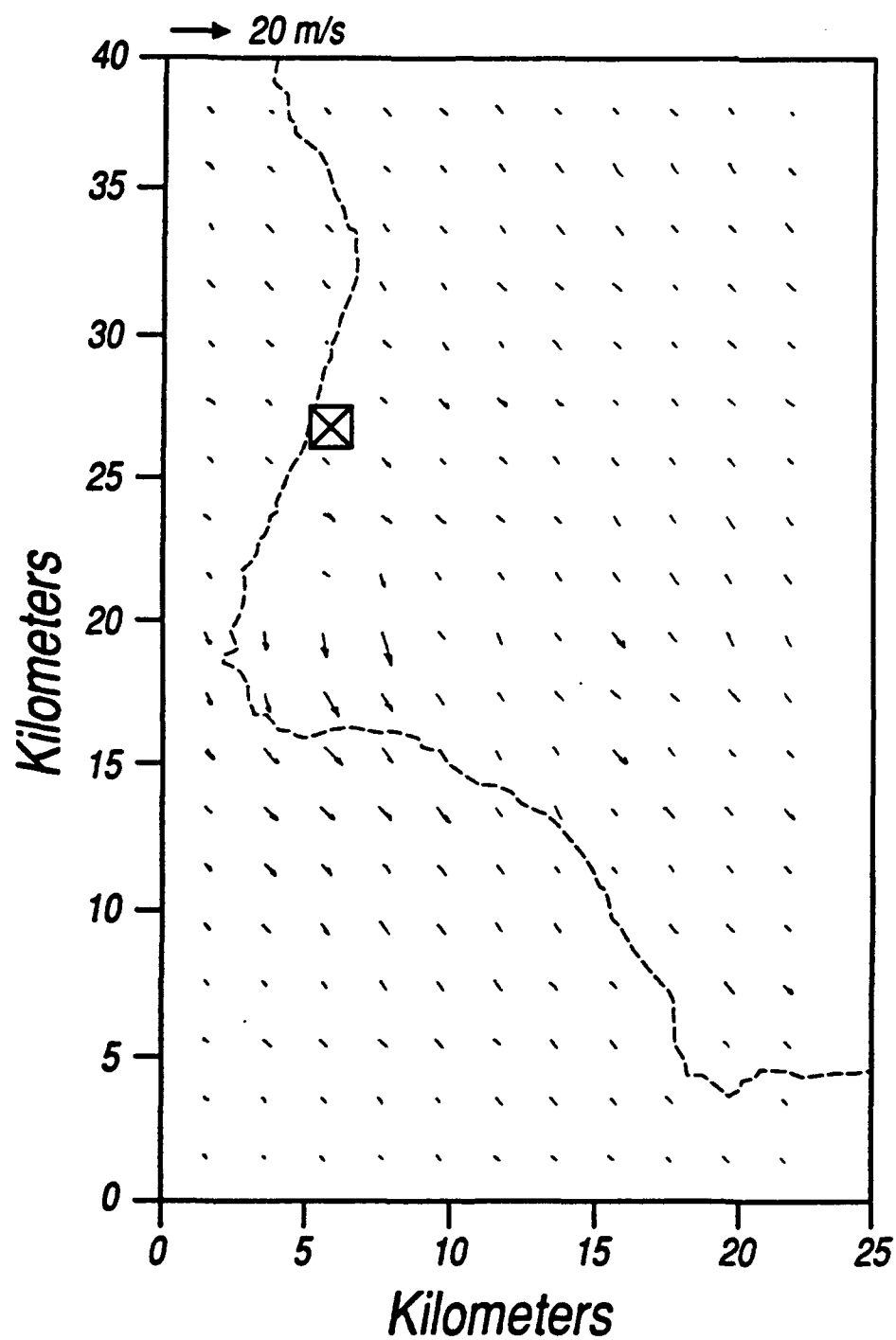


Figure 25. Same as in Figure 23 except for the MI90 Case.

Figures 5 and 11 demonstrate the HOTMAC's capabilities in realistically incorporating the effects of large-scale pressure force and local-scale pressure force due to differential heating.

## B. DIFFUSION MODEL

Thykier—Nielsen et al. (Reference 13) applied a diffusion model (RIMPUFF) to simulate the fluorescent particle concentration distributions at the ground for the MI87 and MI90 cases. RIMPUFF is a Lagrangian puff model that simulates time-variable continuous releases by sequentially releasing a series of Gaussian-shaped puffs. Mean wind fields were provided by LINCOM and turbulence velocities were based on the local energy of the fluctuating horizontal wind components. The turbulent energies were estimated from the climatological study of flow and turbulence at VAFB carried out in connection with handbook-study (Reference 13). The turbulence velocity was added to the mean value to determine a puff velocity at the center of mass. The procedure is similar to that used in RAPTAD except that turbulence velocities in RAPTAD are provided by HOTMAC.

Figures 26 and 27 show the concentration distributions of fluorescent particles at ground level as modeled by RIMPUFF for the MI87 and MI90 cases, respectively. Thykier—Nielsen et al. (Reference 13) do not explain the values for the concentration contours, nor do they present a comparison of the modeled and observed concentration values. However, Thykier—Nielsen et al. did comment on their results, saying, "For all of the eight tracer experiments studied, our simulated mean-plume spread resembles well in form and shape the corresponding measured tracer concentrations, at least for the relatively short range where concentration measurements were detectable during the Mountain Iron tracer experiments."

Finally, we compare the performance of HOTMAC and RAPTAD with that of the MI model currently used at VAFB. The MI model is an empirical equation that relates a surface concentration value to distance, standard deviation of horizontal wind fluctuation, mean

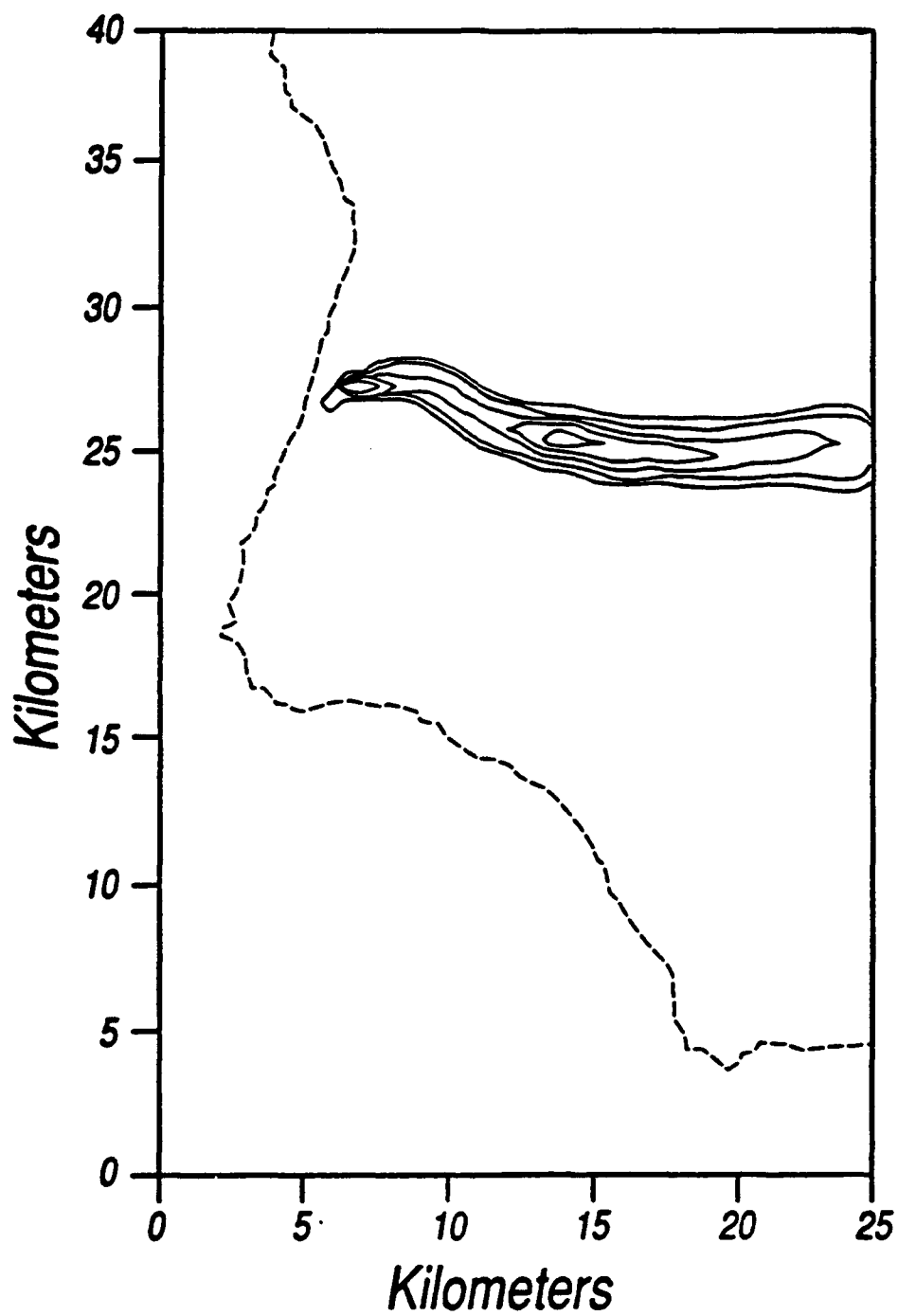


Figure 26. Exposure Distribution of Fluorescent Particles at Ground Level Modeled by RIMPUFF for the MI87 Case. Contour values are undefined.

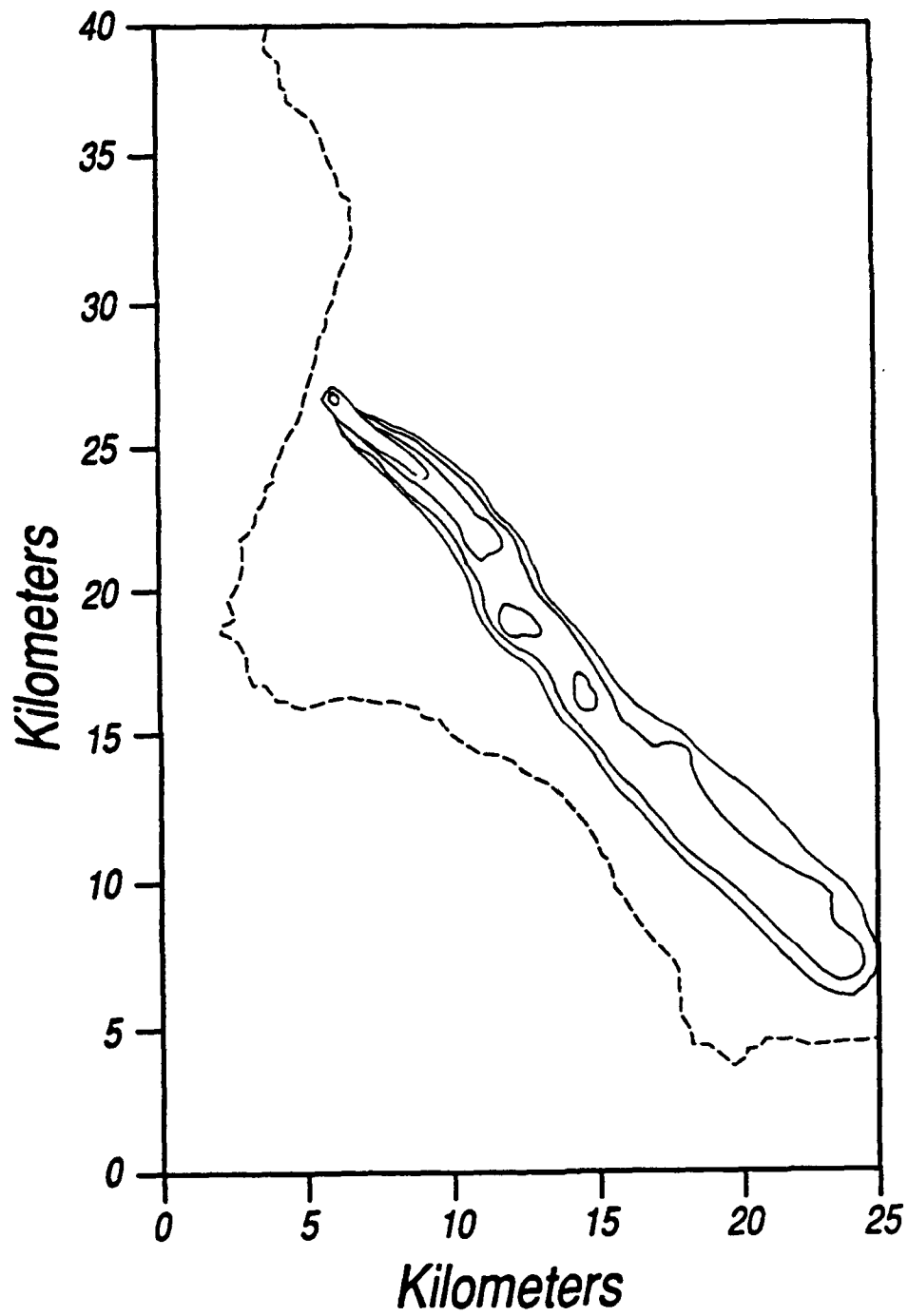


Figure 27. Same as in Figure 26 except for the MI90 Case.

velocity, and temperature gradient in the surface layer. Empirical coefficients were determined to fit best the MI diffusion data.

A simple distance-dependent formula resulted in good fit to the observations, with 63 percent within a factor of 2 of the mean and 92 percent within a factor of 4. We applied the same formula at the sampling sites for MI87, MI90, and MI91 cases and obtained exposure values. The results are compared with observations in Figure 28, where HOTMAC/RAPTAD predictions are also plotted. The predicted values are within a factor of 2 of the observations between the inner two dashed lines and within a factor of 4 between the outer two dashed lines. Two data points outside of the factor of 4 boundary resulted from the unreasonably large observed exposure value reported for the MI87 case.

Figure 28 indicates that HOTMAC and RAPTAD predictions are at least as good as those made by the MI model which was specifically tuned with the MI diffusion data.

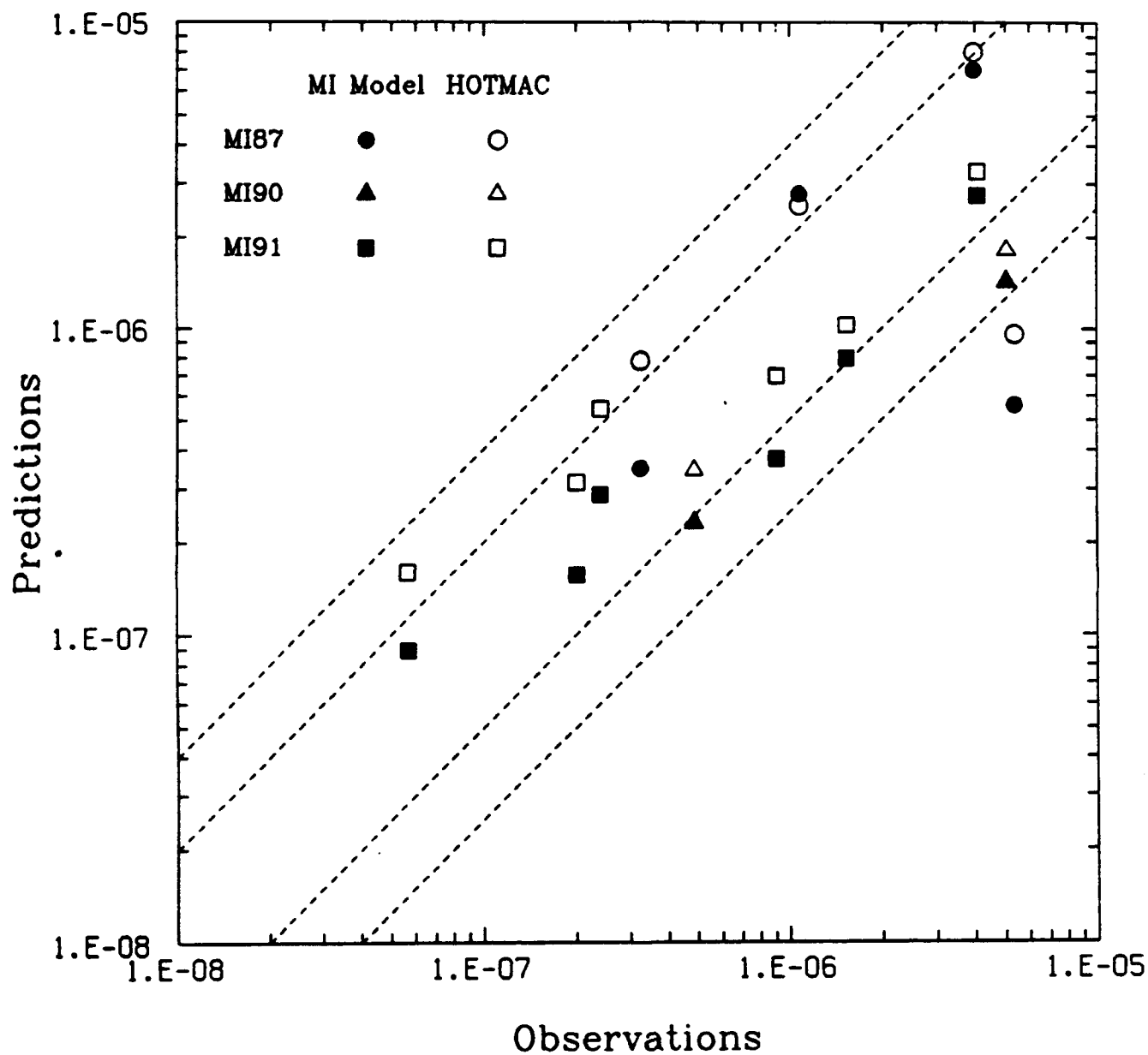


Figure 28. Scatter Diagram of the Predicted and Observed Fluorescent Particle Concentration (nondimensional) at Ground Level. The inner dashed lines indicate a factor of 2 and the outer dashed lines indicate a factor of 4.



## SECTION VI

### APPLICATIONS ON DESKTOP COMPUTERS

Recent advances in desktop computer capabilities, particularly those of an engineering workstation, are astonishing. A high-performance workstation has reportedly exceeded a supercomputer in certain scalar operations. The affordability and portability of the desktop computer have opened the door to many applications that were previously considered impossible.

One logical area for such applications is in upgrading the toxic hazard modeling capabilities for emergency response management. Scientists at Los Alamos National Laboratory are in the process of developing three-dimensional forecasting models that run on a desktop computer.

In this section we will discuss our experience in running HOTMAC and RAPTAD on a Sun Microsystems workstation and a MicroVax computer.

#### A. SUN 4/110 WORKSTATION

The HOTMAC code for a desktop computer is slightly different from that for a supercomputer. First, a single grid is used. The number of cells is generally smaller. This requires either a coarser terrain resolution or a smaller domain, depending on the simulation. Finally, the vertical profile of the initial potential temperature may be represented by two segments, whereas three are used in the supercomputer version.

We ran HOTMAC and RAPTAD for the MI87 case on a Sun 4/110 workstation. The computational domain matches the outer grid used in Section IV, i.e.,  $40 \times 48 \text{ km}^2$ . The horizontal grid spacing was 2 km as opposed to 1 km in the Cray version. Potential temperature lapse rates of  $0.04^\circ\text{C/m}$  from the sea surface to 460 meters above msl and  $0.0044^\circ\text{C/m}$  above 460 meters above msl were used. In the Cray version an additional lapse rate of  $0.0142^\circ\text{C/m}$  was used from 460 to 960 meters above msl. Other meteorological conditions were identical.

Figure 29 shows the modeled horizontal wind vectors 14 meters above the ground at 0700, 1400, and 2300 lst June 14, 1966. Although the upper air wind direction was 225 degrees (southwesterly), downslope flows and land breeze developed in the surface layer due to cooling at the ground. Sunrise on June 14, was shortly before 0500 lst.

As the sun warms the ground, the air temperature in the surface layer quickly increases as a result of turbulent mixing. The air temperature over a sloping surface becomes higher than the temperature at the same elevation but away from the ground. The temperature difference results in a horizontal pressure gradient: a low pressure is normally located at high elevation. This pressure force produces upslope flows and sea breezes that converge over ridges as seen in the horizontal wind vector distribution at 1400 lst.

The ground starts cooling shortly before sunset (around 2000 lst) and the air temperature close to the ground over a sloped surface falls below the air temperature at the same elevation but away from the surface. Thus, the direction of the pressure gradient at night is opposite to its daytime counterpart. However, the magnitude of the pressure gradient force at night is normally much smaller than in the daytime, particularly in summer, for the following reasons.

First, turbulence intensity in the surface layer during the nocturnal period is extremely small compared with the daytime value. Therefore, only the air relatively close to the ground is cooled by turbulent mixing. The depth of the nocturnal stable boundary layer is on the order of 100 meters, much smaller than that of the daytime convective boundary layer, which is at least several hundred meters high.

Second, the solar energy that reaches the ground in summer is far larger than the net longwave radiation loss during the night. In other words, much more heat energy is supplied to the atmosphere during the day than is extracted from it during the night.

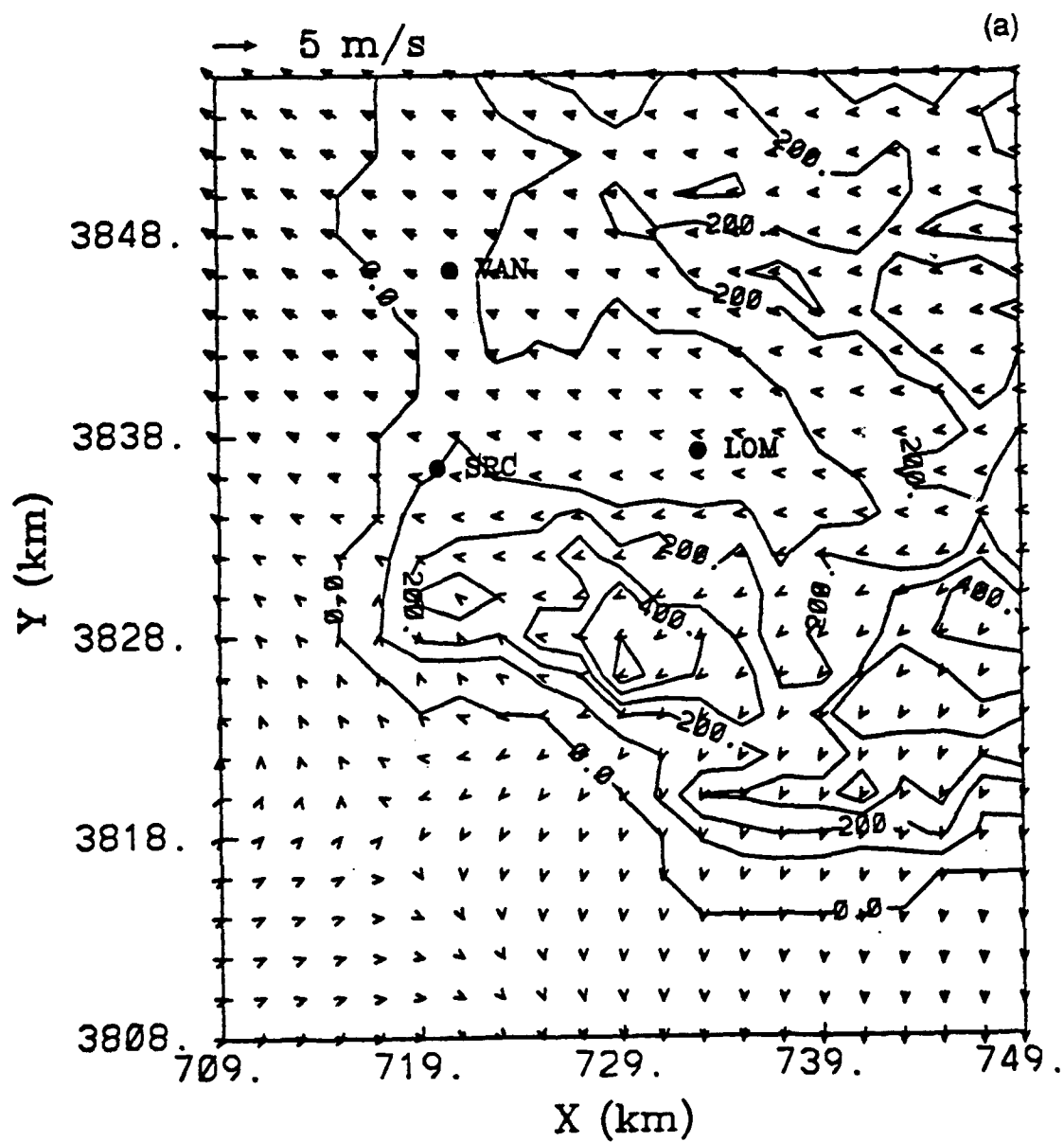


Figure 29. Modeled Horizontal Wind Vectors at 14 meters above the Ground at (a) 0700 lst, (b) 1400 lst, and (c) 2300 lst, June 14, 1966.

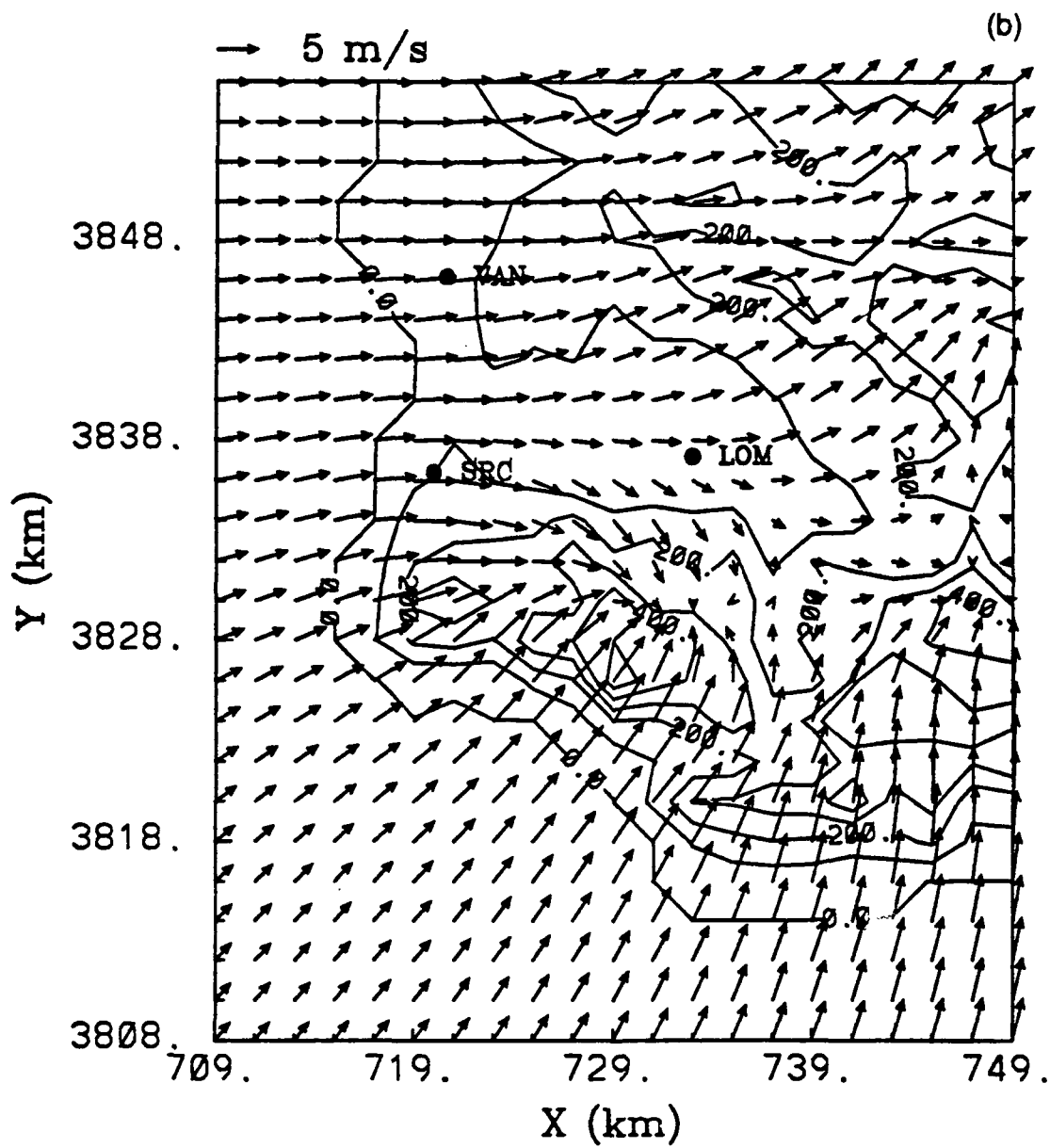


Figure 29. Modeled Horizontal Wind Vectors at 14 meters above the Ground at (a) 0700 lst, (b) 1400 lst, and (c) 2300 lst, June 14, 1966.

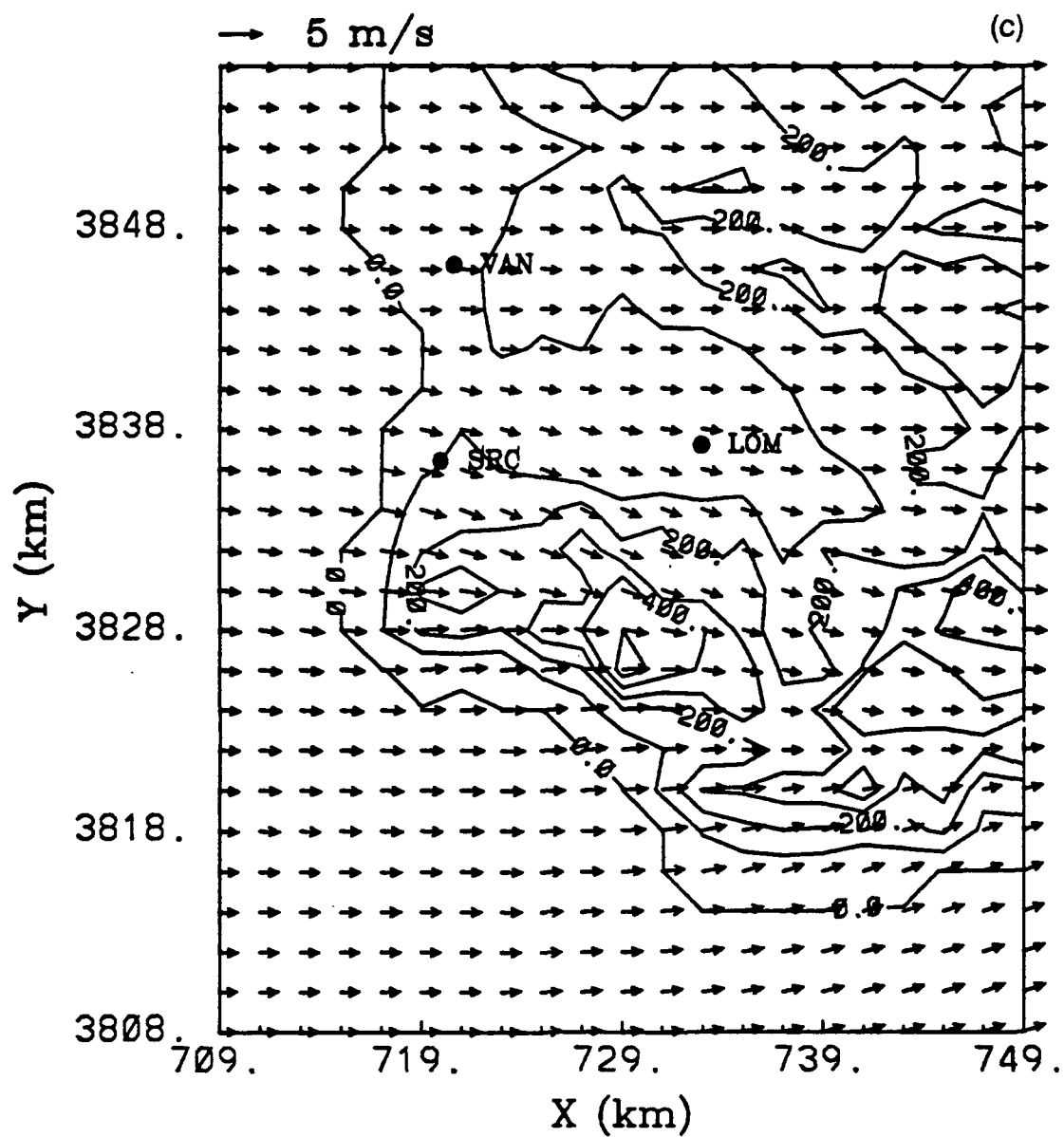


Figure 29. Modeled Horizontal Wind Vectors at 14 meters above the Ground at (a) 0700 lst, (b) 1400 lst, and (c) 2300 lst, June 14, 1966.

The combination of the deeper boundary layer and greater energy available to heat the atmosphere during the day produces much larger pressure gradients than are produced at night. For this reason, the modeled wind directions at 2300 lst (Figure 29) were not downslope, although the upslope flow components encountered at 1400 lst almost completely disappeared. The modeled wind direction later became downslope, but its magnitude was very small.

To illustrate diurnal variations of plume structure, puffs were released continuously for 29 hours starting at 2300 lst, June 13, 1966. Figure 30 shows the projection of puff centers on the ground at 0300, 0700, 1200, 1500, and 2200 lst, June 14, 1966. The upper-air wind direction was southwesterly (MI87) for the entire simulation period, but puffs remained close to the ground at 0300 lst and were transported to the southeast. The northwesterly flows were initiated during the day when sea-breeze circulations and upslope flows combined.

Nocturnal drainage flows and land breezes continued to develop until 0700 lst and puffs were transported offshore. As the ground temperatures increased as the result of solar heating, sea breezes and upslope flows developed. Pollutants offshore were pushed back toward the land by 1200 lst (Figure 30).

Pollutants were initially transported to the east, then toward the south by the surface winds. Horizontal wind vectors in the surface layer converged into high-altitude locations, where upward motion developed. Pollutants moved upward with vertical velocity and vertical mixing due to atmospheric turbulence. The pollutants that were lifted above the surface boundary layer encountered southwesterly prevailing winds and moved toward the northeast as seen from the plot for 1500 lst.

As the sun set, ground temperature continued to decrease and turbulence subsided. Pollutants remained close to the ground and moved toward the east-southeast at 2300 lst (Figure 30).

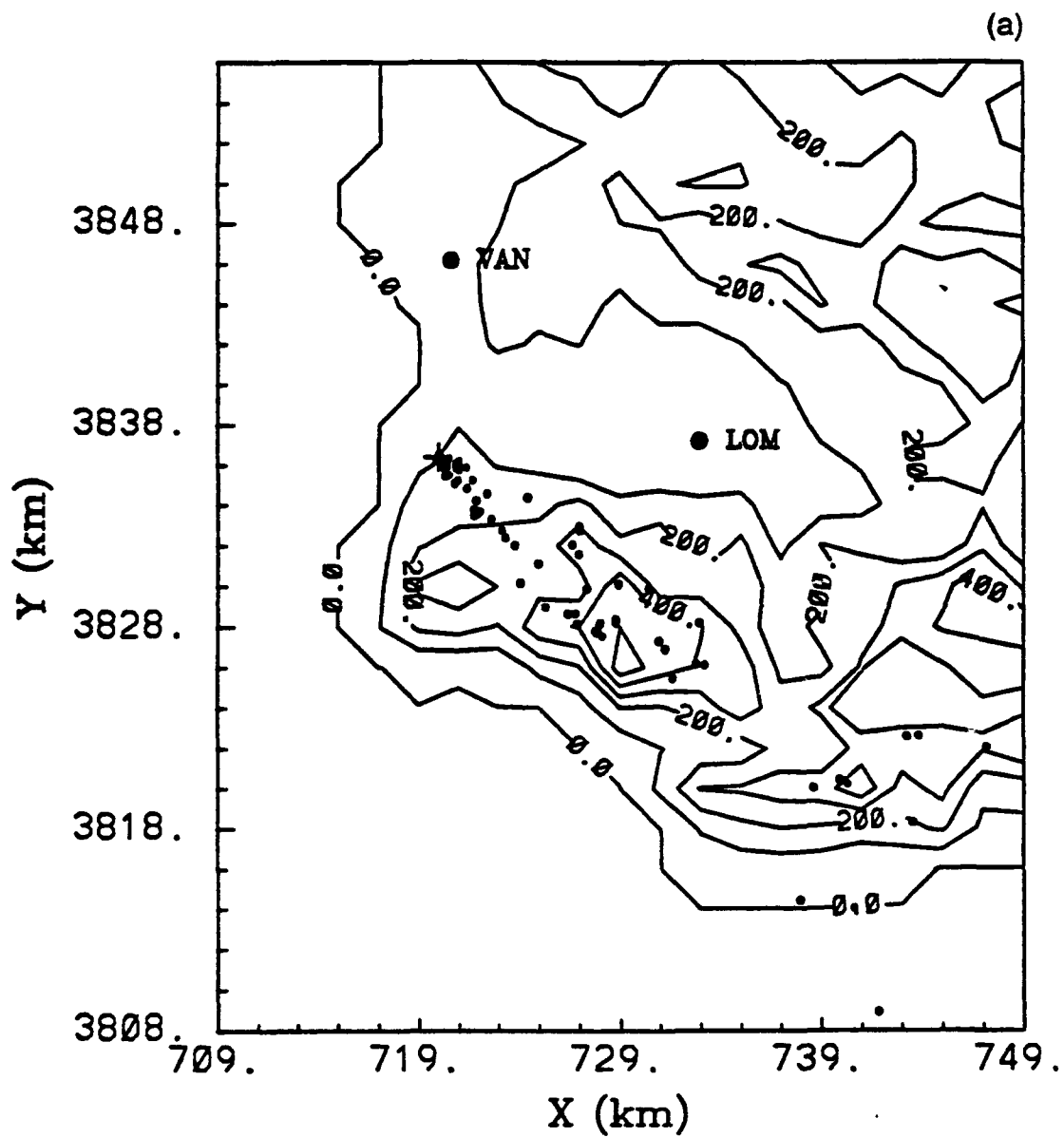


Figure 30. Modeled Trajectories of Puff Centers Projected on the Surface at (a) 0300 lst, (b) 0700 lst, (c) 1200 lst, (d) 1500 lst, and (e) 2300 lst, June 14, 1966. Puffs were released continuously starting at 2300 lst, June 13, 1966.

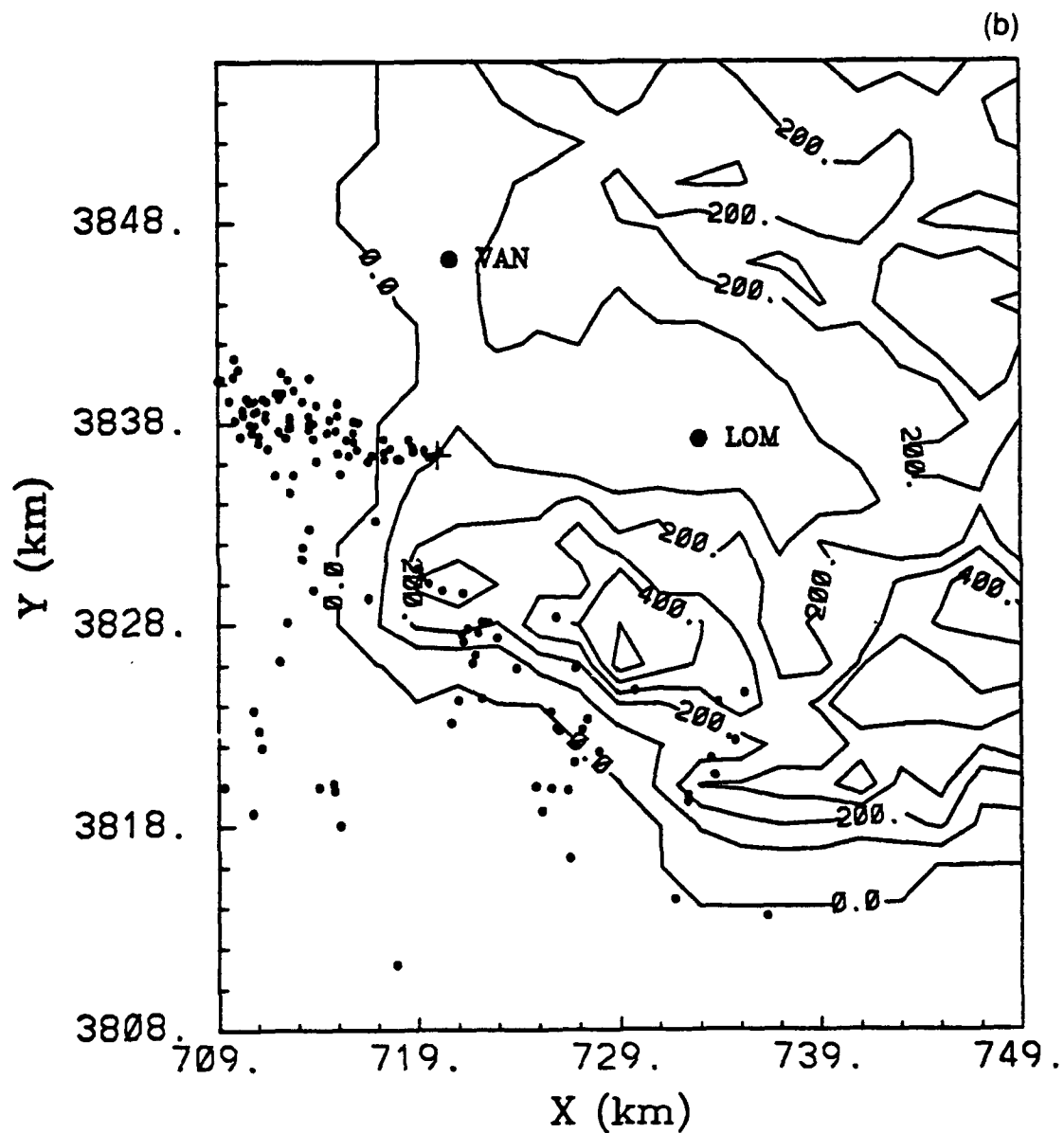


Figure 30. Modeled Trajectories of Puff Centers Projected on the Surface at (a) 0300 lst, (b) 0700 lst, (c) 1200 lst, (d) 1500 lst, and (e) 2300 lst, June 14, 1966. Puffs were released continuously starting at 2300 lst, June 13, 1966.



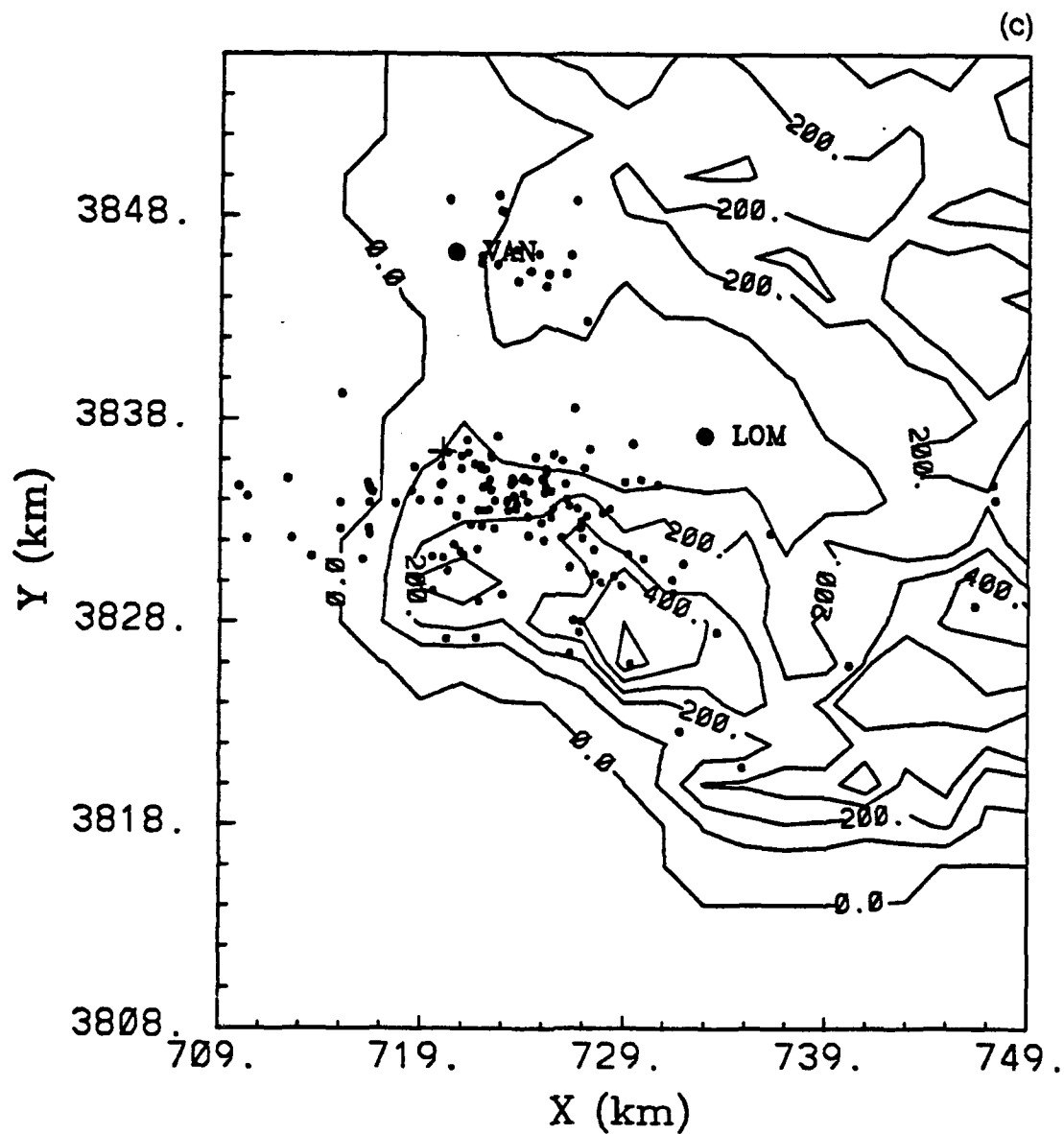


Figure 30. Modeled Trajectories of Puff Centers Projected on the Surface at (a) 0300 lst, (b) 0700 lst, (c) 1200 lst, (d) 1500 lst, and (e) 2300 lst, June 14, 1966. Puffs were released continuously starting at 2300 lst, June 13, 1966.

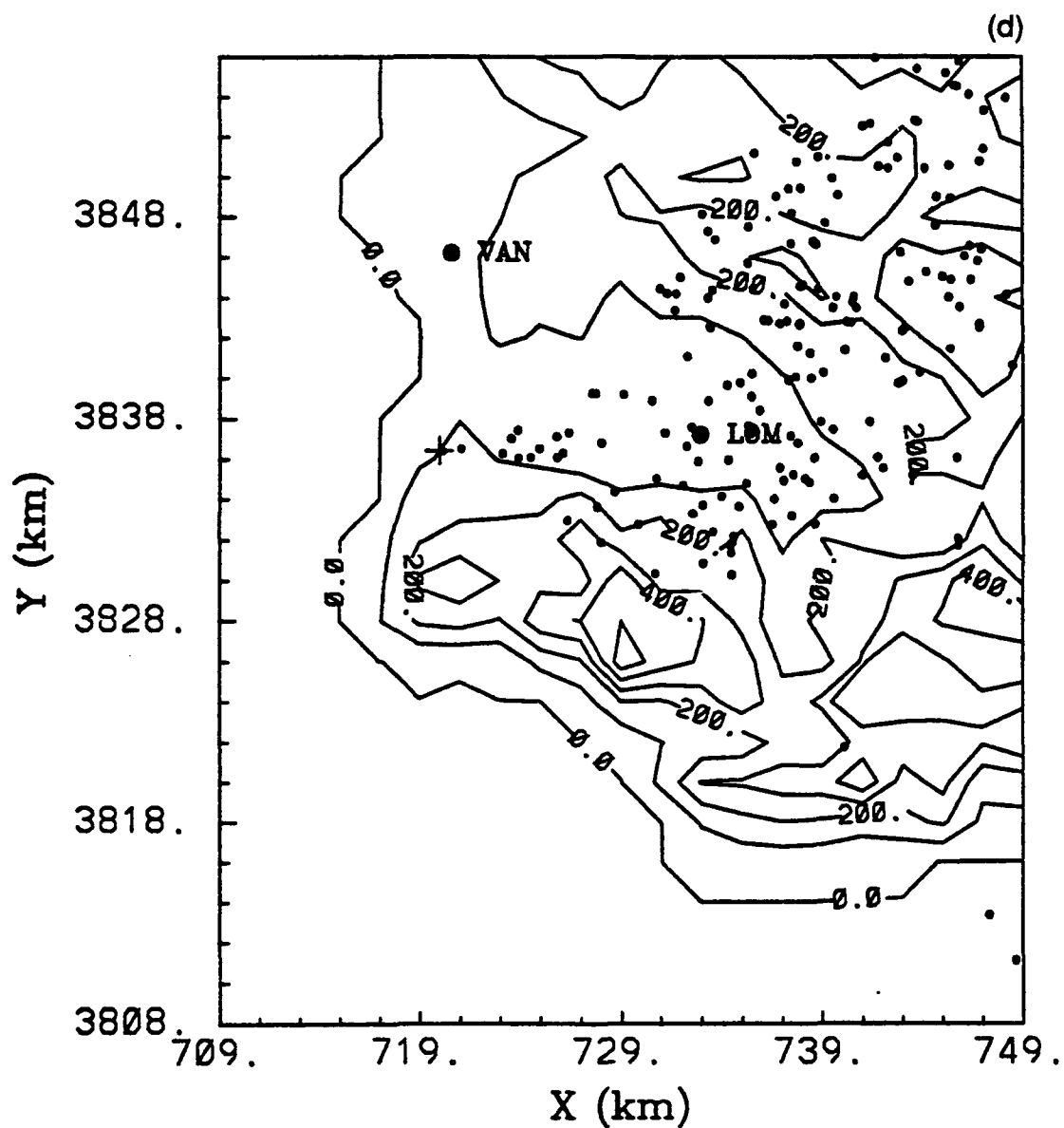


Figure 30. Modeled Trajectories of Puff Centers Projected on the Surface at (a) 0300 lst, (b) 0700 lst, (c) 1200 lst, (d) 1500 lst, and (e) 2300 lst, June 14, 1966. Puffs were released continuously starting at 2300 lst, June 13, 1966.

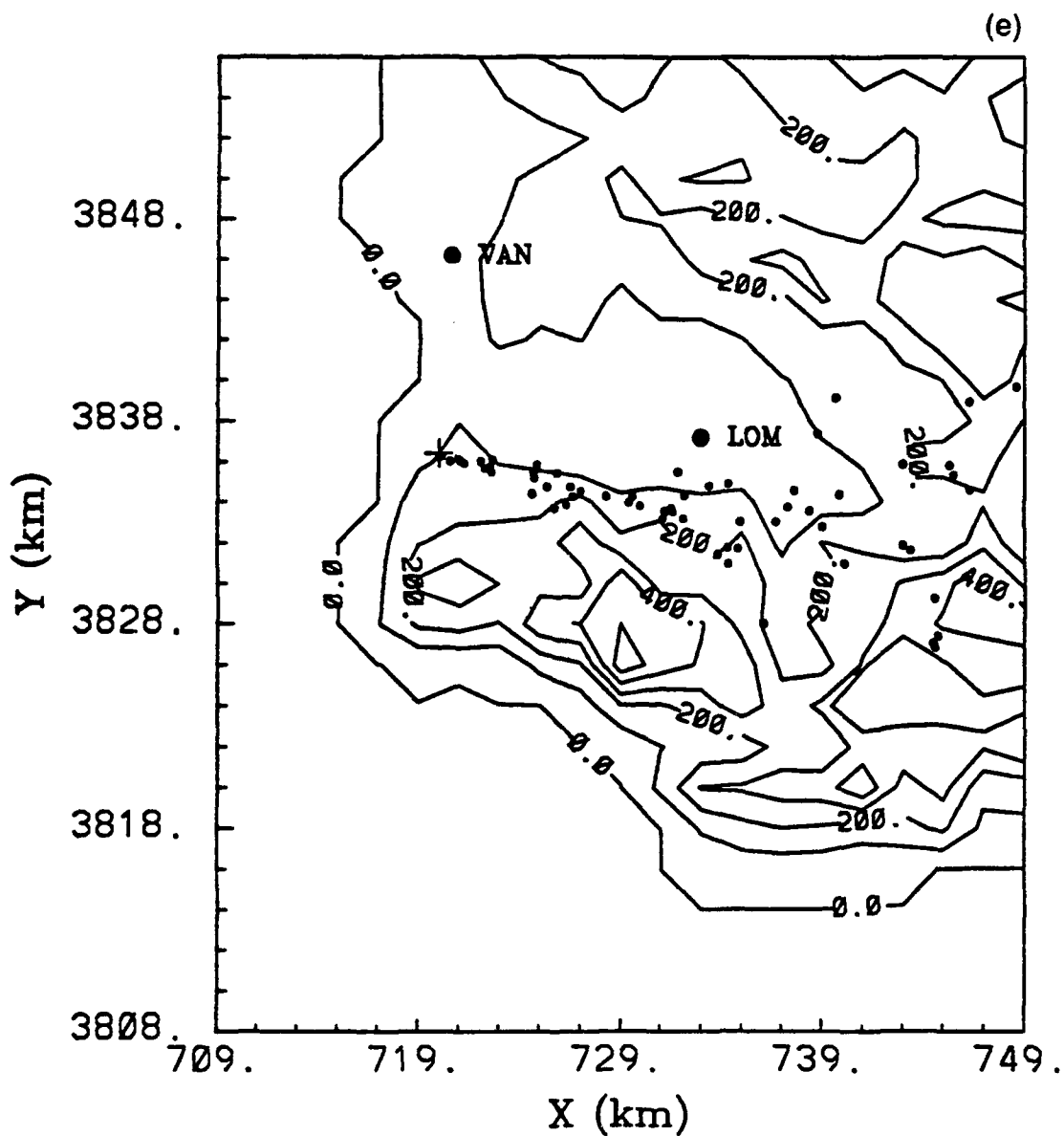


Figure 30. Modeled Trajectories of Puff Centers Projected on the Surface at (a) 0300 lst, (b) 0700 lst, (c) 1200 lst, (d) 1500 lst, and (e) 2300 lst, June 14, 1966. Puffs were released continuously starting at 2300 lst, June 13, 1966.

As seen in Figure 30, surface wind directions at the source location varied 360 degrees in 24 hours. Accordingly, pollutants released continuously went all around around the source.

Figure 31 shows the ground level concentration at 0300, 0700, 1200, 1500, and 2200 lst, respectively. The distribution of the surface concentrations at 0300 and 0700 lst is complicated, with many highs and lows. These distributions are definitely not Gaussian.

Strong vertical mixing due to turbulence at 1200 and 1500 lst resulted in surface concentration distributions similar to a Gaussian plume. Concentration values decreased monotonically with the distance from the source. Local hot spots diminished and maximum values were much smaller than the nighttime counterparts.

#### B. MICROVAX 2000

The computations performed by a Sun 4/110 workstation were repeated by a MicroVax 2000 computer. The computational domain was  $40 \times 48 \text{ km}^2$  with a horizontal grid spacing of 2 km. Initial and boundary conditions were identical to those specified for the Sun computations. The HOTMAC simulation started at 0500 lst, June 13, 1966 and continued for 24 hours. In the RAPTAD simulation, puffs were released continuously for 20 hours starting at 0600 lst, June 13, 1966.

We compared selected HOTMAC outputs from the Sun 4/110 and MicroVax 2000 simulations. They were in good agreement with each other. The differences were, in general, less than 0.1 percent. We consider the differences insignificant.

RAPTAD uses the variables computed by HOTMAC to calculate puff transport and diffusion. Because a random-number generator is involved in RAPTAD, instantaneous concentration values obtained by a MicroVax computer are different from those obtained by a Sun workstation even when HOTMAC outputs are identical. The method of generating a random number varies from one computer architecture to another.

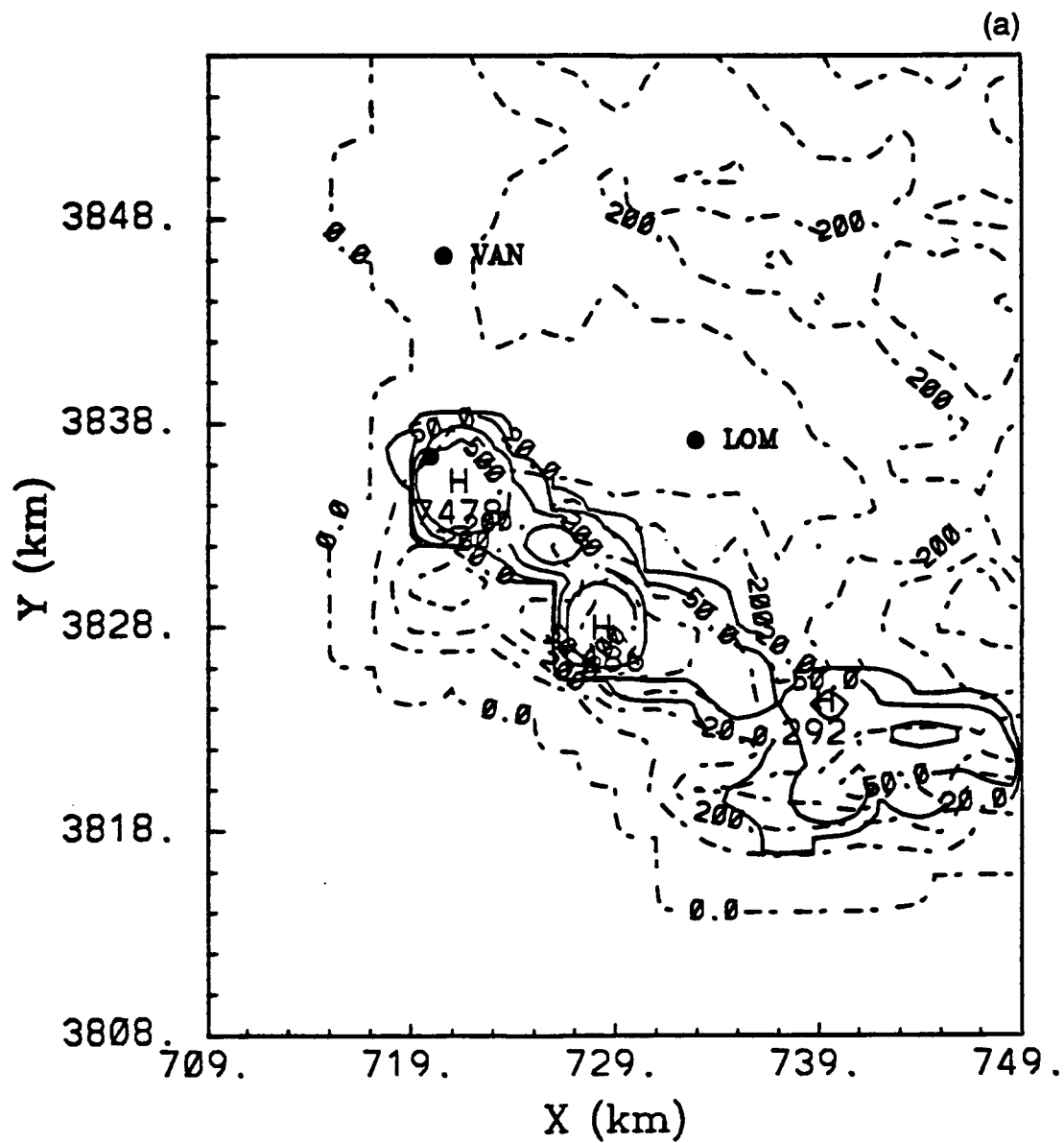


Figure 31. Concentration Distribution (in arbitrary units) of Fluorescent Particles at Ground Level at (a) 0300 lst, (b) 0700 lst, (c) 1200 lst, (d) 1500 lst, and (e) 2200 lst, June 14, 1966.

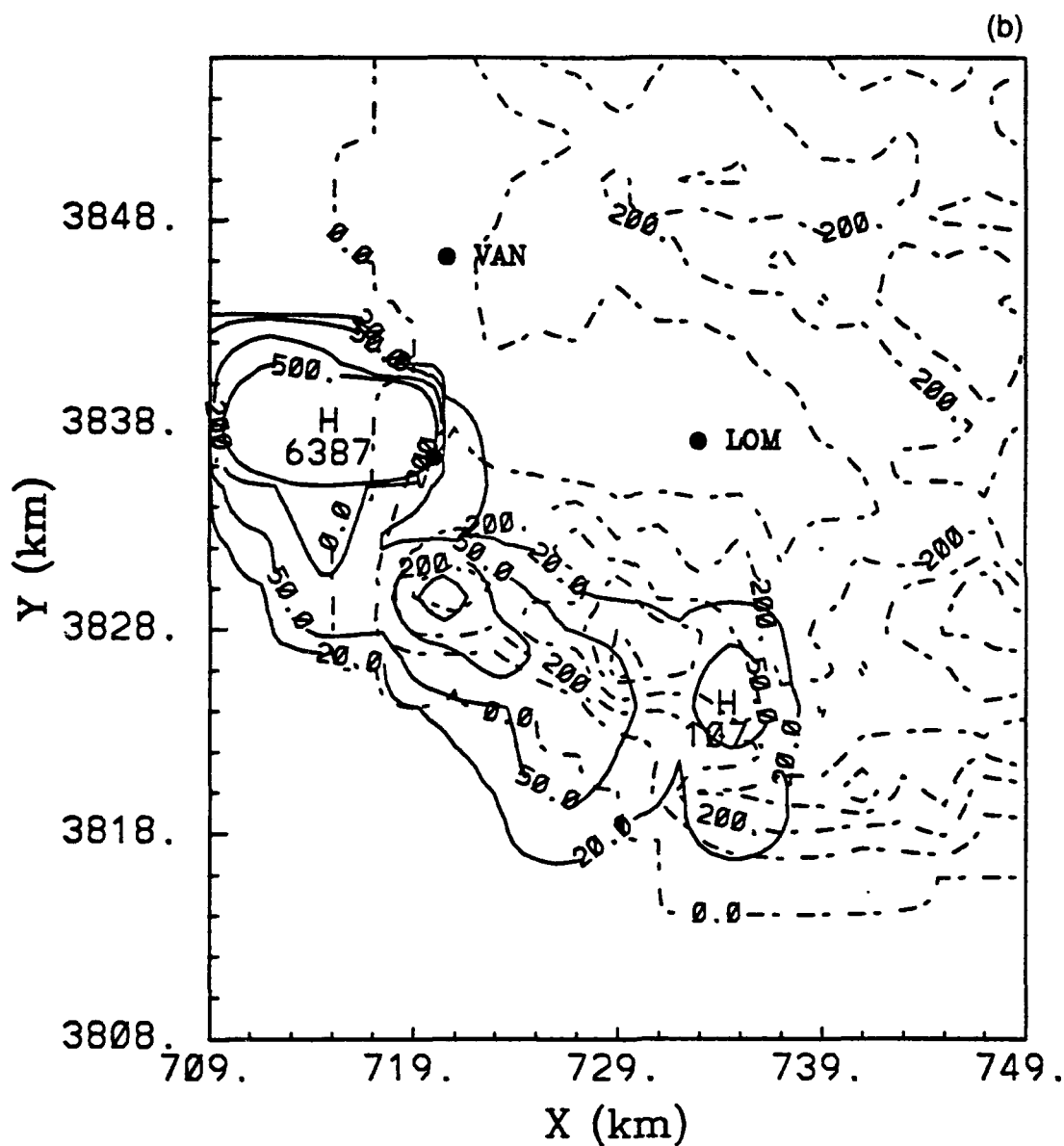


Figure 31. Concentration Distribution (in arbitrary units) of Fluorescent Particles at Ground Level at (a) 0300 lst, (b) 0700 lst, (c) 1200 lst, (d) 1500 lst, and (e) 2200 lst, June 14, 1966.

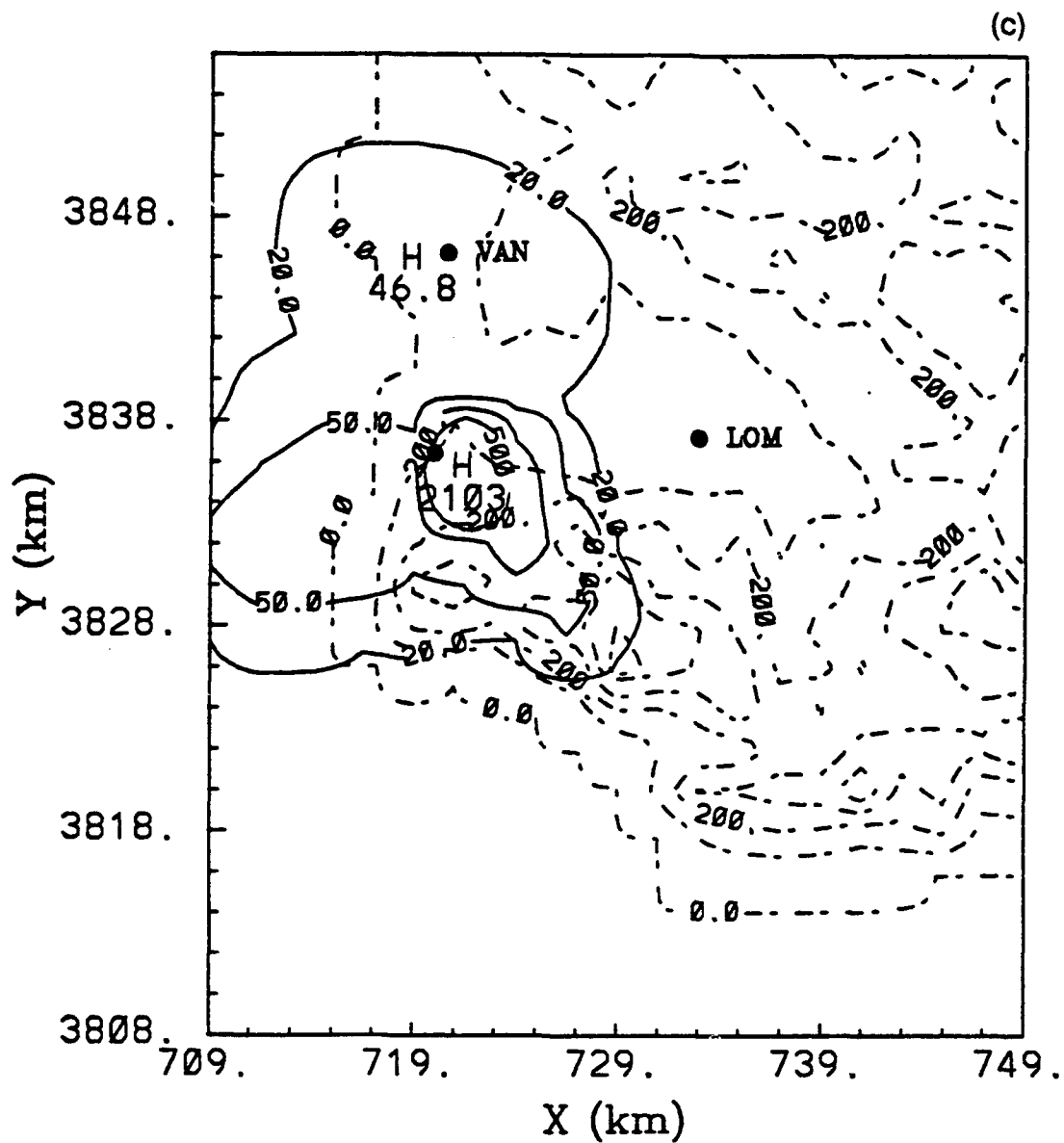


Figure 31. Concentration Distribution (in arbitrary units) of Fluorescent Particles at Ground Level at (a) 0300 lst, (b) 0700 lst, (c) 1200 lst, (d) 1500 lst, and (e) 2200 lst, June 14, 1966.

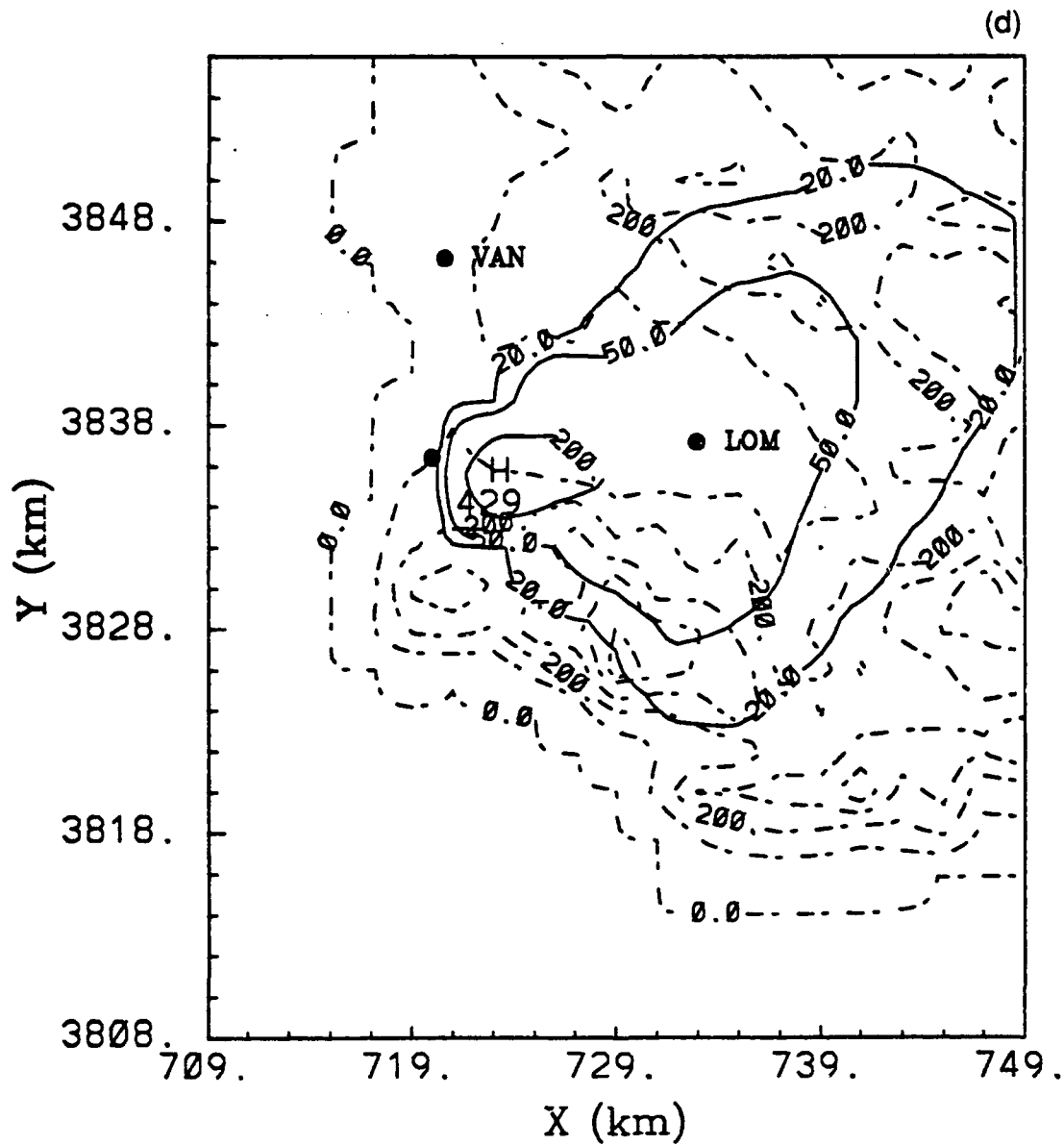


Figure 31. Concentration Distribution (in arbitrary units) of Fluorescent Particles at Ground Level at (a) 0300 lst, (b) 0700 lst, (c) 1200 lst, (d) 1500 lst, and (e) 2200 lst, June 14, 1966.



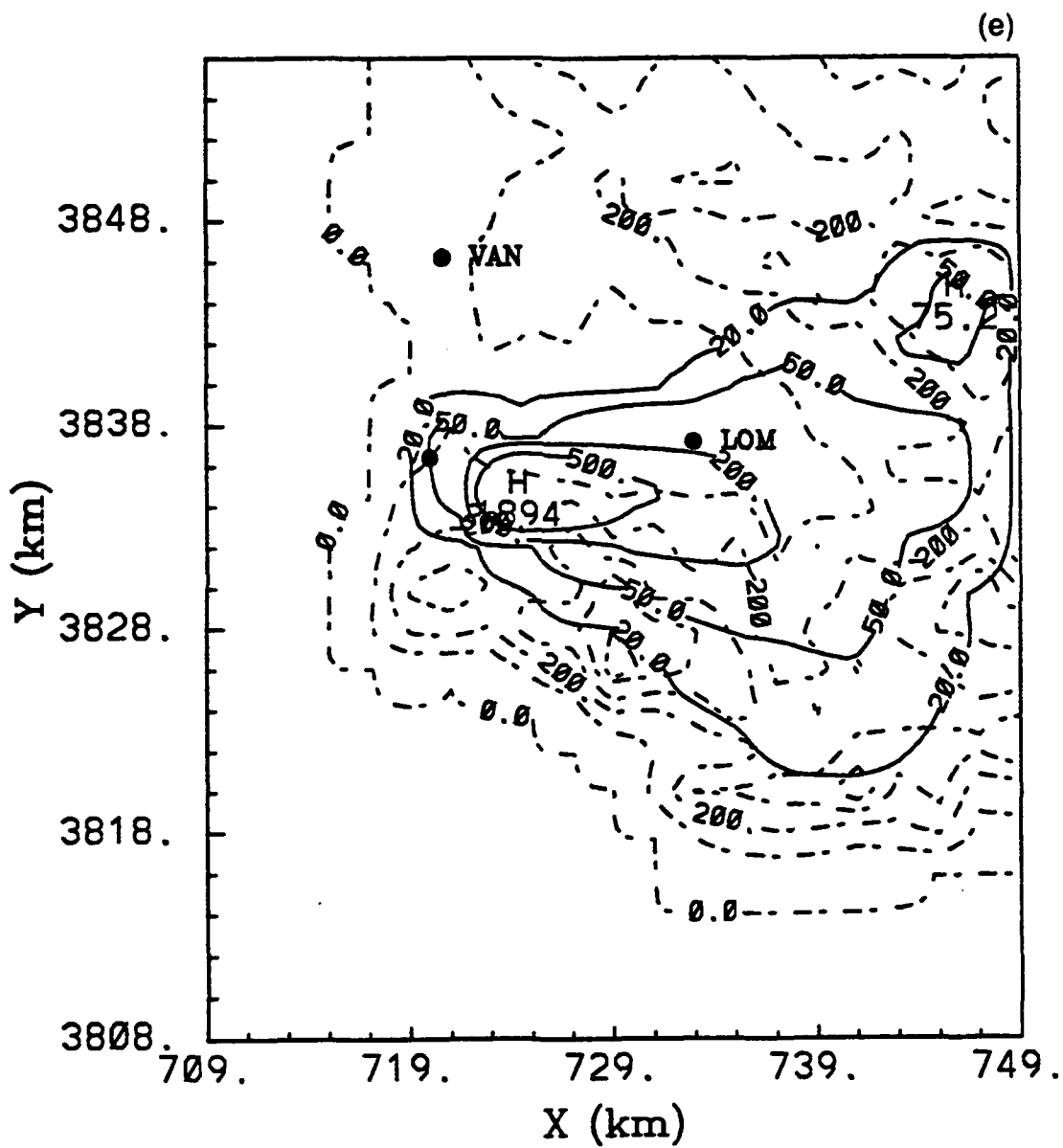


Figure 31. Concentration Distribution (in arbitrary units) of Fluorescent Particles at Ground Level at (a) 0300 lst, (b) 0700 lst, (c) 1200 lst, (d) 1500 lst, and (e) 2200 lst, June 14, 1966.

Figure 32 shows the MicroVax model results of puff centers projected on the ground at 1100 lst, June 13, 1966. The modeled instantaneous concentration distributions (in arbitrary units) at the ground level are shown in Figure 33.

The corresponding model results obtained by a Sun 4/110 workstation are shown in Figure 34 and Figure 35. The puff-center projections (Figure 32) and ground-level concentrations (Figure 33) obtained by a MicroVax computer are in close agreement with but not identical to the counterparts (Figure 34 and Figure 35) obtained by a Sun 4/110 workstation because the two computers generate random numbers differently.

On the basis of the results discussed above, we conclude that HOTMAC and RAPTAD were run successfully on a MicroVax 2000 and that their results are in good agreement with those obtained by a Sun 4/110 workstation.

Finally, we record in Table 3 the CPU time used for the computations. These values serve merely as a reference, as current workstation technology is significantly better than the computers used in this study.

TABLE 3. CPU COMPARISON BETWEEN SUN 4/110 AND MICROVAX 2000.

Calculation	Sun 4/110	MicroVax 2000
<b>HOTMAC</b>		
21 x 25 x 16 grid points	4 h, 11 min	22 h, 10 min
28-h simulation		
<b>RAPTAD</b>		
20-h simulation	26 min	3 h, 45 min

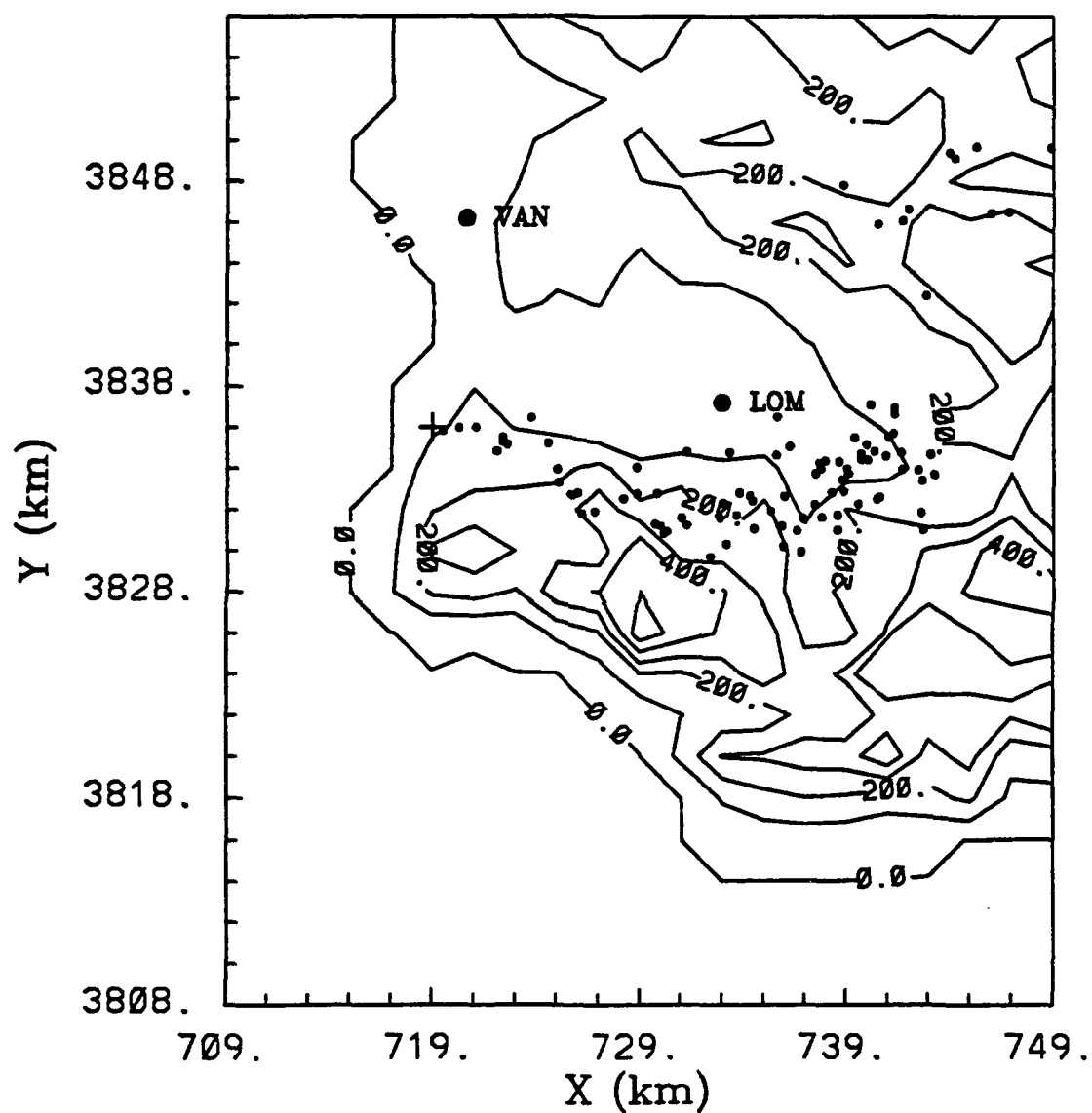


Figure 32. Modeled Trajectories of Puff-Centers Projected on the Surface at 1100 lst, June 13, 1966. Puffs were released continuously for 20 hours starting at 0600 lst, June 13, 1966. The results were obtained by a MicroVax 2000.

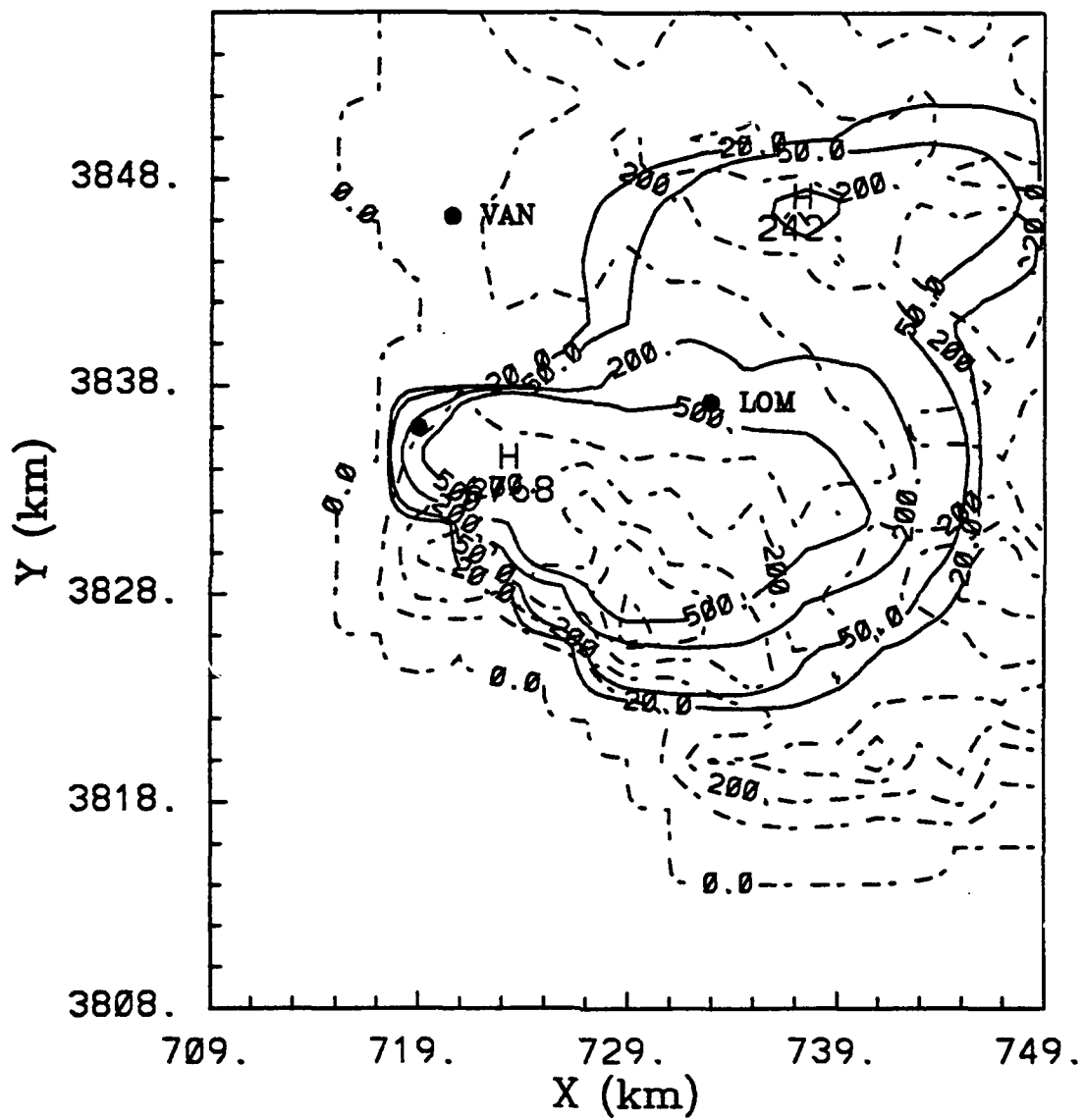


Figure 33. Concentration Distribution (in arbitrary units) of Fluorescent Particles at Ground Level at 1100 lst, June 13, 1966. The results were obtained by a MicroVax 2000.

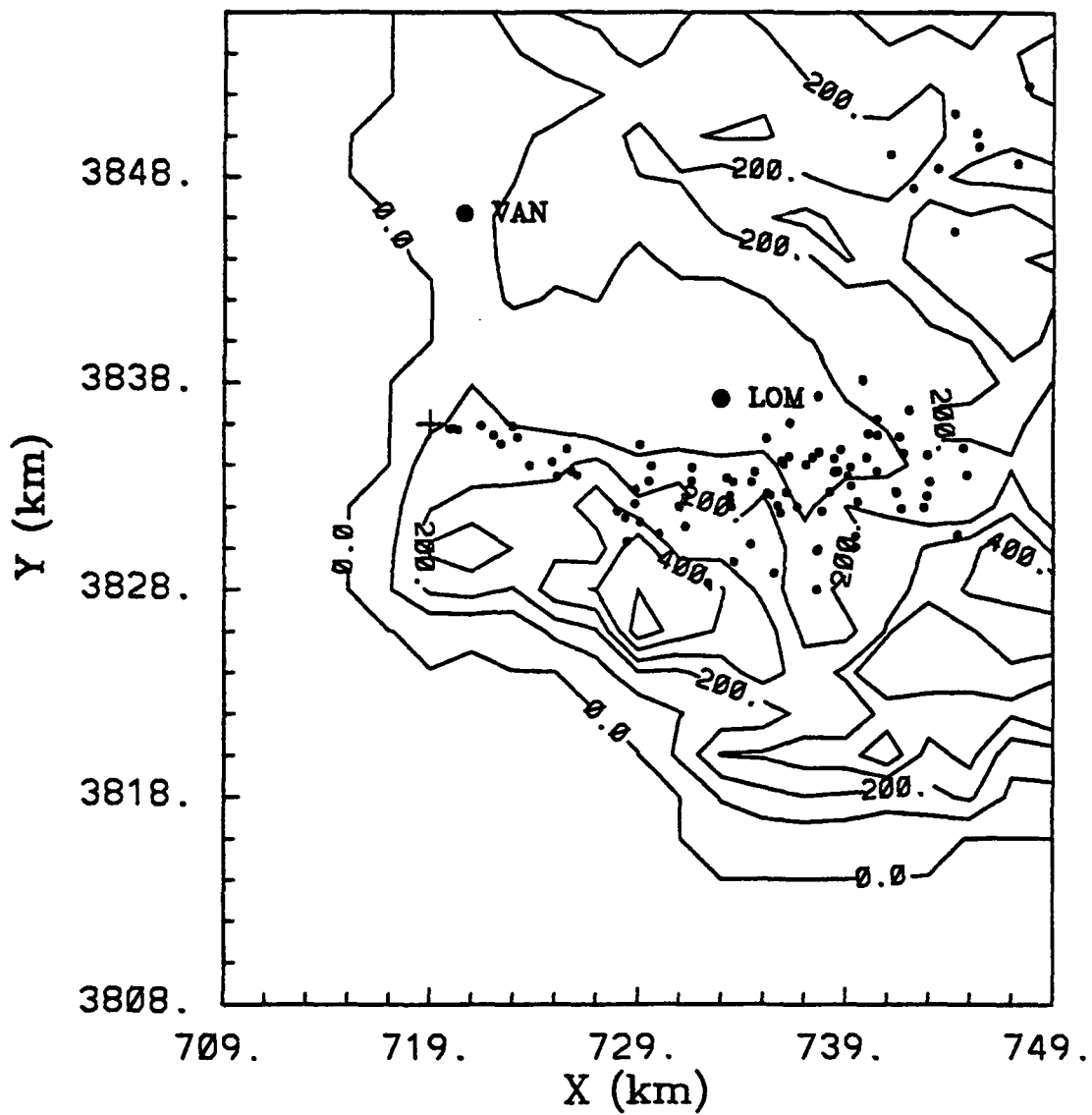


Figure 34. Same as in Figure 32, but the Results were Obtained by a Sun 4/110 Work-station.

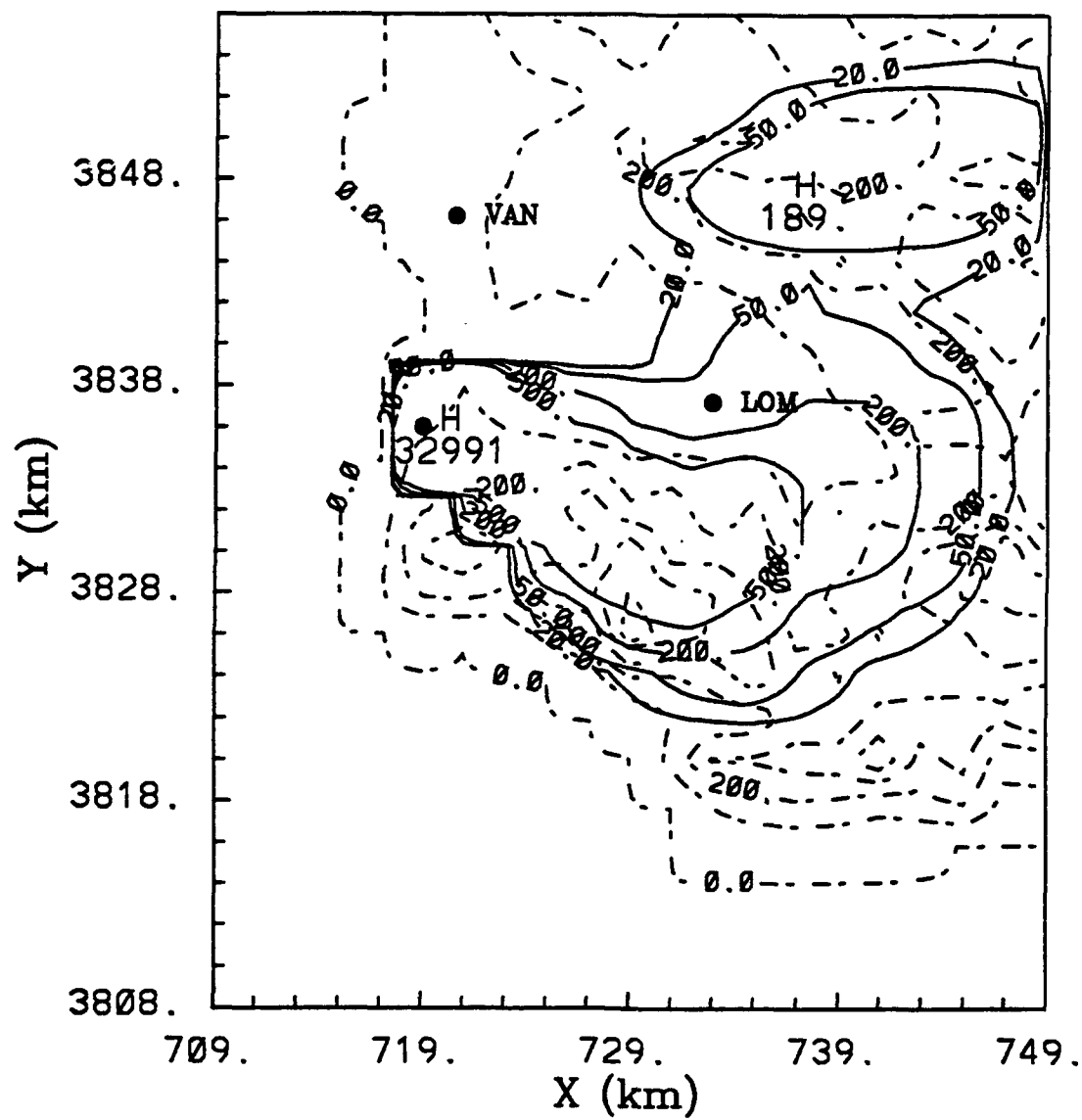


Figure 35. Same as in Figure 33, but the Results were Obtained by a Sun 4/110 Work-station

## SECTION VII

### BUOYANT PLUMES

In this section, we will investigate positive and negative buoyancy effects in HOTMAC and RAPTAD (Phase III tasks).

The most widely used method in treating a buoyant plume is based on a plume-rise theory advanced by Briggs (Reference 14). One can estimate the height where the plume levels off. This height is referred to as an effective stack height. Therefore, the simplest way to deal with a buoyant plume is to apply the Briggs formula in the initial stage when the buoyancy effect is significant. When the plume becomes neutrally buoyant, RAPTAD can be applied as before except that a stack height is replaced by an effective stack height.

There have been some efforts (e.g., Reference 15) to incorporate the buoyancy effect into a puff model. Thus, a puff model can be used from an initial stage and a patchwork with a plume-rise model is not needed. Indeed, the puff model by Gaffen et al. (Reference 15) used a concept very similar to that used for a plume-rise model to include the buoyancy effect.

The advantage of a plume-rise model is its simplicity. A plume rises because its density is smaller than that of the ambient air, and it levels off when it loses buoyancy by mixing with the ambient air. The entrainment process, or mixing rate, is, however, dependent upon a complex, turbulent heat and mass exchange between a puff and the ambient air, but the entrainment process is greatly simplified in a plume-rise model. Both a plume-rise model and a puff model assume that a buoyant plume does not perturb the dynamics of the ambient flows. In other words, the ambient flow conditions influence the plume dynamics, but not vice versa. For this reason, a plume-rise model and a puff model are referred to as a "passive plume-rise model" in this study.

On the other hand, we expect that a high-intensity buoyant plume, such as one that would result from a large fire or explosion, would influence significantly the dynamics of the ambient flow conditions. A fire heats the air surrounding it and produces a low-pressure area. Horizontal pressure gradients generated by a fire force the air to move toward the fire. Convergence of horizontal wind vectors over a fire creates a vertical motion or a plume rise. Therefore, wind and temperature distributions are significantly different with and without a large heat source.

Furthermore, a large fire generates vigorous turbulent motion because temperature stratification becomes extremely unstable as a result of intense heating.

A passive plume-rise model cannot, and is not designed to, address the alterations of the ambient flow conditions. Thus, its application is limited to a relatively low intensity heat source.

An equally interesting problem arises when a high-density and/or a low-temperature gas is released in the air. If a dense gas is spilled at the surface, the gas spreads horizontally and can stay in the surface layer for a long period of time, because the density stratification over a contaminated area is very stable and turbulent mixing is substantially suppressed. Therefore, we expect that a dense gas behaves and impacts the ambient flows quite differently from a buoyant plume. For this reason, people have developed different models to treat a dense gas and a plume rise.

In this section, we will investigate the feasibility of incorporating positive and negative source buoyancy effects in HOTMAC and RAPTAD. Our approach is quite different from that of a passive plume-rise model. We specify a heat source as a boundary condition; then the governing equations in HOTMAC compute wind, temperature, and turbulence distributions. RAPTAD uses the HOTMAC variables to determine the centroid location and size of each puff. Unlike a plume-rise model, a puff in RAPTAD is a tracer that follows precisely the turbulent fluid motion. Our approach in this study is referred to as a "dynamic plume model."



The advantage of a dynamic plume model is that the fluid motions and turbulent processes are consistent with the physical laws expressed by the governing equations. In other words, we can minimize the ambiguities and inconsistencies introduced in a passive plume model. For example, methods used in a passive plume model to define the parameters of turbulent entrainment processes are based on simple and idealized conditions. A passive plume model, by definition, cannot provide feedback to the ambient flow conditions. For example, vertical motions resulting from a plume rise do not affect the distribution of horizontal wind components in the background flow. Of course, this is inconsistent with mass continuity.

The disadvantage of a dynamic plume model is its complexity. We must solve, numerically, a set of three-dimensional hydrodynamic models with appropriate initial and boundary conditions. Reaching these solutions requires considerable knowledge and experience in fluid dynamics and numerical modeling. Furthermore, the computations could be quite expensive, because a very small integration time step is used to ensure computational stability.

Therefore, a dynamic plume model is currently limited to research applications. We expect that it will become practical for an operational use in the near future, because computer capabilities relative to cost will increase substantially in the future, particularly for engineering workstations.

We now discuss results of simulations from HOTMAC and RAPTAD where positive and negative buoyant sources are placed at the lower boundary of a computational domain. We use an area heat source to simulate plume rise associated with a fire and an area cold air distribution to simulate dense gas dispersion in the surface layer. Results are preliminary, because our purpose is to test the feasibility of incorporating a large heat source or a sink into HOTMAC. We did not attempt to evaluate the model performance against any observations in this study.

## A. POSITIVE BUOYANT SOURCE

We have selected the simplest boundary condition because we would like to isolate the effects of the positive buoyancy source on air flow from any other causes that might influence the flow. We have chosen a flat surface boundary and a nighttime simulation period to exclude the diurnal variation of the solar heating.

The computational domain was  $20 \times 20 \times 10$  km in  $x$ ,  $y$ , and  $z$  directions, respectively, and the horizontal grid spacing was 500 meters. The grid spacing in the vertical direction is variable with height: 4 meters near the surface and 1000 meters close to the top of computational domain. A total of  $41 \times 41 \times 31$  grid points represented the computational domain. An area heat source of  $3 \times 4$  km<sup>2</sup> was placed between  $x = 14.25$  and  $17.25$  km and  $y = 7.75$  and  $11.75$  km in the computational domain. We adopted a heat flux of  $50,000$  W/m<sup>2</sup>, which corresponds to an extremely large fire.

Initially, wind and potential temperature distributions were assumed uniform in the horizontal directions. The vertical profile of the initial east-west wind component was obtained from a logarithmic profile  $U/u_* = 1/k \ln (z + z_0)/z_0$  where  $u_* = 0.2$  m/s,  $z_0 = 0.1$  meters, and  $k = 0.4$ . The north-south wind component was zero initially. The vertical profile of the initial potential temperature was  $20^\circ\text{C}$  at the ground and increased with height at a rate of  $0.001^\circ\text{C/m}$  up to 3000 meters above msl and at a rate of  $0.003^\circ\text{C/m}$  above that level.

Wind fields appear to reach a quasi-steady state at 20 minutes after the initiation of heating. The heating rate was kept constant during the entire simulation period. Thus, wind, temperature, and turbulence distributions discussed here are for those at 20 minutes after the fire was initiated. Figure 36 shows a horizontal wind vector distribution at 30 meters above the ground. Horizontal wind vectors converge over a point slightly downwind of the western boundary of the fire. If the prevailing wind were zero, the convergence should have occurred at the center of the fire.

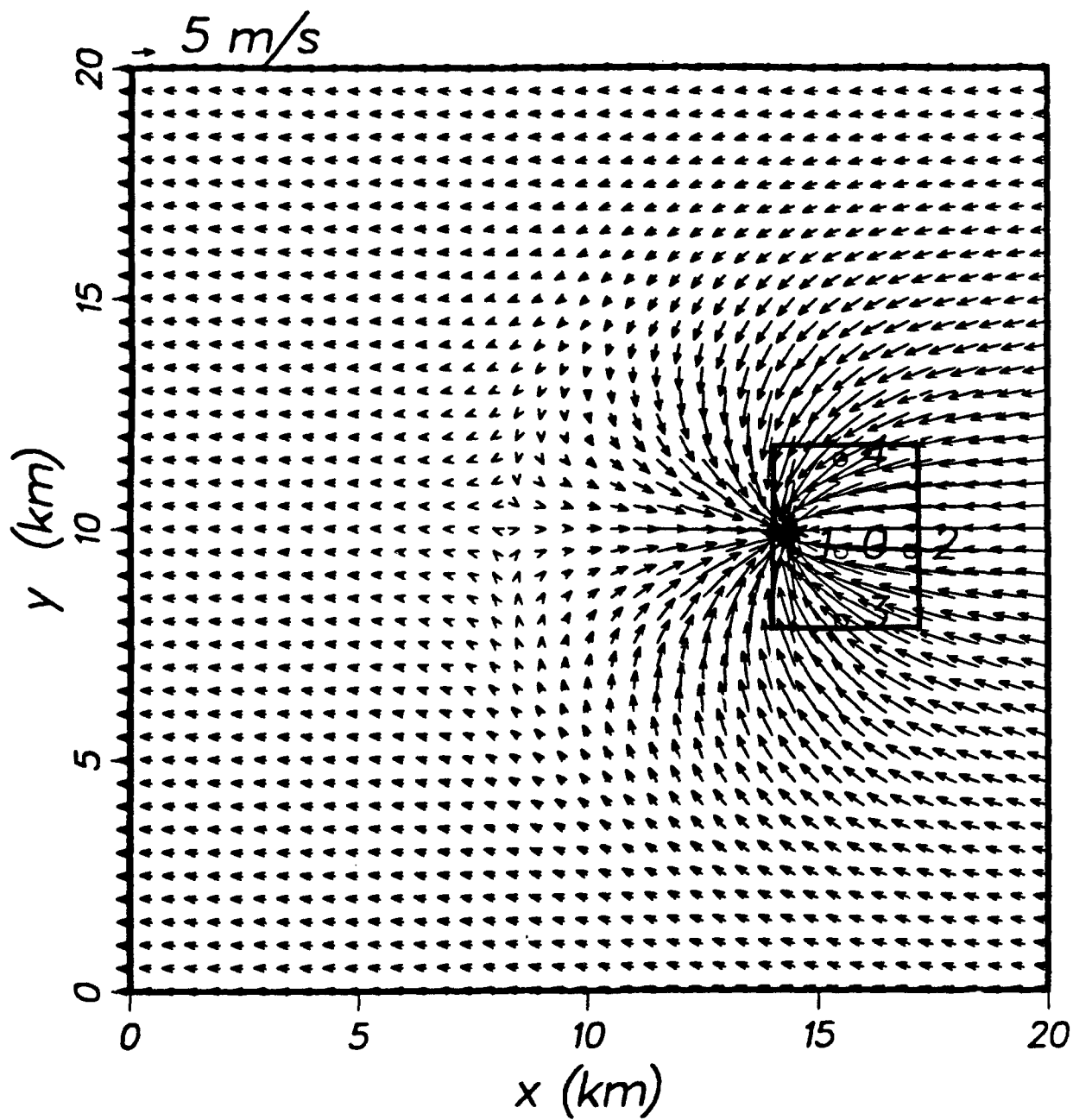


Figure 36. Horizontal Wind Vector Distribution at 30 meters above the Ground. The heated area is indicated by a rectangle.

The convergence of the horizontal wind vectors decreased in magnitude with height, and the wind vector distribution switched to divergence at the higher levels. This is the consequence of the mass continuity constraint imposed in the model. The switch from convergence to divergence occurred at approximately 2000 meters above the ground. Perturbations caused by a fire were negligible at levels higher than 6500 meters above the ground.

Wind vectors in east-west vertical cross sections along the southern boundary and the central axis of the fire are shown in Figure 37. These wind vectors show large undulations: a strong subsidence in front of the fire and an extremely large lift over the convergence zone followed by another subsidence. Convergence of horizontal wind vectors in the surface layer and return flows generated well-established rotors downwind of the fire. The maximum vertical velocity was 43.5 m/s, and the maximum horizontal velocity was 18.5 m/s.

Wind vectors in north-south vertical cross sections along  $x = 14.5$  km, 16 km, and 17 km are shown in Figure 38. Wind vector distributions in the vertical cross section along the western boundary of the fire ( $x = 14.5$  km) clearly show almost symmetric vortices for each side of the fire. The wind vectors along the north-south centerline of the heated area ( $x = 16$  km) exhibit much smaller vortices than those at  $x = 14.5$  km. The updraft over the central part of the heated area diminishes at approximately 3.5 km above the ground and is replaced by a downdraft in the upper levels. Wind vectors along the eastern boundary of the fire ( $x = 17$  km) indicate that the air motions are mostly downward.

The fire produced very large vertical velocities (over 40 m/s) along the fire column over the convergence point of the horizontal wind vectors. The question arises whether the hydrostatic approximation assumed here is still valid. We repeated the simulation with a nonhydrostatic code and obtained results very similar to those reported here. The magnitude of the dynamic pressure obtained in the nonhydrostatic pressure computation was less than 1 percent of the

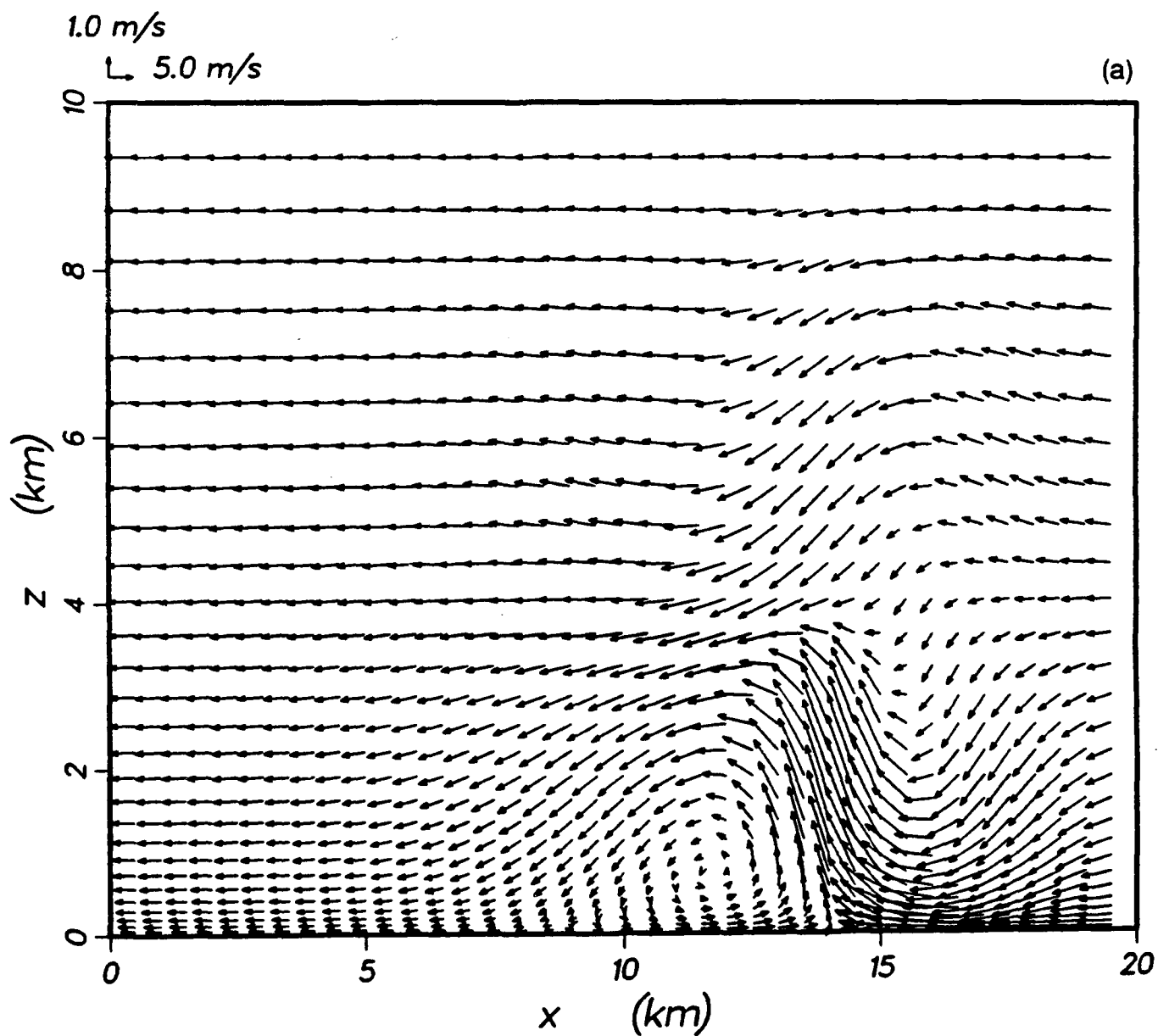


Figure 37. Wind Vectors in East-West Vertical Cross Sections along (a) the Southern Boundary and (b) the Central Axis of the Fire.

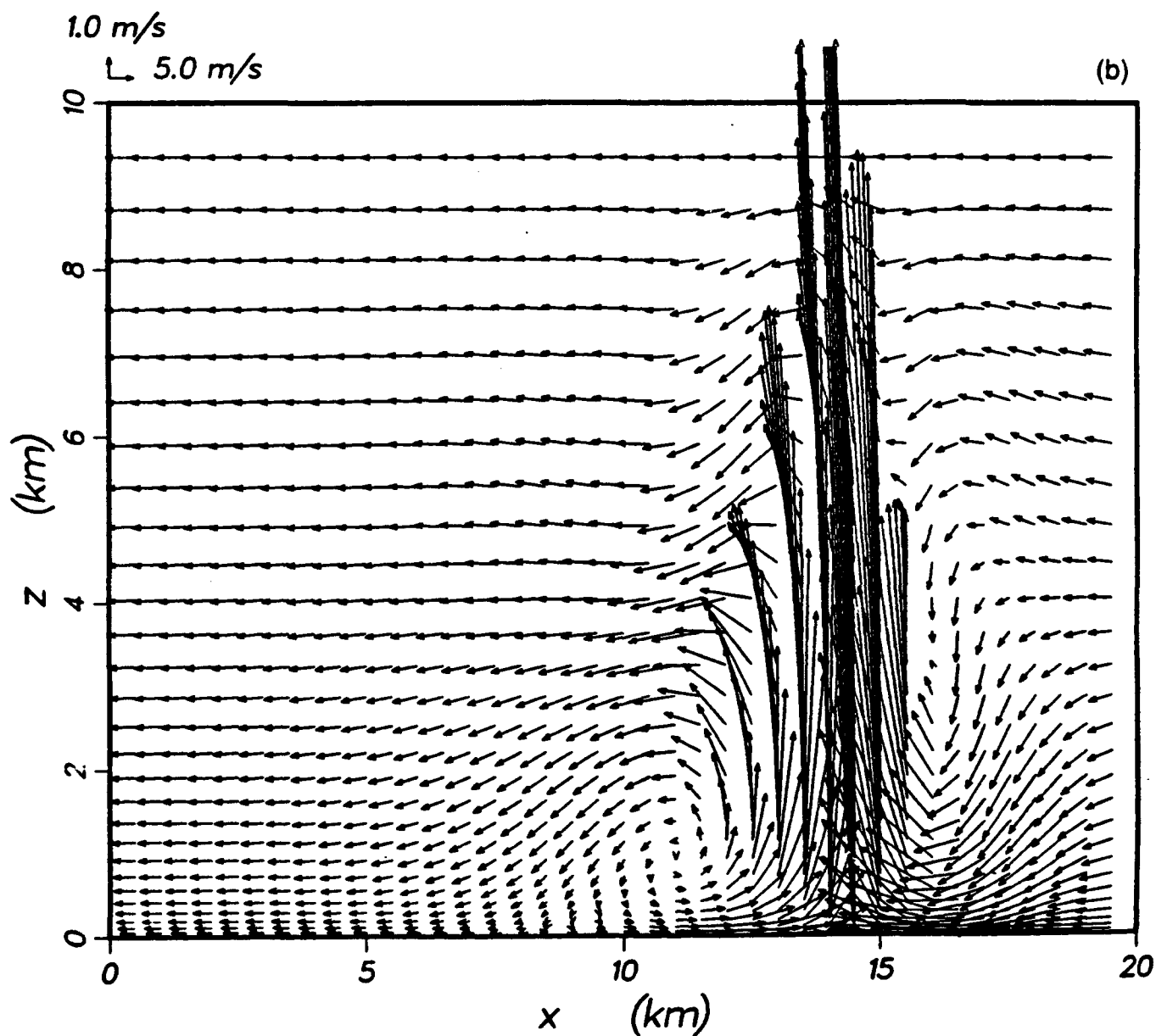


Figure 37. Wind Vectors in East-West Vertical Cross Sections along (a) the Southern Boundary and (b) the Central Axis of the Fire.

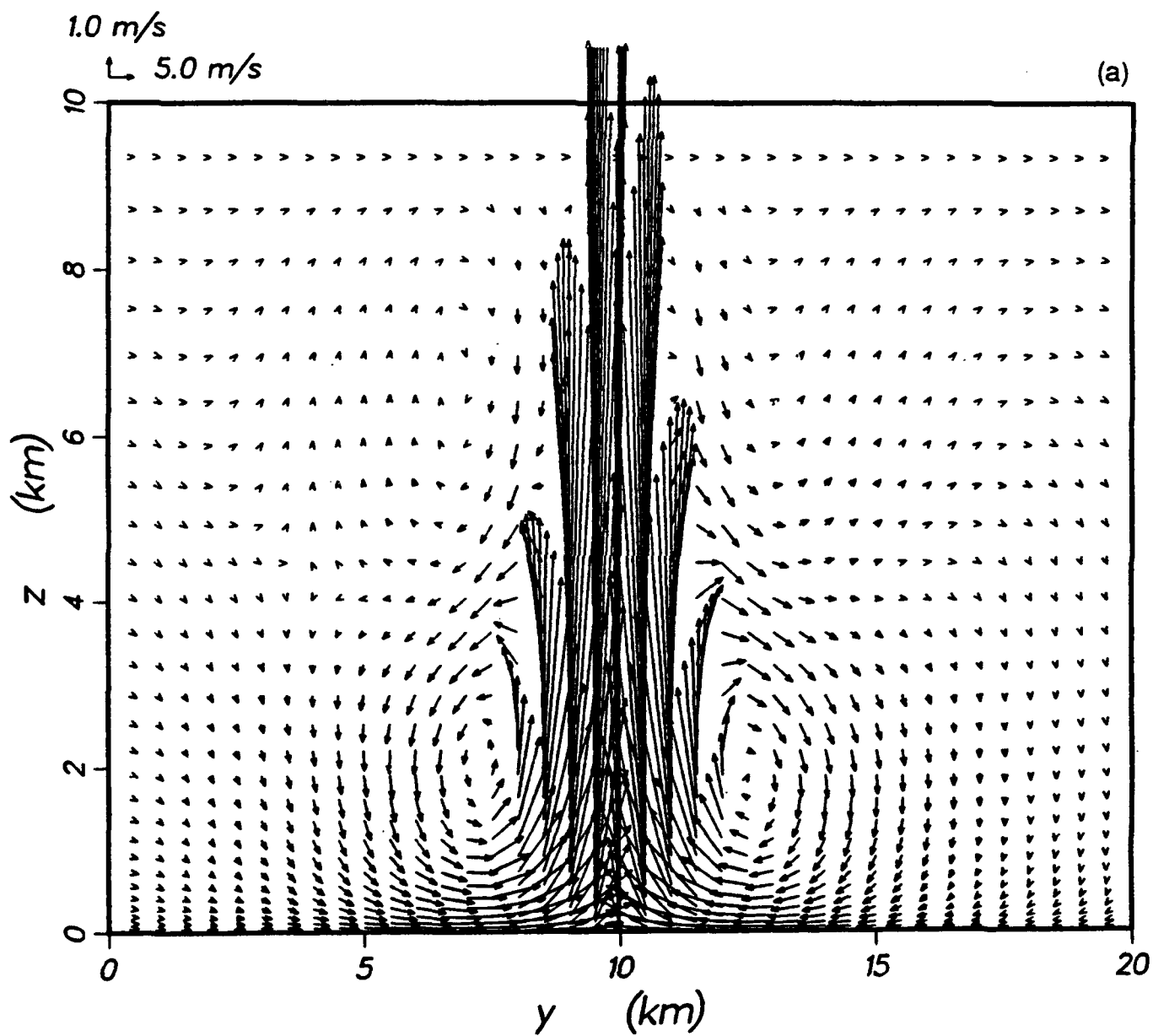


Figure 38. Wind Vectors in the North-South Vertical Cross Sections along (a)  $x = 14.5$  km, (b)  $x = 16$  km, and (c)  $x = 17$  km.

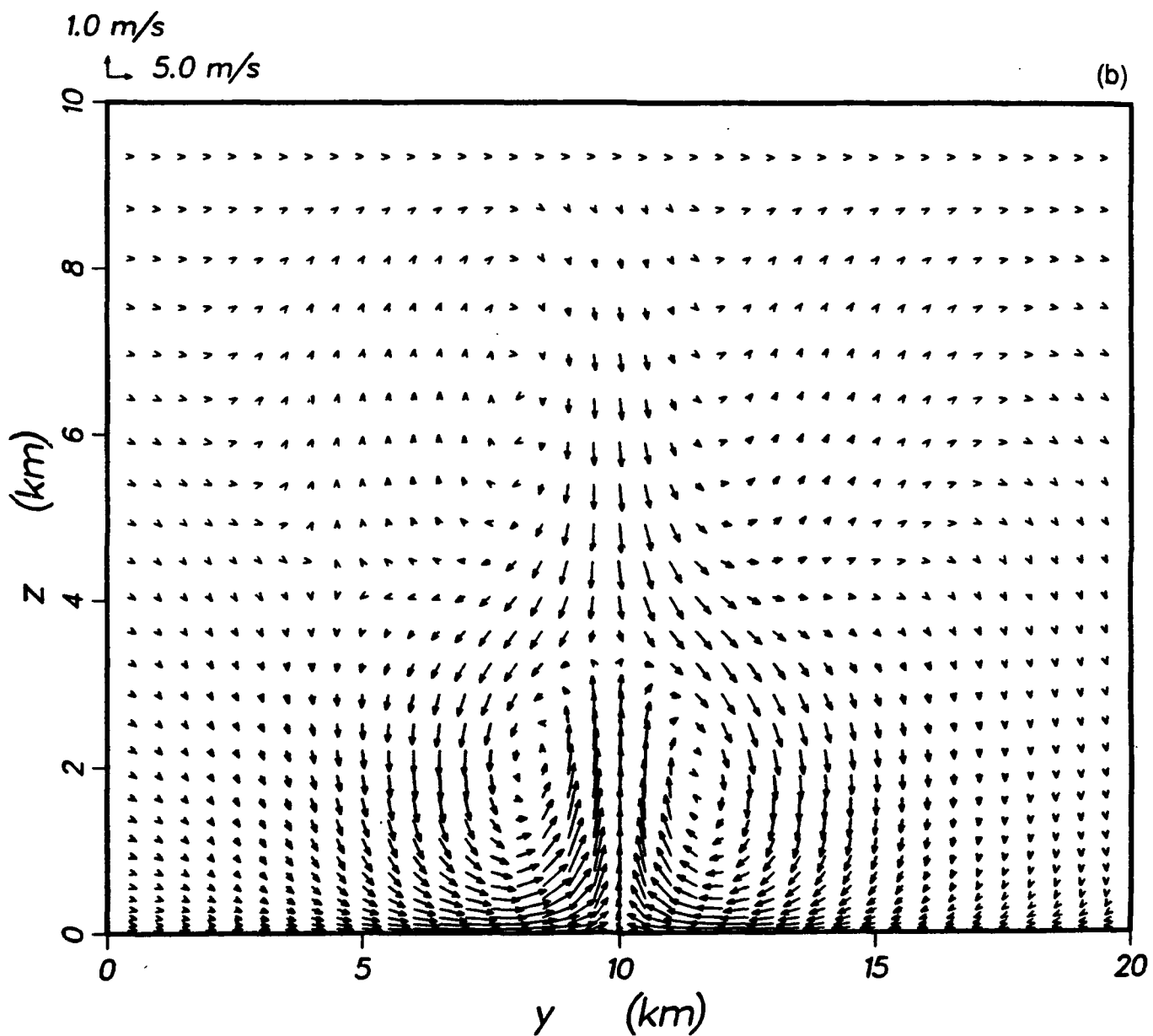


Figure 38. Wind Vectors in the North-South Vertical Cross Sections along (a)  $x = 14.5$  km, (b)  $x = 16$  km, and (c)  $x = 17$  km.



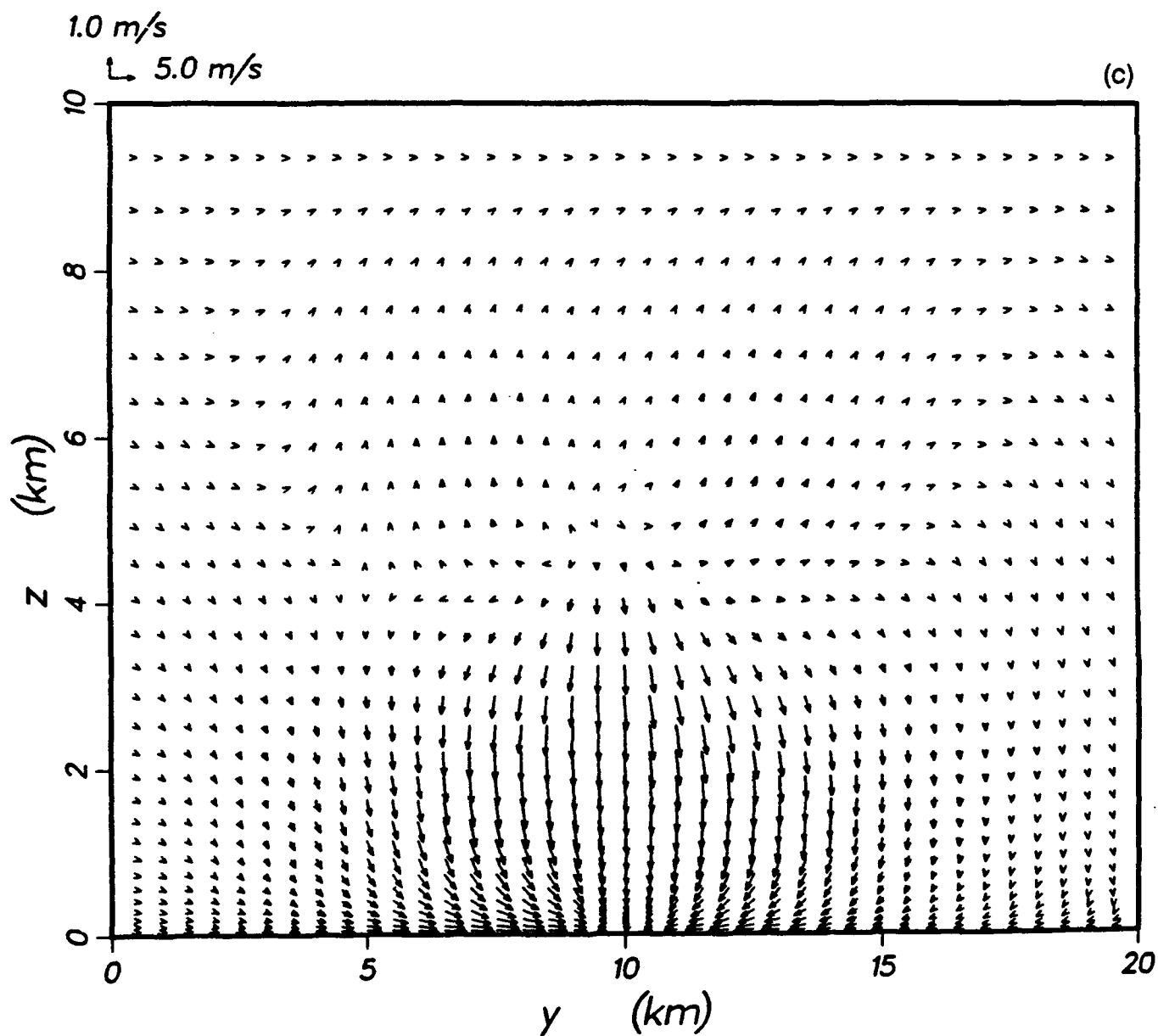


Figure 38. Wind Vectors in the North-South Vertical Cross Sections along (a)  $x = 14.5$  km, (b)  $x = 16$  km, and (c)  $x = 17$  km.

hydrostatic pressure. Thus, we tentatively conclude that the hydrostatic pressure approximation is still valid even for a large heat source. This conclusion may depend on the horizontal grid resolution used in a model because a coarse grid tends to underestimate horizontal derivatives of wind distribution. Those terms are the main contributors to the dynamic pressure.

The fire modified considerably not only mean winds but also turbulence variables. A heat flux of  $50,000 \text{ W/m}^2$  over the fire area resulted in a maximum surface temperature of  $367^\circ\text{C}$  near the western boundary of the fire where the convergence of horizontal wind vectors was observed. The surface temperatures over the heated area were over  $300^\circ\text{C}$  everywhere. The heat energy from a fire becomes a buoyancy source of atmospheric turbulence. Figure 39 shows the vertical profiles of standard deviation of vertical velocity, twice turbulence kinetic energy, and standard deviation of potential temperature at site 1 (Figure 36), which is located near the center of the western boundary of the fire. The values for turbulence kinetic energy reported in Figure 39 are at least 20 times larger than those encountered in the convective atmospheric boundary layer. Turbulence reached 6000 meters above the ground, whereas a typical atmospheric boundary layer height is approximately 2000 meters.

To visualize the extent of a plume rise, we released puffs continuously over the heated area. Figure 40 shows three-dimensional projections of puff centroids at 20, 40, and 60 minutes after the release, respectively. Puffs close to the ground first moved toward the convergence point, which is located near the center of the western boundary of the fire. The updraft over the convergence zone transported puffs upward over 8800 meters above the ground. Puffs detrained from the fire column in the levels between 2000 and 8800 meters above the ground where horizontal wind vectors were divergent.

## B. NEGATIVE BUOYANT SOURCE

Because of the nature of the chemicals dealt with at VAFB, little emphasis is placed

site 1    day 182    0020 lst    grid 1

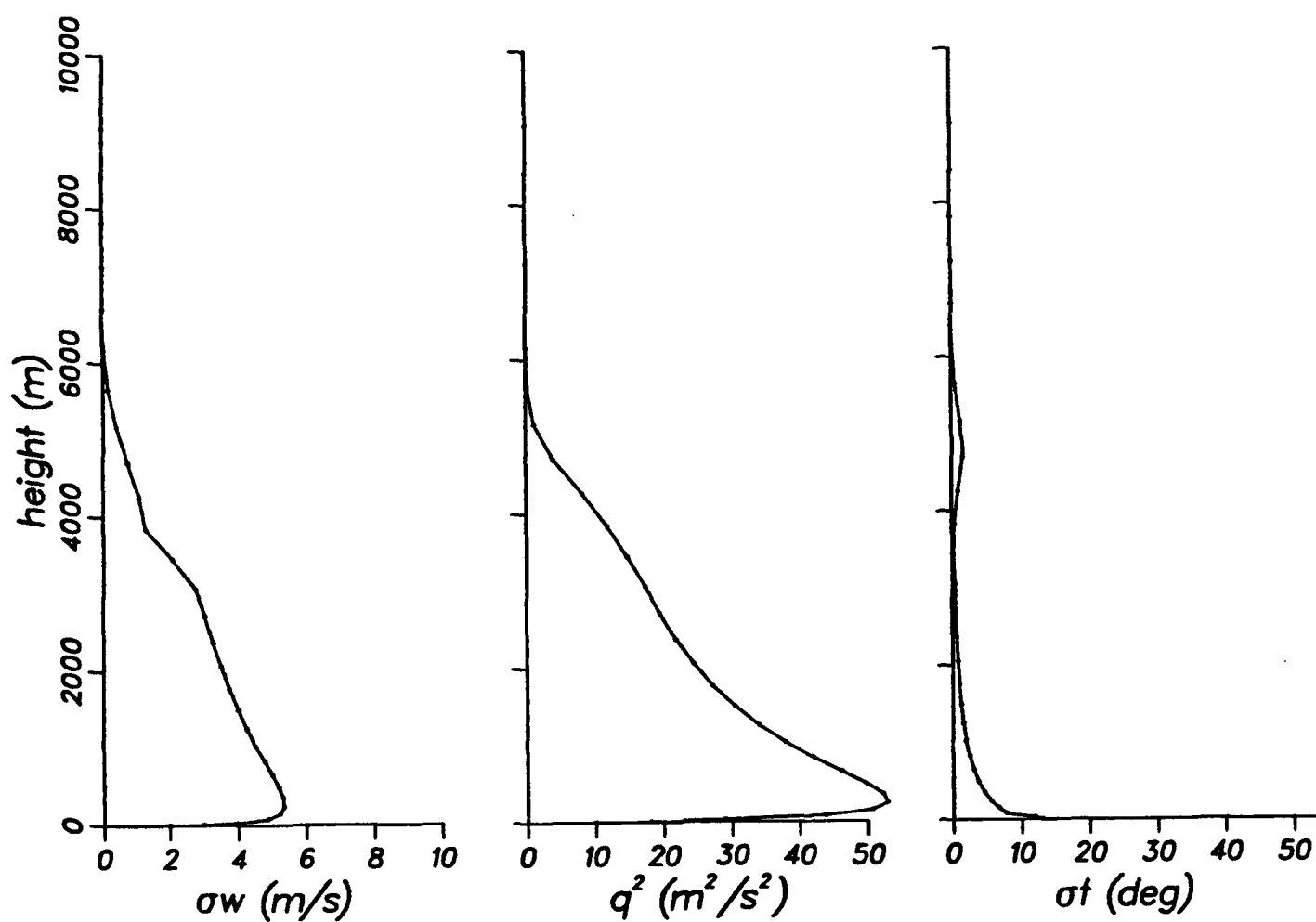


Figure 39. Vertical Profiles of Standard Deviation of Vertical Velocity,  $\sigma_{wi}$ ; Twice Turbulence Kinetic Energy,  $q^2$ ; and Standard Deviation of Potential Temperature,  $\sigma_t$ .

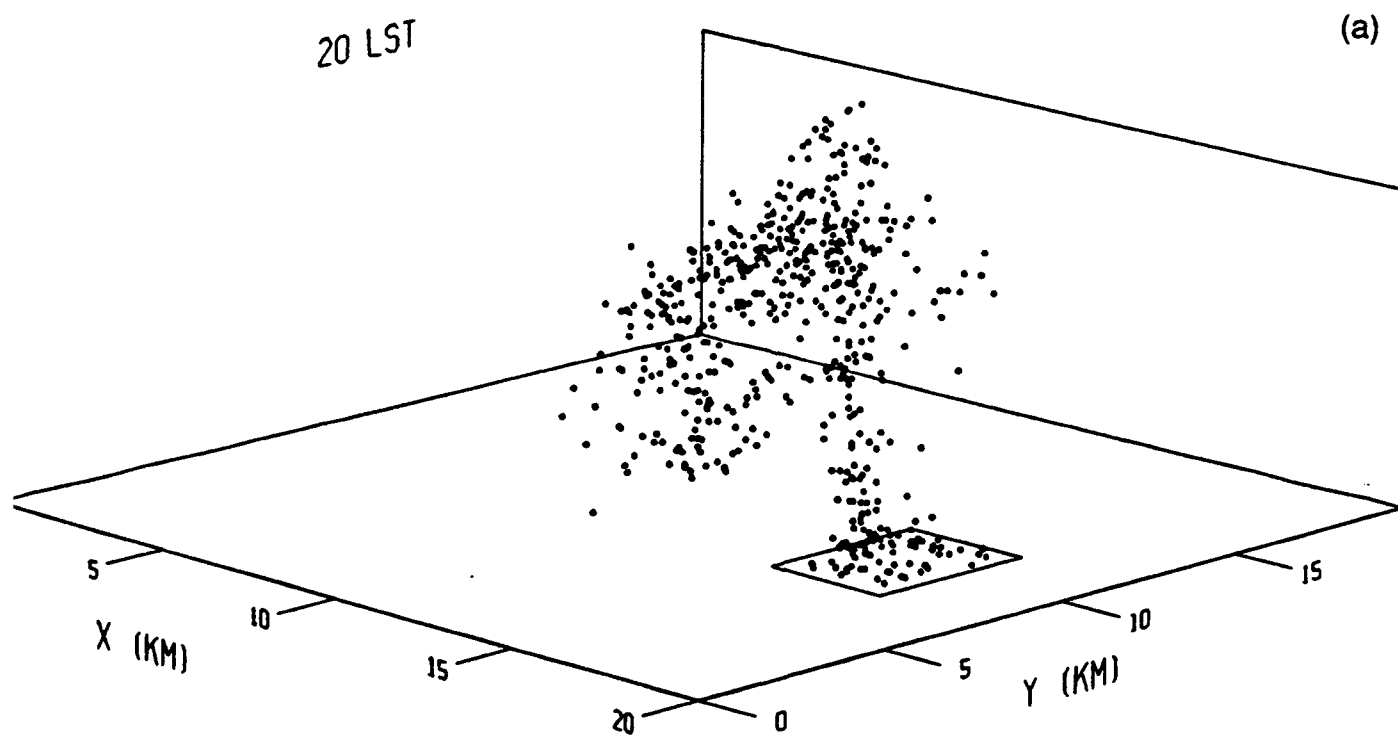


Figure 40. Three-Dimensional Projections of Puff Centroids at (a) 20 minutes, (b) 40 minutes, and (c) 60 minutes after the Release.

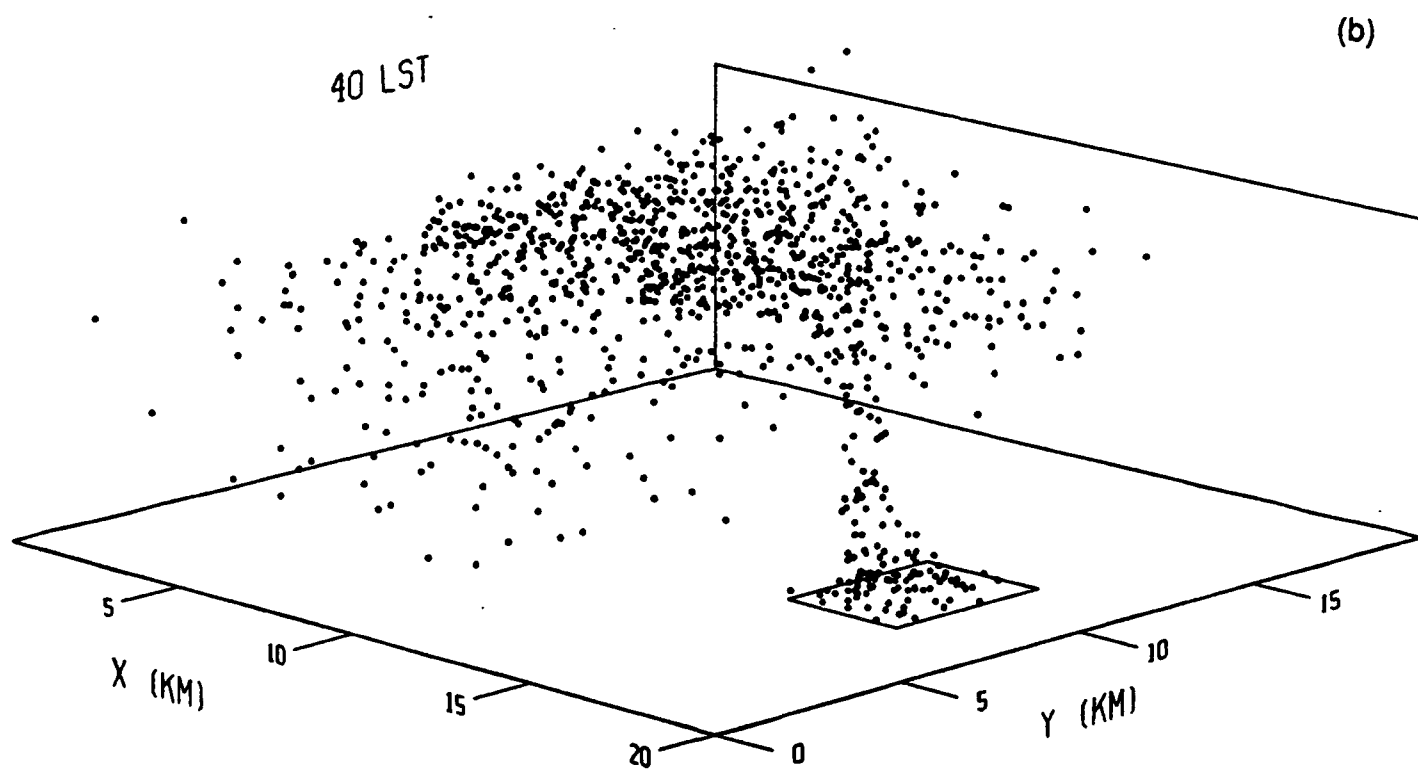


Figure 40. Three-Dimensional Projections of Puff Centroids at (a) 20 minutes, (b) 40 minutes, and (c) 60 minutes after the Release.

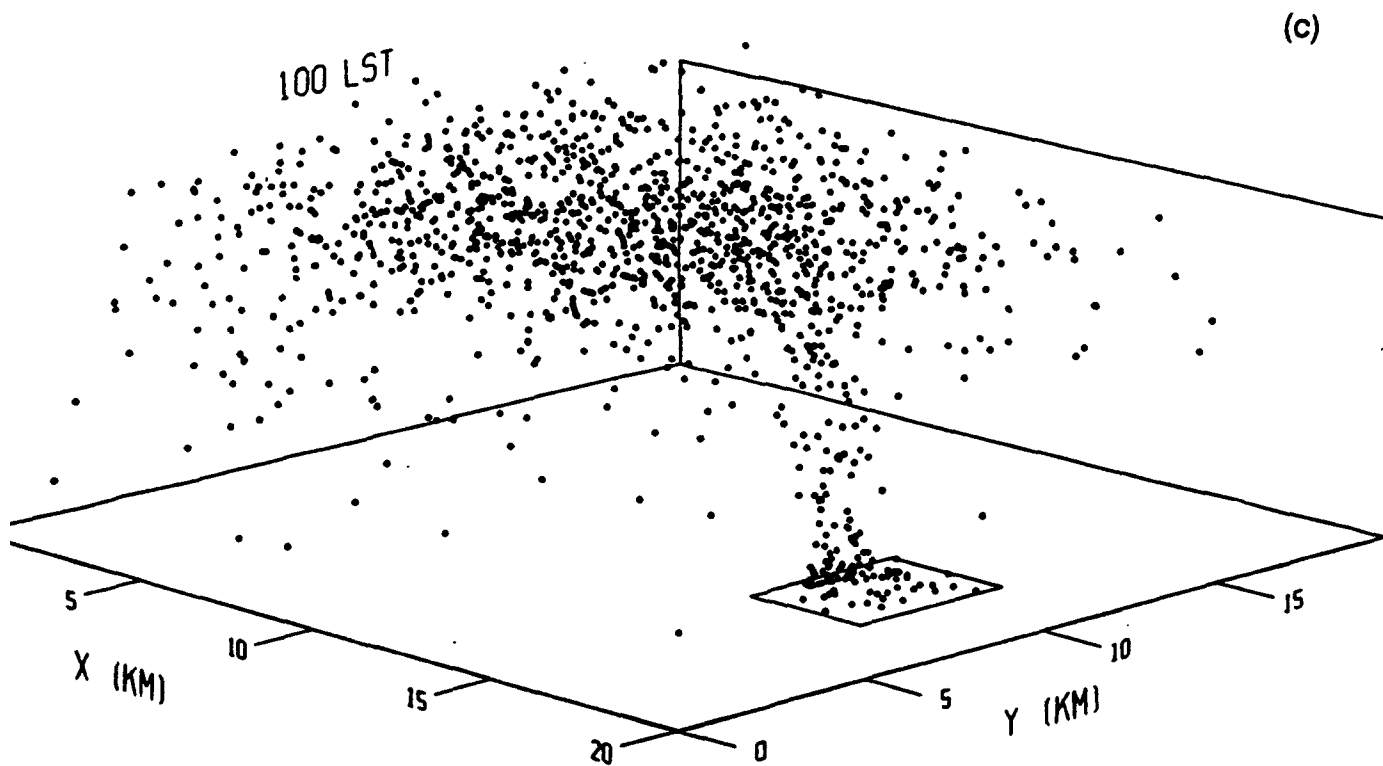


Figure 40. Three-Dimensional Projections of Puff Centroids at (a) 20 minutes, (b) 40 minutes, and (c) 60 minutes after the Release.

on a negative buoyant source at this initial stage of testing the feasibility of operating HOTMAC/RAPTAD with the VAFB terrain. Gas can be heavier than air when its molecular weight is greater than that of air, or when its temperature is lower than that of air, or when both conditions exist. In this section, the terms “negative buoyant source,” “gas heavier than air,” and “dense gas” are used interchangeably.

The approach used to incorporate a negative buoyant source in HOTMAC is similar to that used to incorporate a positive buoyant source, as discussed in the previous subsection. Again, we made no effort to verify the model results with observations.

We selected a computational domain of 80 x 140 x 5 km in x, y, and z directions, respectively. For simplicity, we assumed that the surface was flat and that wind and temperature distributions were initially uniform in the horizontal directions. Initially, wind direction was southerly and wind speed was 3 m/s. Initial potential temperature was 30°C at the surface and increased with height at a rate of 0.010°C/m up to 700 meters above the ground. The lapse rate decreased to 0.00236°C/m for the rest of the levels up to the top of the computational domain.

Horizontal grid spacing was 4 km, and vertical grid spacing varied with height. We placed near the center of the computational domain a cold area of 8 x 8 km with a temperature of -150°C. The integration was initiated at 0300 lst and lasted for 6 hours.

Figure 41 shows the distribution of horizontal wind vectors at 10 meters above the ground at 0400 lst. As expected, the wind field diverges over the cold area where the surface pressure was higher than the surroundings. The wind perturbations were confined in the layer less than 30 meters from the ground, and turbulence intensity was very small. We released puffs continuously, starting at 0400 lst. Figure 42 shows the locations of puff centroids projected on the ground at 0500 lst and 0900 lst, respectively. Puffs were initially coherent but bifurcated with time because of the divergent nature of the wind field over the cold area (Figure 41).

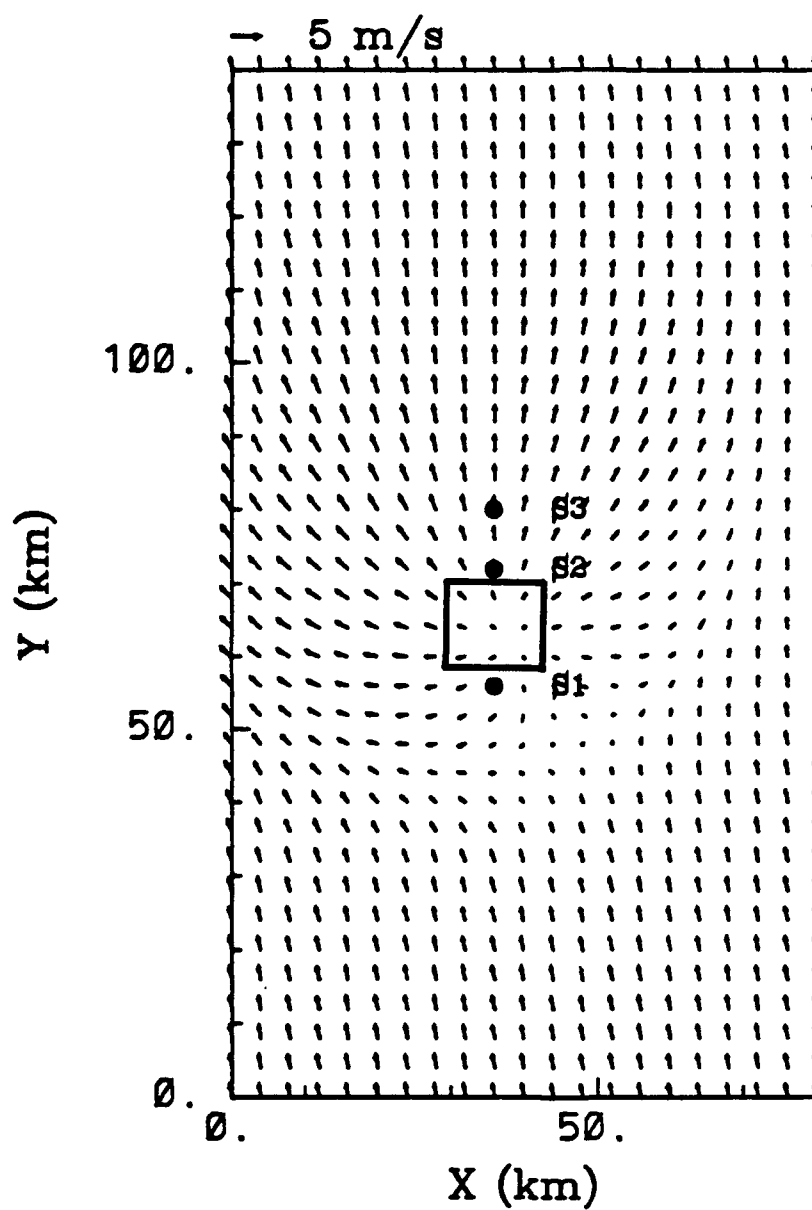


Figure 41. Horizontal Wind Vectors at 10 meters above the Ground at 0400 lst. The cold area is indicated by a rectangle.



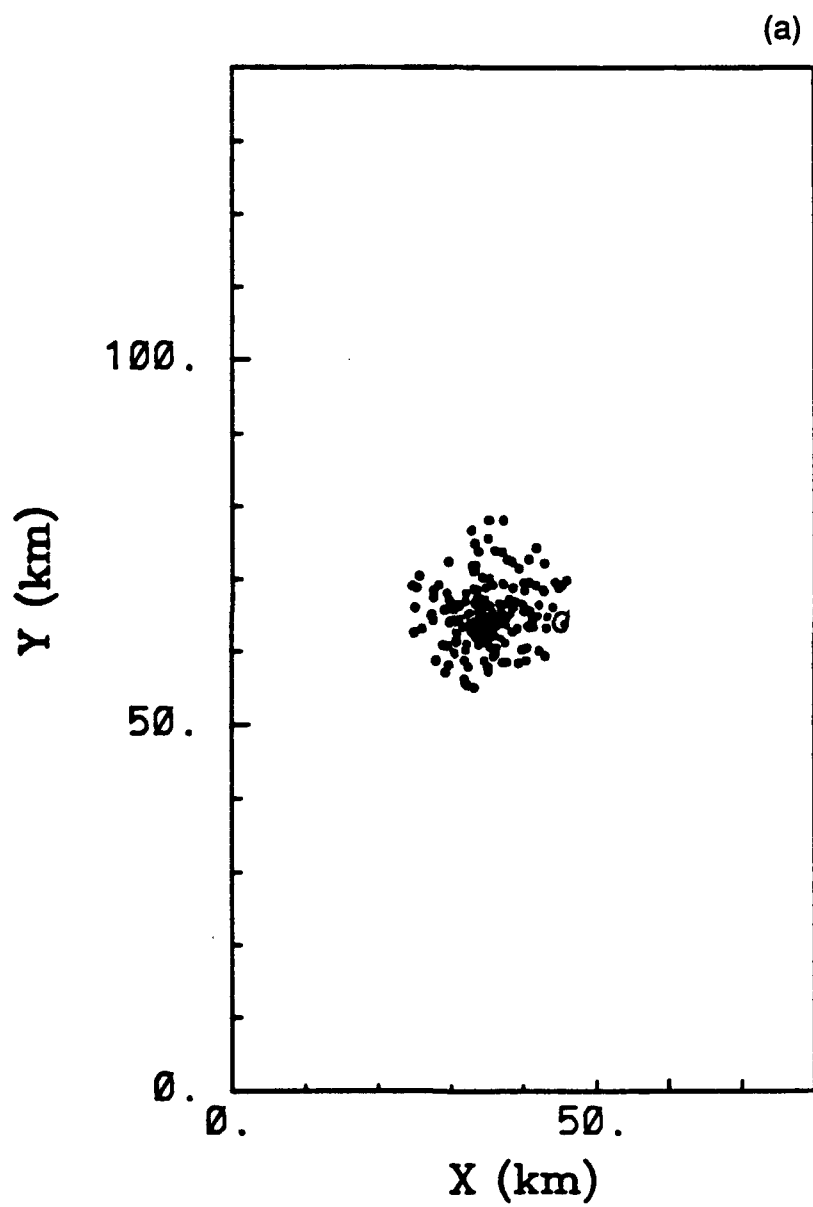


Figure 42. Projections of Puff Centroids on the Ground at (a) 0500 lst and (b) 0900 lst.

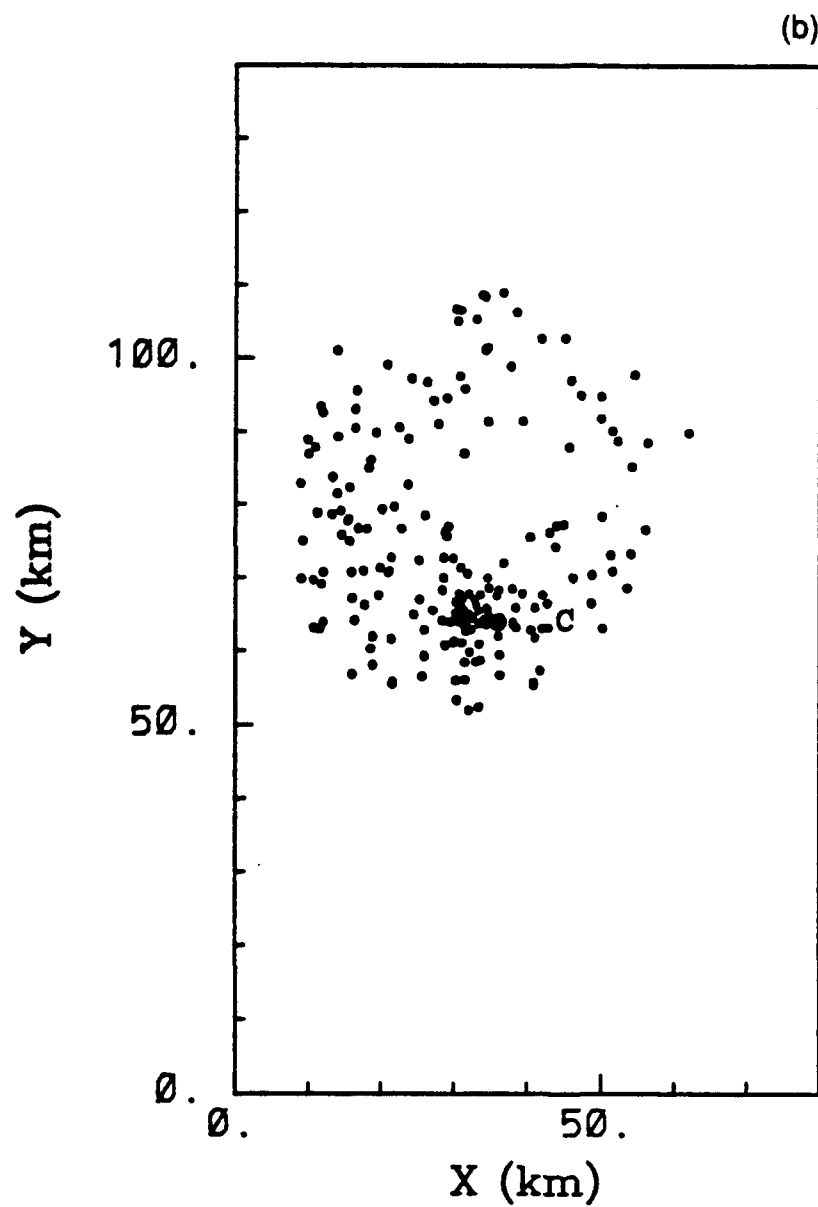


Figure 42. Projections of Puff Centroids on the Ground at (a) 0500 lst and (b) 0900 lst.

Figure 43 shows the surface concentration contours (in arbitrary units) at 0500 lst and 0900 lst, respectively. Both figures show that the distributions are not Gaussian, and bifurcations are evident, particularly at 0900 lst.

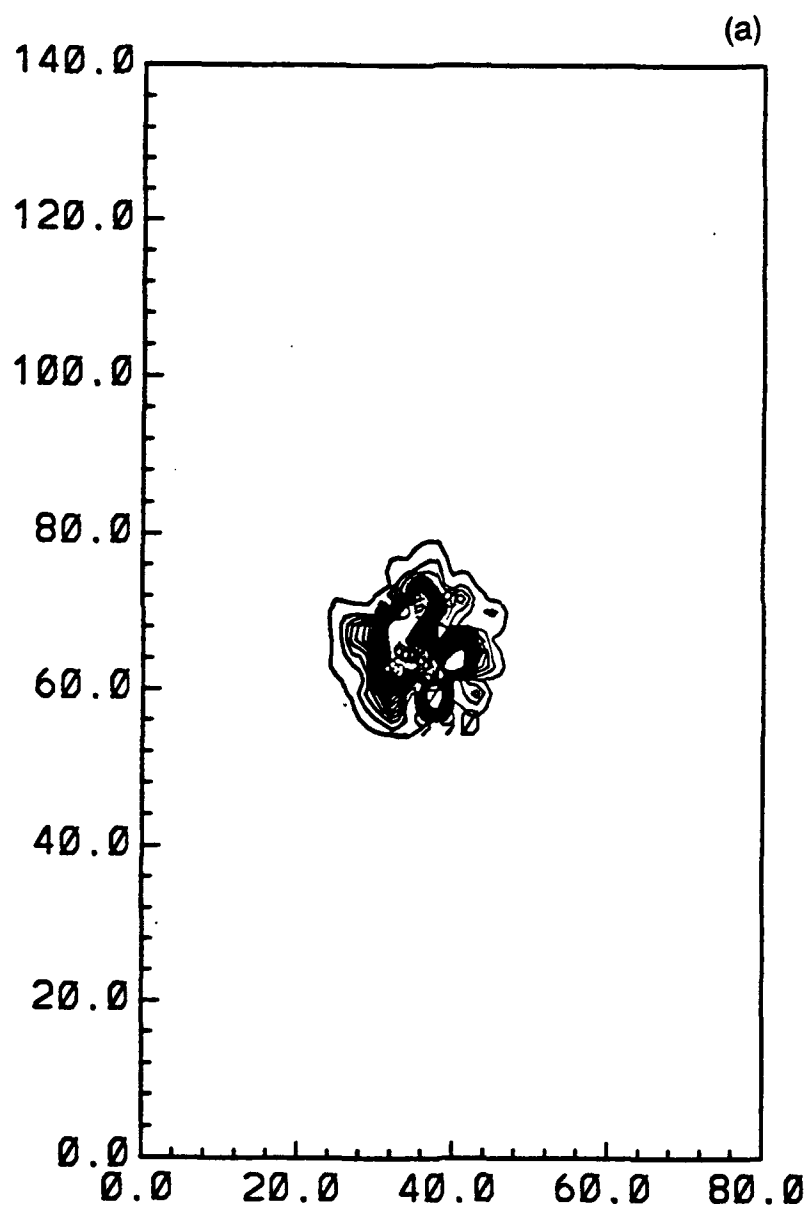


Figure 43. Surface Concentration Contours (in arbitrary units) at (a) 0500 lst and (b) 0900 lst.

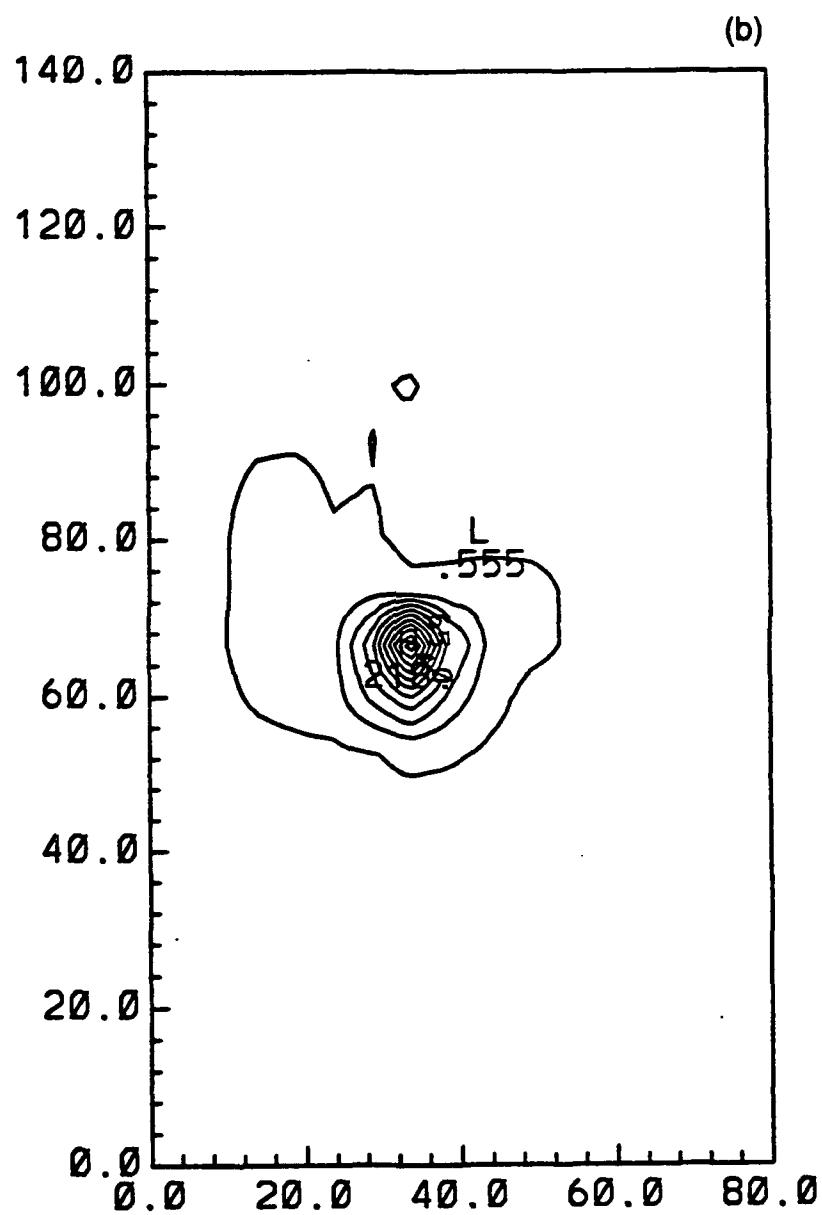


Figure 43. Surface Concentration Contours (in arbitrary units) at (a) 0500 lst and (b) 0900 lst.

## SECTION VIII

### CONCLUSIONS AND RECOMMENDATIONS

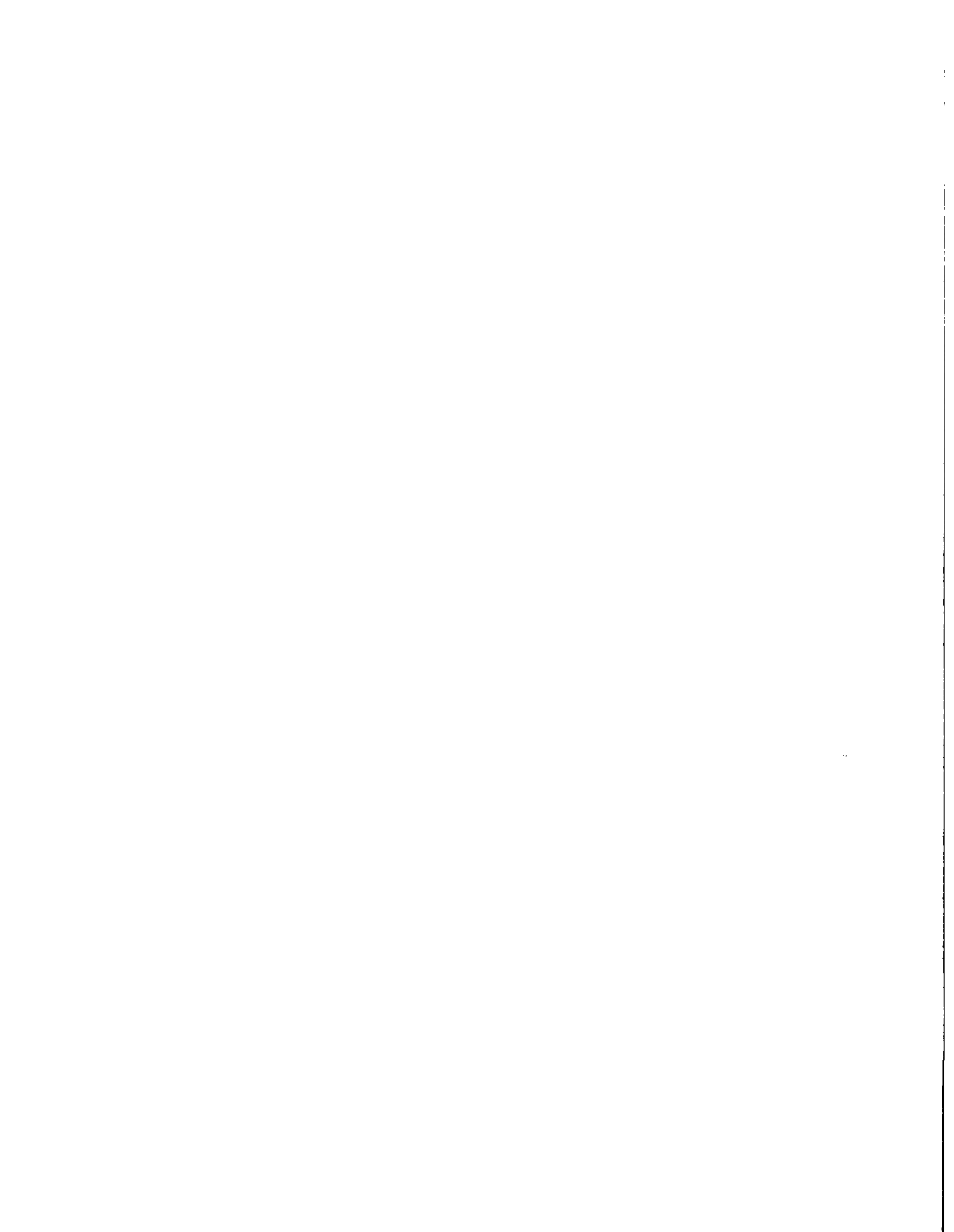
#### A. CONCLUSIONS

- It is feasible to operate the three-dimensional atmospheric models HOTMAC and RAPTAD to forecast the transport and dispersion of airborne materials at VAFB.
- HOTMAC and RAPTAD predictions were at least as good as those obtained by diagnostic models and the MI model where wind data were available.
- HOTMAC and RAPTAD predictions were far better than those obtained by diagnostic models and they were the best practical solution where wind data were not available.
- It is feasible to operate HOTMAC and RAPTAD on a desktop computer. HOTMAC took 4 hours 11 minutes and 22 hours 10 minutes CPU time, respectively, on a Sun 4/100 workstation, and a MicroVax 2000 computer for a 28 hour forecast with 21 x 25 x 16 grid points. RAPTAD took 26 minutes and 3 hours 45 minutes CPU time, respectively, on a Sun 4/110 workstation, and a MicroVax 2000 computer for a 20 hour simulation.
- The affordability and portability of the desktop computer has opened the door to upgrading toxic hazard modeling capabilities for emergency response management at VAFB.
- The HOTMAC and RAPTAD modeling system would be a useful addition to enhance current VAFB emergency response management capabilities.
- It is feasible to incorporate the positive and negative source buoyancy effects in HOTMAC and RAPTAD. Our approach can minimize the ambiguities and inconsistencies introduced in a simple plume rise model.

## B. RECOMMENDATIONS

- Become familiar with background theories and operating procedures of HOTMAC and RAPTAD. Install the models on a mainframe computer and repeat the simulations discussed in this report
- Consider upgrading computer capabilities for emergency response applications at VAFB. MicroVax computers may not be fast enough to operate HOTMAC and RAPTAD.
- Modify HOTMAC to run all the time and store wind and turbulence data for the next 24 hours. When an emergency occurs, RAPTAD can be used immediately with the wind data stored on a disk. The RAPTAD computation is much faster than that of HOTMAC. Thus, this approach meets better the time constraint imposed under emergency situations.
- Develop a method to integrate tower data into HOTMAC. The wind data can be used to initialize and correct the wind distribution in HOTMAC. These may be accomplished by a dynamical initialization technique and a four-dimensional data assimilation method.
- Develop a method to predict concentration variances which can be used to estimate uncertainties associated with predictions. A short time averaging value is required for predicting concentration of toxic materials. Such a value normally exhibits great variations in time and space.
- Add model physics necessary to simulate the evolution of fog formation and dissipation processes. Fog is frequently observed at VAFB and it affects the heat energy balance at the ground.
- Continue to investigate the feasibility of incorporating positive and negative source buoyancy effects in HOTMAC and RAPTAD and test the scheme with observations.

(The reverse of this page is blank)





## APPENDIX A

### DESCRIPTION OF MODELS AND NUMERICAL PROCEDURES

#### A. HOTMAC (Higher Orders Turbulence Model for Atmospheric Circulation)

##### 1. Model Equations

This model, also referred to as a "second-moment turbulence-closure model," is based on a set of second-moment turbulence equations closed by assuming certain relationships between unknown higher-order turbulence moments and the known lower-order variables. The model output variables are winds, potential temperature, mixing ratios of water vapor and liquid water, turbulence second moments, a turbulence length scale, and turbulence transport coefficients (eddy viscosity and eddy diffusivity). These results can be used as inputs to pollutant dispersion models. The model is time dependent and three-dimensional in space.

HOTMAC can be used under quite general conditions of flow and thermal stratification: methods for turbulence parameterization are more advanced than those in simple eddy viscosity models. The present model, combined with a statistical cloud model, has simulated interaction between water phase changes and basic dynamic variables. For example, computed turbulence energy increases substantially in the layers where condensation occurs. This appears reasonable, since the latent heat released by condensation produces local unstable layers, resulting in generation of turbulence. Effects of short- and long-wave solar radiation, tall tree canopies, and topography are also included in the model. Surface temperatures are computed from a heat conduction equation for the soil and a heat energy balance equation at the surface.

The present model assumes hydrostatic equilibrium and uses the Boussinesq approximation. Therefore, in theory, the model applications are limited to flows where the local acceleration and advection terms in the equation of vertical motion are much smaller than the acceleration due to gravity (hydrostatic equilibrium) and temperature variations in the horizontal are not too large (Boussinesq approximation).

The model has been used for a variety of fluid problems: surface boundary layer (Reference 16), atmospheric boundary layer, (Reference 17; Reference 18; Reference 19; Reference 20; Reference 21), airflow over tall tree canopies (Reference 22), air pollution transport (Reference 23), ocean boundary layer, (Reference 24), airflow over a cooling pond (Reference 25), laboratory flows (Reference 26), flow over complex terrain (Reference 27), and the results have been used in dispersion simulations over complex terrain (Reference 28; Reference 29; Reference 8), over the eastern half of the U.S. (Reference 30) and over the mountainous western U.S. (Reference 31). This model has also been used by others including Dobosy (Reference 32), Shaw (Reference 33), Burk (Reference 34), Miyakoda and Sirutis (Reference 35), Freeman (Reference 36), and Sun and Ogura (Reference 37). A complete summary of the model is given in a recent review paper (Reference 38).

The basic equations of HOTMAC for mean wind, temperature, mixing ratio of water vapor, and turbulence are similar to those used by Yamada in Reference 28 and Reference 39, except two improvements, the nested grid capability and effects of shadows produced by terrain, are added.

A terrain-following vertical coordinate system is used in order to increase the accuracy in the treatment of surface boundary conditions:

$$z^* = \bar{H} \frac{z - z_g}{H - z_g}, \quad (A - 1)$$

where  $z^*$  and  $z$  are the transformed and Cartesian vertical coordinates, respectively;  $z_g$  is ground elevation;  $\bar{H}$  is the material surface top of the model in the  $z^*$  coordinate; and  $H$  is the corresponding height in the  $z$ -coordinate.

The governing equations, following the coordinate transformation, are (Reference 28)

$$\begin{aligned} \frac{DU}{Dt} = & f(V - V_g) + g \frac{\bar{H} - z^*}{\bar{H}} \left( 1 - \frac{\langle \Theta_v \rangle}{\Theta_v} \right) \frac{\partial z_g}{\partial x} \\ & + \frac{\partial}{\partial x} \left( K_x \frac{\partial U}{\partial x} \right) + \frac{\partial}{\partial y} \left( K_{xy} \frac{\partial U}{\partial y} \right) + \frac{\bar{H}}{H - z_g} \frac{\partial}{\partial z^*} (-\bar{u}w) \end{aligned} \quad (A - 2)$$

$$\begin{aligned}
\frac{DV}{Dt} = & -f(U - U_g) + g \frac{\bar{H} - z^*}{\bar{H}} \left( 1 - \frac{\langle \Theta_v \rangle}{\Theta_v} \right) \frac{\partial z_g}{\partial y} \\
& + \frac{\partial}{\partial x} \left( K_{xy} \frac{\partial V}{\partial x} \right) + \frac{\partial}{\partial y} \left( K_y \frac{\partial V}{\partial y} \right) \\
& + \frac{\bar{H}}{H - z_g} \frac{\partial}{\partial z^*} (-\bar{v}w)
\end{aligned} \tag{A-3}$$

$$\frac{\partial U}{\partial x} + \frac{\partial V}{\partial y} + \frac{\partial W^*}{\partial z^*} - \frac{1}{H - z_g} \left( U \frac{\partial z_g}{\partial x} + V \frac{\partial z_g}{\partial y} \right) = 0 , \tag{A-4}$$

where

$$W^* \equiv \frac{\bar{H}}{H - z_g} W + \frac{z^* - \bar{H}}{H - z_g} \left( U \frac{\partial z_g}{\partial x} + V \frac{\partial z_g}{\partial y} \right) \tag{A-5}$$

and

$$\frac{D(\quad)}{Dt} \equiv \frac{\partial(\quad)}{\partial t} + U \frac{\partial(\quad)}{\partial x} + V \frac{\partial(\quad)}{\partial y} + W^* \frac{\partial(\quad)}{\partial z^*} . \tag{A-6}$$

In the above expressions,  $\langle \rangle$  indicates an average over a horizontal surface. The second terms on the right-hand side of Equations (A-2) and (A-3) indicate the effects of ground slope. For simplicity,  $H$  is specified as

$$H = \bar{H} + z_{gmax} , \tag{A-7}$$

where  $z_{gmax}$  is the maximum value of the ground elevation in the computational domain.

The geostrophic winds  $U_g$  and  $V_g$  are computed from Reference 28, i.e.,

$$\begin{aligned}
fU_g \equiv & fU_g(\bar{H}) \frac{\langle \Theta_v \rangle}{\langle \Theta_v(\bar{H}) \rangle} + g \frac{H - z_g}{\bar{H}} \int_{z^*}^{\bar{H}} \frac{1}{\langle \Theta_v \rangle} \frac{\partial}{\partial y} \Delta \Theta_v dz' \\
& - \frac{g}{\bar{H}} \frac{\partial z_g}{\partial y} \int_{z^*}^{\bar{H}} \frac{\Delta \Theta_v}{\langle \Theta_v \rangle} dz' ,
\end{aligned} \tag{A-8}$$

and

$$fV_g \equiv fV_g(\bar{H}) \frac{\langle \Theta_v \rangle}{\langle \Theta_v(\bar{H}) \rangle} - g \frac{H - z_g}{\bar{H}} \int_{z*}^{\bar{H}} \frac{1}{\langle \Theta_v \rangle} \frac{\partial \Delta \Theta_v}{\partial x} dz' \\ + \frac{g}{\bar{H}} \frac{\partial z_g}{\partial x} \int_{z*}^{\bar{H}} \frac{\Delta \Theta_v}{\langle \Theta_v \rangle} dz' , \quad (A-9)$$

where  $\Delta \Theta_v \equiv \Theta_v - \langle \Theta_v \rangle$ , and the abbreviated symbols  $U_g(\bar{H}) \equiv U_g(x, y, \bar{H}, t)$ ,  $V_g(\bar{H}) \equiv V_g(x, y, \bar{H}, t)$ , are used. The derivations of Equations (A-2) to (A-5), (A-8), and (A-9) are given in the Appendix of Reference 28. A turbulence kinetic energy equation is given by

$$\frac{D}{Dt} \left( \frac{q^2}{2} \right) = \frac{\partial}{\partial x} \left[ K_x \frac{\partial}{\partial x} \left( \frac{q^2}{2} \right) \right] + \frac{\partial}{\partial y} \left[ K_y \frac{\partial}{\partial y} \left( \frac{q^2}{2} \right) \right] \\ + \left( \frac{\bar{H}}{H - z_g} \right)^2 \frac{\partial}{\partial z*} \left[ q \ell S_q \frac{\partial}{\partial z*} \left( \frac{q^2}{2} \right) \right] \\ - \frac{\bar{H}}{H - z_g} \left( \overline{uw} \frac{\partial U}{\partial z*} + \overline{vw} \frac{\partial V}{\partial z*} \right) \\ + \beta g \overline{w \theta_v} - \frac{q^3}{B_1 \ell} , \quad (A-10)$$

and a turbulence length scale  $\ell$  is obtained from

$$\frac{D}{Dt} (q^2 \ell) = \frac{\partial}{\partial x} \left[ K_x \frac{\partial}{\partial x} (q^2 \ell) \right] + \frac{\partial}{\partial y} \left[ K_y \frac{\partial}{\partial y} (q^2 \ell) \right] \\ + \left( \frac{\bar{H}}{H - z_g} \right)^2 \frac{\partial}{\partial z*} \left[ q \ell S_\ell \frac{\partial}{\partial z*} (q^2 \ell) \right] \\ - \ell F_1 \left[ \frac{\bar{H}}{H - z_g} \left( -\overline{uw} \frac{\partial U}{\partial z*} - \overline{vw} \frac{\partial V}{\partial z*} \right) + \beta g \overline{w \theta_v} \right] \\ - \frac{q^3}{B_1} \left[ 1 + F_2 \left( \frac{\ell}{kz} \right)^2 \right] , \quad (A-11)$$

where  $q^2 = \overline{u^2} + \overline{v^2} + \overline{w^2}$  is twice the turbulence kinetic energy,  $\overline{w \theta_v}$  turbulence heat flux,  $\theta_v$  the fluctuation part of virtual potential temperature, and  $(F_1, F_2, S_q, S_\ell, \text{ and } B_1) =$

(1.8, 1.33, 0.2, 0.2, and 16.6), empirical constants determined from laboratory experiments (Reference 38). The internal heat energy equation is written as in Reference 8

$$\begin{aligned} \frac{D\Delta\Theta}{Dt} = \frac{\partial}{\partial x} \left[ K_x \frac{\partial\Delta\Theta}{\partial x} \right] + \frac{\partial}{\partial y} \left[ K_y \frac{\partial\Delta\Theta}{\partial y} \right] + \frac{\bar{H}}{H - z_g} \\ \times \left[ \frac{\partial}{\partial z^*} (-\overline{w\theta}) + \frac{1}{\rho C_p} \frac{\partial R_N}{\partial z^*} - W \frac{\partial\Theta_v}{\partial z^*} \right], \end{aligned} \quad (A-12)$$

The long-wave radiation flux  $R_N/\rho C_p$  is computed according to Sasamori (Reference 40). A conservation equation for mixing ratio of water vapor is given by

$$\frac{DQ_v}{Dt} = \frac{\partial}{\partial x} \left[ K_x \frac{\partial Q_v}{\partial x} \right] + \frac{\partial}{\partial y} \left[ K_y \frac{\partial Q_v}{\partial y} \right] + \frac{\bar{H}}{H - z_g} \frac{\partial}{\partial z^*} (-\overline{wq_v}). \quad (A-13)$$

The turbulent fluxes in Equations (A-2), (A-3), (A-10), (A-11), (A-12), and (A-13) are obtained from simplified second-moment turbulence-closure equations (Reference 27):

$$(\overline{uw}, \overline{vw}) = -\ell q \tilde{S}_M \left[ \frac{\partial U}{\partial z}, \frac{\partial V}{\partial z} \right] \quad (A-14a, b)$$

$$(\overline{w\theta}, \overline{wq_v}) = -\alpha \ell q \tilde{S}_M \left[ \frac{\partial \Theta}{\partial z}, \frac{\partial Q_v}{\partial z} \right] \quad (A-15a, b)$$

where  $\tilde{S}_M$  and  $\alpha$  are functions of the flux Richardson number, and  $\alpha (\equiv K_H/K_M$  where  $K_H$  is an eddy diffusivity coefficient and  $K_M$  is an eddy viscosity coefficient) is the reciprocal of the turbulent Prandtl number.

The expressions for  $\tilde{S}_M$  and  $\alpha$  were obtained from the Level 2 model of Mellor and Yamada (Reference 17) where temporal and spatial derivatives in Equation (A-10) are neglected. The readers are referred to Reference 19 for further discussions of the Level 2 model equations. The final expressions for  $\tilde{S}_M$  and  $\alpha$  are given in Reference 27 and are not repeated here.

## 2. Boundary Conditions

Surface boundary conditions for Equations (A-2), (A-3), and (A-10) to (A-13) are constructed from the empirical formulas by Dyer and Hicks (Reference 10) for the nondimensional wind and temperature profiles (see the Appendix of Reference 28). Strictly speaking, the formulas are valid only for horizontally homogeneous surfaces. It is assumed, however, that the same relations are fair approximations over nonhomogeneous terrain, provided that the formulas are applied sufficiently close to the surface. It should be noted that vegetation plays an active part in the apportionment of available heat energy between convective (sensible and latent) and conductive (into the soil) components. Use of the similarity formulas requires knowledge of the surface temperatures; a method to obtain the surface temperature is discussed below.

The temperature  $T_s$  in the soil layer is obtained by solving the heat conduction equation

$$\frac{\partial T_s}{\partial t} = \frac{\partial}{\partial z_s} \left( K_s \frac{\partial T_s}{\partial z_s} \right) , \quad (A-16)$$

where  $z_s$  is positive downward, and soil diffusivity  $K_s$  can be a function of soil moisture content. Appropriate boundary conditions for solution of Equation (A-16) are the heat energy balance at the soil surface and specification of the soil temperature or soil heat flux at a certain depth whose value is dependent on the duration of the integration. The heat energy balance at the surface is given by

$$R_s + R_L \downarrow - R_L \uparrow = H_s + LE + G_s , \quad (A-17)$$

where  $R_s$  is the incoming direct solar radiation absorbed by the surface,  $R_L \downarrow$  is the incoming long-wave radiation, and  $R_L \uparrow$  is the outgoing long-wave radiation.

The surface heat flux  $H_s$ , latent heat flux  $LE$ , and ground heat flux  $G_s$  are given by

$$H_s = -\rho_a c_p u_* T_* , \quad (A-18)$$

$$LE = -\rho_a L u_* Q_* , \quad (A-19)$$

and

$$G_s = K_s \left. \frac{\partial T_s}{\partial z_s} \right|_G , \quad (A-20)$$

where  $\rho_a$  is the air density,  $u_*$  is the friction velocity,  $T_*$  is the temperature scale,  $Q_*$  is the water vapor scale, and the subscript  $G$  denotes the value at the ground surface. Substituting Equations (A-18) to (A-20) into Equation (A-17) we obtain

$$R_s + \epsilon R_L \downarrow - \epsilon \sigma T_G^4 = -\rho_a c_p u_* T_* (1 + B^{-1}) - K_s \partial T_s / \partial z_s |_G , \quad (A-21)$$

where the relation

$$R_L \uparrow = \epsilon \sigma T_G^4 + (1 - \epsilon) R_L \downarrow , \quad (A-22)$$

and Bowen ratio

$$B = H_s / LE , \quad (A-23)$$

are used;  $\epsilon$  is the emissivity of the surface and  $\sigma$  is the Stefan-Boltzman constant. Garratt and Hicks (Reference 41) obtained a relationship between the surface temperature and air temperature at  $z_1$  (in the surface layer):

$$(\Theta(z_1) - \Theta_G) T_*^{-1} = (P_r / k) [(\ln\{(z_1 + z_{ot})/z_o\} + \ln(z_o/z_{ot}) - \psi] , \quad (A-24)$$

where  $P_r$  is the turbulence Prandtl number at neutral stability,  $k$  is the von Karman constant,  $z_o$  and  $z_{ot}$  are the roughness lengths for momentum and temperature, and  $\psi$  is the stability correction terms of Panofsky (Reference 42). A constant value of 0.1 m is assumed for  $z_o$ , and  $z_{ot}$  is obtained from a relationship  $\ln(z_o/z_{ot}) = 2$  (Reference 41). Using Equation (A-24) we can eliminate  $T_*$  from Equation (A-21) to obtain

$$R_s + \epsilon R_L \downarrow - \epsilon \sigma T_G^4 + m[\Theta(z_1) - T_G(P_o/P_G)^{R/c_p}] + K_s \left. \frac{\partial T_s}{\partial z_s} \right|_G = 0 , \quad (A-25)$$

where

$$m = k \rho_a c_p u_* (1 + B^{-1}) P_r^{-1} [\ln\{(z_1 + z_{ot})/z_o\} + 2 - \psi]^{-1} \quad (A-26)$$

$P_o$  is a reference pressure (1000 mb) and  $P_G$  is the pressure at the surface. Equation (A-25) may be linearized by noting that

$$(T_G^{n+1} - T_G^n)/T_G^n \ll 1$$

where the superscripts  $n$  and  $n+1$  denote the  $n$  and  $(n+1)^{th}$  time steps of integration (a typical time increment used in integration is 1 minute). After substitution into Equation (A-25) of the approximation

$$(T_G^{n+1})^4 \approx 4(T_G^n)^3 T_G^{n+1} - 3(T_G^n)^4 , \quad (A-27)$$

we obtain

$$\begin{aligned} & \left[ 4\epsilon \sigma (T_G^n)^3 + m(P_o/P_G)^{R/c_p} + \frac{K_s}{\Delta z_s} \right] T_G^{n+1} \\ &= \left( \frac{K_s}{\Delta z_s} \right) T_s^{n+1}(1) + R_s + \epsilon R_L \downarrow \\ &+ 3\epsilon \sigma (T_G^n)^4 + m\Theta^n(z_1) , \end{aligned} \quad (A-28)$$

where the derivative  $\partial T_s / \partial z_s|_G$  is replaced by a forward finite-difference approximation  $(T_s^{n+1}(1) - T_G^{n+1})/\Delta z_s$ ,  $T_s(1)$  is the soil temperature at the first grid level from the surface, and  $\Delta z_s$  is the distance between the surface and the first grid level in the soil layer.

Equation (A-16) is solved numerically in finite-difference form by Laasonen (Reference 11, p. 189). By this method Equation (A-16) reduces to  $AT_s = B$  where  $A$  is a



tridiagonal matrix and B is a column vector. The solution is conveniently obtained by using the relation (Reference 11, p. 198)

$$(T_s)_\ell = E_\ell(T_s)_{\ell+1} + F_1, \quad (A-29)$$

where  $(T_s)_\ell$  is the soil temperature at the  $\ell^{\text{th}}$  grid level from the surface. Expressions for  $E_\ell$  and  $F_\ell$  when  $\ell > 1$  are determined from the finite-difference form of Equation (A-16), and Equation (A-28) determines  $E_1$  and  $F_1$ . From Equations (A-28) and (A-29), we obtain

$$E_1 = \left( \frac{K_s}{\Delta z_s} \right) / \left[ 4\epsilon\sigma(T_G^n)^3 + m \left( \frac{P_o}{P_G} \right)^{R/c_p} + \frac{K_s}{\Delta z_s} \right], \quad (A-30)$$

and

$$F_1 = \frac{[R_s + \epsilon R_L \downarrow + 3\epsilon\sigma(T_G^n)^4 + m\Theta^n(z_1)]}{[4\epsilon\sigma(T_G^n)^3 + m \left( \frac{P_o}{P_G} \right)^{R/c_p} + \left( \frac{K_s}{\Delta z_s} \right)]}. \quad (A-31)$$

Numerical integration of Equation (A-16) by use of Equation (A-29) to Equation (A-31) is rapid since no iteration is required.

The incoming direct solar radiation flux to an inclined surface is obtained from Kondratyev (Reference 43):

$$R_s = R_o[A + B \cos \Omega + C \sin \Omega] \quad (A-32)$$

where

$$A = \cos \alpha \sin \phi \sin \delta + \sin \alpha [\cos \Psi_n (\tan \Phi \sin \Phi \sin \delta - \sin \delta \sec \Phi)] \quad (A-33a)$$

$$B = \cos \alpha \cos \Phi \cos \delta + \sin \alpha \cos \Phi \sin \Phi_n \cos \delta, \quad (A-33b)$$

and

$$C = \sin \alpha \cos \delta \sin \Phi_n. \quad (A-33c)$$

In the above expressions  $R_o$  is the near surface, direct solar radiation flux;  $\Omega$  is the solar hour angle, positive clockwise from apparent noon;  $\Phi$  is the latitude;  $\delta$  is the declination

of the sun;  $\alpha$  is the angle of inclination of the surface relative to the horizontal plane; and  $\Psi_n$  is the azimuth of the projection of the normal to the surface on the horizontal plane, as counted from the plane of the meridian (azimuth is considered positive when counted clockwise). Since the maximum change in the solar declination  $\delta$  in 24 hours is less than 0.5 degrees,  $\delta$  is assumed to be constant during a given day. Spencer (quoted in Reference 44, p. 63) provides a formula to compute  $\delta$  in radians,

$$\begin{aligned}\delta = & 0.006918 - 0.399912 \cos \theta_o + 0.070257 \sin \theta_o \\ & - 0.006758 \cos 2\theta_o + 0.000907 \sin 2\theta_o \\ & - 0.002697 \cos 3\theta_o + 0.001480 \sin 3\theta_o ,\end{aligned}\tag{34}$$

where the angle  $\theta_o$  in radians is related to the Julian day  $J_d$  by

$$\theta_o = \frac{2\pi(J_d - 1)}{365} .\tag{A - 35}$$

Equation (A-34) estimates  $\delta$  with a maximum error of 0.0006 radians. Solar hour  $\Omega$  can be obtained if the longitude, clocktime, and the equation of time are known. The equation of time is the difference between the local apparent time and a fixed mean solar time, which is derived from the motion of a celestial equation at a rate equal to the average movement of the sun. The solar hour angle  $\Omega$  is given in radians by

$$\Omega = \frac{\pi(t_s - 12)}{12} ,\tag{A - 36}$$

where  $t_s$  is the true solar time (local apparent time) in hours. The true solar time is obtained from

$$t_s = t_{c.t.} + \Delta t_{long} + t_{eq} ,\tag{A - 37}$$

where  $t_{c.t.}$ ,  $\Delta t_{long}$ , and  $t_{eq}$  are the clocktime, the longitude correction, and the equation of time, respectively. The longitude correction accounts for the difference between the local meridian and a standard meridian, and is positive if the local meridian is east of the

standard. The equation of time is provided by Spencer (quoted in Reference 44, p. 63) as follows;

$$t_{eq} = \frac{12}{\pi} (0.000075 + 0.001868 \cos \theta_o - 0.032077 \sin \theta_o - 0.014615 \cos 2\theta_o - 0.40849 \sin 2\theta_o) , \quad (A - 38)$$

where  $t_{eq}$  is in hours and  $\theta_o$  is defined by Equation (A-35). Equation (A-38) has a maximum error, compared with values tabulated in the National Almanac, of 35 s in time.

The amount of solar radiation reaching the surface is much less than that at the top of the atmosphere due to many factors, including molecular scattering and absorption by permanent gases such as oxygen, ozone, and carbon dioxide. The effect is parameterized by Atwater and Brown (Reference 45), who modified the original form by Kondratyev (Reference 46) to include the effect of the forward Rayleigh scattering. The expression is

$$G = 0.485 + 0.515 \left[ 1.041 - 0.16 \left( \frac{0.000949P + 0.051}{\cos Z} \right)^{1/2} \right] \quad (A - 39)$$

where  $P$  is pressure in *mb*. Other important factors that also modify the amount of incoming solar radiation include water vapor, clouds, and airborne particles. Parameterizations for these factors are not included in the present model.

Currently  $R_o$  in Equation (A-32) is calculated from

$$R_o = R_{\infty} G , \quad (A - 40)$$

where  $R_{\infty}$  is the incoming radiation flux at the top of the atmosphere and  $G$  is given by Equation (A-39).

The zenith angle  $Z$  in Equation (A-39) is determined from the following formula

$$\cos Z = \sin \Phi \sin \delta + \cos \Phi \cos \delta \cos \Omega . \quad (A - 41)$$

Finally,  $R_L \downarrow$ , the long-wave incoming radiation at the surface, is computed according to the following formula

$$R_L \downarrow = R_o \downarrow \cos \alpha \quad (A - 42)$$

where  $R_o \downarrow$  is the long-wave incoming radiation normal to horizontal surface and  $\alpha$  is the angle of inclination of a sloped surface given by

$$\alpha = \tan^{-1} \left[ \left( \frac{\partial z_g}{\partial x} \right)^2 + \left( \frac{\partial z_g}{\partial y} \right)^2 \right]^{1/2} . \quad (A - 43)$$

Boundary conditions for  $U, V, \Theta, Q_v, q$ , and  $\ell$  along the upper computational boundary are

$$(U, V) = (U_g, V_g), \quad (A - 44a, b)$$

where  $U_g$  and  $V_g$  are geostrophic wind components defined as

$$(U_g, V_g) = (1/f) \left( \frac{-\partial P}{\partial y}, \left( \frac{\partial P}{\partial x} \right) \right) . \quad (A - 45a, b)$$

Potential temperature and the mixing ratio are specified, and turbulence is assumed to vanish along the upper boundary. Soil temperature at 30 cm below the surface is also specified.

The lateral boundary values for  $U, V, \Theta, Q_v, q^2$ , and  $\ell$  are obtained by integrating the corresponding governing Equations (A-2), (A-3), (A-10), (A-11), (A-12), and (A-13), except that variations in the horizontal directions are all neglected. Variables  $U, V, q^2$ , and  $q^2 \ell$  are smoothed at each time step by using the values at four neighboring points, i.e.,

$$\Phi_{i,j} = (1 - \lambda) \Phi_{i,j} + 0.25 \lambda (\Phi_{i+1,j} + \Phi_{i-1,j} + \Phi_{i,j-1} + \Phi_{i,j+1}) , \quad (A - 46)$$

where  $\Phi$  represents either  $U$ ,  $V$ ,  $q^2$ , or  $q^2\ell$ , and  $\lambda = 0.5$  is used. A similar expression, but using only three neighboring points, is applied to the values at the lateral boundaries.

Two modifications have been made for use on a microcomputer. First, changes have been made in the code that destroy the effects of terrain slopes at the boundaries. This makes it possible to put the boundaries in very complex terrain without constructing an artificial apron around the area of interest. The second change was to force the first grid vertical cell to be at 4 meters aboveground. This change was to ensure that the lowest layer was sufficiently near the ground to generate the appropriate slope flows.

### 3. Initial Values

An initial wind profile at the southwestern corner of the computational domain is first constructed by assuming a logarithmic variation (initially  $u_* = 0.2$  m/s, and  $z_o = 0.1$  meters) from the ground up to the level where the wind speed reaches an ambient value (geostrophic wind). Initial wind profiles at other grid locations are obtained by scaling the southwestern corner winds to satisfy the mass continuity.

The vertical profile of potential temperature is initially assumed to increase linearly with height. Initial potential temperatures are assumed to be uniform in the horizontal directions. Initial values for water vapor are constructed by using the initial potential temperature profiles, pressure at the top of computational domain, and observed relative humidity. The turbulence kinetic energy and length scale are initialized by using the initial wind and temperature profiles and the relationships resulted from the Level 2 model. These expressions are already given by Yamada (Reference 19) and are not repeated here.

### 4. Numerical Integrations

The partial differential Equations (A-2), (A-3), and (A-10) to (A-13) are integrated by using the Alternating Direction Implicit (ADI) method, and a time increment is chosen to satisfy Courant-Friedrich-Lewy criteria. To increase the accuracy of finite-difference approximations, mean and turbulence variables are defined at grids that are staggered both in horizontal and vertical directions. Mean winds, temperatures, and wa-

ter vapor vary greatly with height near the surface. In order to resolve these variations, nonuniform grid spacings are used in the vertical direction.

#### B. RAPTAD (Random Particle Transport And Diffusion.)

A brief description of the RAPTAD model is given here. Locations of particles are computed from

$$x_i(t + \Delta t) = x_i(t) + U_{pi}\Delta t , \quad (A - 47)$$

where

$$U_{pi} = U_i + u_i , \quad (A - 48)$$

$$u_i(t + \Delta t) = au_i(t) + b\sigma_{u_i}\zeta + \delta_{i3}(1 - a)t_{Lx_i} \frac{\partial}{\partial x_i}(\sigma_{u_i}^2) , \quad (A - 49)$$

$$a = \exp(-\Delta t/t_{Lx_i}) , \quad (A - 50)$$

and

$$b = (1 - a^2)^{1/2} . \quad (A - 51)$$

In the above expressions,  $U_{pi}$  is the particle velocity in  $x_i$  direction,  $U_i$  mean velocity,  $u_i$  turbulence velocity,  $\zeta$  a random number from a Gaussian distribution with zero mean and unit variance,  $t_{Lx_i}$  the Lagrangian integral time for the velocity  $u_i$ ,  $\sigma_{u_i}$  variance of velocity fluctuation  $u_i$ , and  $\delta_{i3}$  is the Dirac delta. The last term on the right-hand side of Equation (A-49) was introduced by Legg and Raupach (Reference 47) to correct accumulation of particles in the low energy areas. The mean velocity  $U_i$  and vertical velocity variance  $\sigma_{u_i}$  are obtained from the hydrodynamic model results. The Lagrangian time scales,  $t_{Lz} = 20s$ ,  $t_{Lx} = 5000s$ , and  $t_{Ly} = 5000s$ , are used in this study.

In the previous studies (Reference 28; Reference 39), the concentration at a given time and location was determined by counting the number of particles in an imaginary

sampling volume. The computed concentration level could vary considerably, depending on the size of the sampling volume and number of particles used in the computation. For example, if the sampling volume is very small, the concentration distribution becomes noisy. On the other hand, if the sampling volume is too large, the concentration distribution will be oversmoothed (Reference 48). Theoretically, the sampling volume problem is eliminated by releasing an infinite number of particles in the computation. Of course, it is impossible in practice, or at least very expensive, to release an infinite number of particles.

A "kernel" density estimator is used in this study where each particle represents a center of a puff. Various functional forms can be assumed to express the concentration distribution in the puff. One of the simplest ways is to assume a Gaussian distribution where variances are determined as the time integration of the velocity variances encountered over the history of the puff. The concentration level at a given time and space is determined as the sum of the concentrations each puff contributes. The kernel method requires no imaginary sampling volumes and produces smooth concentration distribution with a much smaller number of particles than required for the previous particle method (Reference 47).

Concentration  $\chi$  at  $(X, Y, Z)$  is estimated by using the following expression:

$$\begin{aligned} \chi(X, Y, Z) = & \frac{Q\Delta t}{(2\pi)^{3/2}} \sum_{k=1}^N \frac{1}{\sigma_{x_k} \sigma_{y_k} \sigma_{z_k}} \exp\left(-\frac{1}{2} \frac{(x_k - X)^2}{\sigma_{x_k}^2}\right) \\ & \bullet \exp\left(-\frac{1}{2} \frac{(y_k - Y)^2}{\sigma_{y_k}^2}\right) \\ & \bullet \left[ \exp\left(-\frac{1}{2} \frac{(z_k - Z)^2}{\sigma_{z_k}^2}\right) + \exp\left(-\frac{1}{2} \frac{(z_k + Z - 2z_g)^2}{\sigma_{z_k}^2}\right) \right] \quad (A-52) \end{aligned}$$

where  $(x_k, y_k, z_k)$  is the location of  $k$  th particle;  $\sigma_{x_k}$ ,  $\sigma_{y_k}$  and  $\sigma_{z_k}$  are standard deviations of a Gaussian distribution; and  $z_g$  is the ground elevation. The variances are estimated based on Taylor's homogeneous diffusion theory (Reference 49). For example,  $\sigma_y$  is obtained from

$$\begin{aligned}\sigma_y^2 &= 2\sigma_v^2 \int_0^t \int_0^\zeta R(\zeta) d\zeta dt \\ &= 2\sigma_v^2 t_{Ly} \left( t + t_{Ly} \exp\left(-\frac{t}{t_{Ly}}\right) - t_{Ly} \right) ,\end{aligned}\quad (A-53)$$

where a correlation function  $R(\zeta) = \exp\left(-\frac{\zeta}{t_{Ly}}\right)$  is used. Equation (A-53) is approximated by

$$\sigma_y = \sigma_v t \quad \text{for } t \leq 2t_{Ly} , \quad (A-54a)$$

and

$$\sigma_y^2 = 2t_{Ly}\sigma_v^2 t \quad \text{for } t > 2t_{Ly} . \quad (A-54b)$$

Although the turbulence field under the study is not homogeneous, we assume the theory can be applicable over a short time period, such as an integration time step (10 seconds in this study). Therefore,

$$\sigma_y(t + \Delta t) = \sigma_y(t) + \sigma_v \Delta t \quad \text{for } t \leq 2t_{Ly} \quad (A-55a)$$

and

$$\sigma_y^2(t + \Delta t) = \sigma_y^2(t) + 2t_{Ly}\sigma_v^2 \Delta t \quad \text{for } t > 2t_{Ly} \quad (A-55b)$$

are used in this study.

In a similar fashion,

$$\sigma_x(t + \Delta t) = \sigma_x(t) + \sigma_u \Delta t \quad \text{for } t \leq 2t_{Lx} , \quad (A-56a)$$

$$\sigma_x^2(t + \Delta t) = \sigma_x^2(t) + 2t_{Lx}\sigma_u^2 \Delta t \quad \text{for } t > 2t_{Lx} , \quad (A-56b)$$

$$\sigma_z(t + \Delta t) = \sigma_z(t) + \sigma_w \Delta t \quad \text{for } t \leq 2t_{Lz} , \quad (A-57a)$$

and



$$\sigma_z^2(t + \Delta t) = \sigma_z^2(t) + 2t_{Lz}\sigma_w^2\Delta t \quad \text{for } t > 2t_{Lz} \quad , \quad (A - 57b)$$

where the standard deviations  $\sigma_u, \sigma_v$ , and  $\sigma_w$  at each particle location are obtained by interpolating grid values of a computation grid volume in which a particle is located.

## NUMERICAL PROCEDURES

### A. FINITE-DIFFERENCE EQUATIONS

The prognostic Equations (A-2), (A-3), (A-10), (A-11), (A-12), and (A-13) may be expressed in the following general form:

$$\frac{\partial \phi}{\partial t} = \Delta_x \phi + \Delta_y \phi + \Delta_z \phi - A\phi + F \quad (A-58)$$

where

$$\Delta_x \phi \equiv \frac{\partial}{\partial x} \left( K_1 \frac{\partial \phi}{\partial x} \right) - U \frac{\partial \phi}{\partial x} , \quad (A-59a)$$

$$\Delta_y \phi \equiv \frac{\partial}{\partial y} \left( K_2 \frac{\partial \phi}{\partial y} \right) - V \frac{\partial \phi}{\partial y} , \quad (A-59b)$$

$$\Delta_z \phi \equiv \frac{\partial}{\partial z} \left( K_3 \frac{\partial \phi}{\partial z} \right) - W \frac{\partial \phi}{\partial z} , \quad (A-59c)$$

and

$$\phi \equiv (U, V, \Theta_t, Q_w, q^2, q^2 \ell) . \quad (A-60)$$

The coefficient  $K_1$  represents the horizontal eddy viscosity coefficients  $K_x$  or  $K_{xy}$ . Similarly,  $K_2$  represents  $K_y$  or  $K_{xy}$ , and  $K_3$  represents the vertical eddy viscosity coefficients  $K_M$  or  $K_H$ . The fourth and fifth terms on the right-hand side of Equation (A-58) represent the variable to which the equation applies and external forcing functions, respectively. Table A-1 summarizes  $K_1, K_2, K_3, A$ , and  $F$  for the prognostic equations for  $U, V, \Theta_t, Q_w, q^2$ , and  $q^2 \ell$ .

The ADI method, developed by Peaceman and Rachford (Reference 50), has second-order accuracy for both space and time derivatives and is unconditionally stable. The ADI scheme has been extensively and successfully applied in the simulation of various one- and two-dimensional fluid dynamics problems (Reference 51, p. 95). Generalization of the scheme to a three-dimensional space, however, requires special consideration, as pointed out by Richtmyer and Morton (Reference 11, p. 212); otherwise, the unconditional stability is lost and accuracy drops to  $O(\Delta t) + O[(\Delta x)^2]$ .

TABLE A-1. COEFFICIENTS  $K_1, K_2, K_3, A$ , AND  $F$  IN EQUATION (A-58)

$\phi$	$K_1$	$K_2$	$K_3$	$A$	$F$
$U$	$K_x$	$K_{xy}$	$K_M$	0	$f(V - V_g) + g \frac{\bar{H} - z^*}{\bar{H}} \left( 1 - \frac{\langle \theta_v \rangle}{\theta_v} \right) \frac{\partial z_g}{\partial x}$
$V$	$K_{xy}$	$K_y$	$K_M$	0	$-f(U - U_g) + g \frac{\bar{H} - z^*}{\bar{H}} \left( 1 - \frac{\langle \theta_v \rangle}{\theta_v} \right) \frac{\partial z_g}{\partial y}$
$\Delta \Theta_\ell$	$K_x$	$K_H$	$K_H$	0	$\frac{\bar{H}}{\bar{H} - z_g} \left( \frac{1}{\rho C_p} \frac{\partial R_N}{\partial z^*} - w \frac{\partial \theta_v}{\partial z^*} \right)$
$Q_w$	$K_x$	$K_y$	$K_H$	0	0
$\frac{q^2}{2}$	$K_x$	$K_y$	$q\ell \tilde{S}_\ell$	$q/\wedge_1$	$-\frac{\bar{H}}{\bar{H} - z_g} \left( \overline{uw} \frac{\partial U}{\partial z^*} + \overline{vw} \frac{\partial V}{\partial z^*} \right) + \beta g \overline{w\theta_v}$
$q^2 \ell$	$K_x$	$K_y$	$q\ell \tilde{S}_\ell$	$q/\wedge_1 \times$ $\left[ 1 + F_2 \left( \frac{\ell}{k_z} \right)^2 \right]$	$\ell F_1 \frac{\bar{H}}{\bar{H} - z_g} \left( -\overline{uw} \frac{\partial U}{\partial z^*} - \overline{vw} \frac{\partial V}{\partial z^*} \right) + \beta g \overline{w\theta_v}$

The finite-difference version of Equation (A-58) may be written according to ADI method as

$$\frac{\phi^* - \phi^n}{\Delta t} = \frac{1}{2} \Delta_z (\phi^* + \phi^n) + \Delta_x \phi^n + \Delta_y \phi^n - A\phi^* + F, \quad (A-61)$$

$$\frac{\phi^{**} - \phi^n}{\Delta t} = \frac{1}{2} \Delta_z (\phi^* + \phi^n) + \frac{1}{2} \Delta_x (\phi^{**} + \phi^n) + \Delta_y \phi^n - A\phi^* + F, \quad (A-62)$$

and

$$\begin{aligned} \frac{\phi^{n+1} - \phi^n}{\Delta t} &= \frac{1}{2} \Delta_z (\phi^* + \phi^n) + \frac{1}{2} \Delta_x (\phi^{**} + \phi^n) \\ &\quad + \frac{1}{2} \Delta_y (\phi^{n+1} + \phi^n) - A\phi^* + F, \end{aligned} \quad (A-63)$$

where  $\phi^n$  and  $\phi^{n+1}$  are values at  $t = n\Delta t$  and  $(n+1)\Delta t$ , respectively, and  $\Delta t$  is a time increment of integration. The value represented by  $\phi^*$  and  $\phi^{**}$  are the first and second intermediate values necessary to obtain  $\phi^{n+1}$  from  $\phi^n$ . Richtmyer and Morton (Reference 11, p. 213) pointed out that if  $\phi^*$  in the vertical derivative term of Equation (A-63) is replaced by the most recent value  $\phi^{**}$ , then the unconditional stability is lost. The

amplification factor for the complete cycle given by Equations (A-61) to (A-63) is shown to be not greater than 1, indicating unconditional stability (Reference 11, p. 213).

Equations (A-62) and (A-63) may be simplified by subtracting Equation (A-61) from Equation (A-62) and subtracting Equation (A-62) from Equation (A-63), respectively. The resulting equations are

$$\frac{\phi^{**} - \phi^*}{\Delta t} = \frac{1}{2} \Delta_x (\phi^{**} - \phi^n) \quad (A-64)$$

and

$$\frac{\phi^{n+1} - \phi^{**}}{\Delta t} = \frac{1}{2} \Delta_y (\phi^{n+1} - \phi^n) . \quad (A-65)$$

Equations (A-61), (A-64), and (A-65) may be rewritten as

$$\left(1 + A\Delta t - \frac{\Delta t}{2} \Delta_x\right) \phi^* = \phi^n + \Delta t \left\{ \frac{1}{2} \Delta_x \phi^n + \Delta_x \phi^n + \Delta_y \phi^n + F \right\} \quad (A-66)$$

$$\left(1 - \frac{\Delta t}{2} \Delta_x\right) \phi^{**} = \phi^* - \frac{\Delta t}{2} \Delta_x \phi^n , \quad (A-67)$$

and

$$\left(1 - \frac{\Delta t}{2} \Delta_y\right) \phi^{n+1} = \phi^{**} - \frac{\Delta t}{2} \Delta_y \phi^n . \quad (A-68)$$

Equations (A-66) and (A-68) may be further transformed to the general form

$$-A_\ell \phi_{\ell-1} + B_\ell \phi_\ell - C_\ell \phi_{\ell+1} = D_\ell , \quad (A-69)$$

where  $\ell = i, j, k$  represents the  $i, j$ , and  $k$  th grid points in the  $x, y$ , and  $z$  directions, respectively. The space derivatives  $\Delta_x \phi$ ,  $\Delta_y \phi$ , and  $\Delta_z \phi$  are approximated by centered finite differences. Coefficients  $A_\ell, B_\ell, C_\ell$ , and  $D_\ell$  may be identified by comparing term by term the expanded forms of Equations (A-66) to (A-68) with those of Equation (A-69). The results are given in Table A-2. The coefficients  $a_i, b_j$ , and  $c_k$  are  $dX/dx, dY/dy$ , and  $dZ/dz^*$ , respectively, where  $(X, Y, Z)$  are grid coordinates, whose increments are one.

TABLE A-2. COEFFICIENTS  $A_\ell$ ,  $B_\ell$ ,  $C_\ell$ , and  $D_\ell$  FOR EQUATION (A-69).

---

$A_k$	$(c_k \Delta t / 2) \left\{ \frac{W_k^n}{2} + (cK_3)_{k-1/2} \right\}$
$C_k$	$(c_k \Delta t / 2) \left\{ \frac{-W_k^n}{2} + (cK_3)_{k+1/2} \right\}$
$B_k$	$1 + A_k + C_k + A \Delta t$
$D_k$	$\phi^n + \Delta t \left\{ \frac{1}{2} \Delta_z \phi^n + \Delta_x \phi^n + \Delta_y \phi^n + F \right\}$

---

$A_i$	$(a_i \Delta t / 2) \left\{ \frac{U_i^n}{2} + (aK_1)_i - 1/2 \right\}$
$C_i$	$(a_i \Delta t / 2) \left\{ \frac{-U_i^n}{2} + (aK_1)_i + 1/2 \right\}$
$B_i$	$1 + A_i + C_i$
$D_i$	$\phi_i^* - (\Delta t / 2) \Delta_x \phi^n$

---

$A_j$	$(b_j \Delta t / 2) \left\{ \frac{V_j^n}{2} + (bK_2)_{j-1/2} \right\}$
$C_j$	$(b_j \Delta t / 2) \left\{ \frac{-V_j^n}{2} + (bK_2)_{j+1/2} \right\}$
$B_j$	$1 + A_j + C_j$
$D_j$	$\phi_j^{**} - (\Delta t / 2) \Delta_y \phi^n$

---

Equation (A-69) may be expressed in the general form  $\mathcal{T}\phi = \mathcal{S}$ , where  $\mathcal{T}$  is a tridiagonal matrix whose elements are given by  $A_\ell$ ,  $B_\ell$ , and  $C_\ell$ , and  $\mathcal{S}$  is a column vector whose elements are given by  $D_\ell$ . Solutions for Equation (A-69), whose coefficient matrix is tridiagonal, are obtained by a direct elimination method (Reference 11, p. 200).

Accuracy of a finite-difference approximation is enhanced if more grid points are placed where the variables vary greatly with the coordinates. For example, wind, temperature, and water vapor are known to vary considerably with height in the surface layer. Those variables, however, vary much more slowly with height in the layers away from the surface. Thus, vertical grids are spaced linearly near the surface and parabolically away from the surface:

$$z = c_4 k \quad \text{for } k \leq k_t \quad (A - 70a)$$

$$z = c_1 k + c_2 k + c_3 \quad \text{for } k > k_t \quad (A - 70b)$$

where  $k$  is the vertical grid level whose increment is one and  $k_t$  is a transition level between the linear and parabolic variations. Constraints  $c_1, c_2, c_3$  and  $c_4$  are determined, depending on the problem to be solved.

In order to increase the accuracy of finite-difference approximations and to suppress computational noise whose wave length is  $2\Delta$ , where  $\Delta$  is a grid increment, mean and turbulence variables are defined on a staggered grid.

Figure A-1 shows relative locations of variables in a grid volume:  $U$  and  $V$  in Figure A-1a;  $\Theta_t$  and  $Q_w$  in Figure A-1b; and  $q^2$  and  $q^2\ell$  in Figure A-1c.

## B. BOUNDARY CONDITIONS

As shown by Mellor (Reference 16), our model simulated the surface layer data reported by Businger et al. (Reference 52) quite well. A rather coarse vertical grid spacing is necessary for three-dimensional modeling due to limitations of storage and time. Thus, in order to increase accuracy, empirical surface-layer parameterization is used for the first and second grid levels above the ground. Wind, temperature, and water vapor profiles in the surface layer may be approximated by the following formulas:

$$\frac{|\tilde{V}(z)|}{u_*} = \frac{1}{k} [\ln\{(z + z_o)/z_o\} - \psi_m(\zeta)] , \quad (A - 71)$$

$$\frac{\Theta_t(z) - \Theta_t(0)}{T_*} = \frac{P_r}{k} [\ln\{(z + z_{ot})/z_{ot}\} - \psi_h(\zeta)] , \quad (A - 72)$$

$$\frac{Q_w(z) - Q_w(0)}{Q_*} = \frac{S_c}{k} [\ln\{(z + z_{ov})/z_{ov}\} - \psi_v(\zeta)] , \quad (A - 73)$$

$$q^2(z) = B_1^{2/3} u_*^2 (\phi_m - \zeta)^{2/3} , \quad (74)$$

and

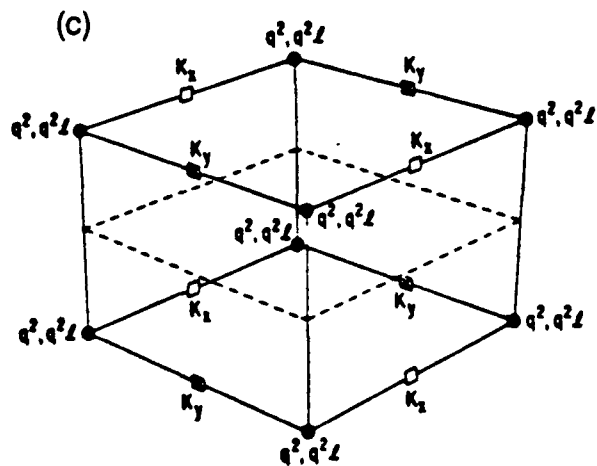
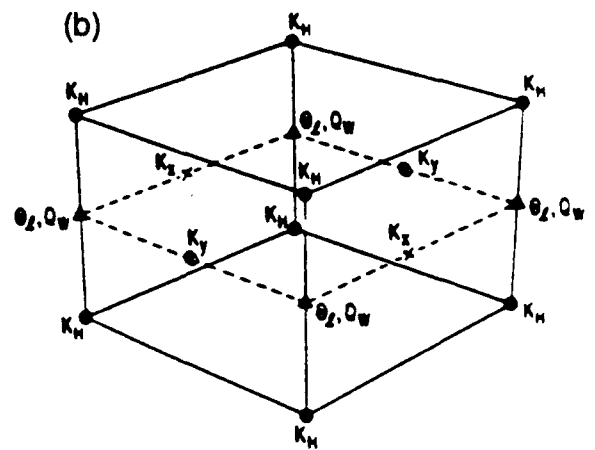
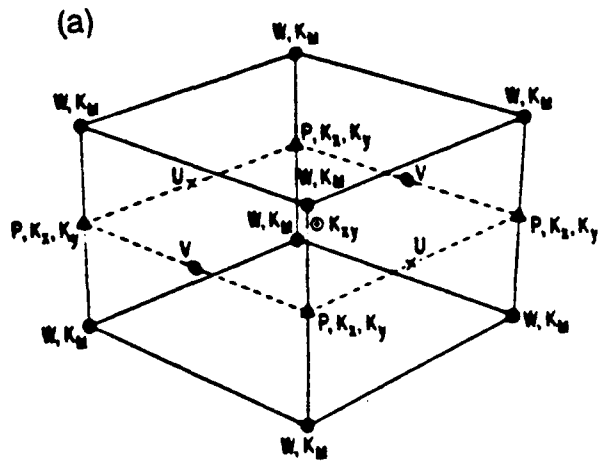


Figure A-1. Relative Locations of Mean and Turbulence Variables in the Computational Grid:  
 (a)  $U$  and  $V$ , (b)  $\Theta_L$  and  $Q_w$ , and (c)  $q^2$ , and  $q_L^2$ .

$$q^2 \ell(z) = kzq^2(z) . \quad (A - 75)$$

In the above equations,  $\mathcal{V}(z)$ ,  $\Theta_\ell(z)$ , and  $Q_w(z)$  are the abbreviations for  $\mathcal{V}(x, y, z, t)$ ,  $\Theta_\ell(x, y, z, t)$ , and  $Q_w(x, y, z, t)$ , respectively, and  $|\mathcal{V}|$  is the horizontal wind speed  $(U^2 + V^2)^{1/2}$ . Terms  $u_*$ ,  $T_*$ , and  $Q_*$ , defined as  $u_* \equiv \sqrt{\tau/\rho}$ ,  $T_* \equiv H/\rho c_p u_*$  and  $Q_* \equiv E/\rho u_*$ , are friction velocity and scales for temperature and water vapor, respectively. Terms  $\rho$ ,  $H$ , and  $E$  are surface stress, total sensible heat, and rate of evaporation, respectively; total sensible heat being defined as  $H = \overline{w\theta_v} = (1 + 0.61Q_w)\overline{w\theta} + 0.61\overline{wq_w}$ . The parameter  $\zeta$  is a nondimensional height  $z/L$ , where  $L$  is the Obukhov length -  $u_*^3/k\beta gH$ ;  $k$  is the von Karman constant;  $z_o$ ,  $z_{ot}$ , and  $z_{ov}$  are roughness lengths for wind, temperature, and water vapor, respectively; and  $P_r$  and  $S_c$  are the turbulence Prandtl and Schmidt numbers, respectively. Terms  $\psi_m$ ,  $\psi_h$ , and  $\psi_v$  (Reference 42) are correction terms for the atmospheric stability, and their functional forms are given by

$$\psi_m(\zeta) = \int_0^\zeta \left( \frac{1 - \phi_m(\zeta')}{\zeta'} \right) d\zeta' , \quad (A - 76)$$

$$\psi_h(\zeta) = \int_0^\zeta \left( \frac{1 - \phi_h(\zeta')}{\zeta'} \right) d\zeta' , \quad (A - 77)$$

and

$$\psi_v(\zeta) = \int_0^\zeta \left( \frac{1 - \phi_v(\zeta')}{\zeta'} \right) d\zeta' , \quad (A - 78)$$

where  $\phi_m$ ,  $\phi_h$ ,  $\phi_v$  are nondimensional wind, temperature, and water vapor gradients, respectively. The following formulations (Reference 53; Reference 10) are used for  $\phi_m$ ,  $\phi_h$ , and  $\phi_v$  under unstable conditions,

$$\phi_m(\zeta) \equiv \frac{kz}{u_*} \frac{\partial U}{\partial z} = (1 - 15\zeta)^{-1/4} , \quad (A - 79)$$

$$\phi_h(\zeta) \equiv \frac{kz}{T_*} \frac{\partial \Theta_\ell}{\partial z} = (1 - 15\zeta)^{-1/2} , \quad (A - 80)$$

and

$$\phi_v(\zeta) \equiv \frac{kz}{Q_*} \frac{\partial Q_w}{\partial z} = (1 - 15\zeta)^{-1/2} . \quad (A - 81)$$



For stable conditions,

$$\phi_m(\zeta) = \phi_h(\zeta) = \phi_v(\zeta) = 1 + 5\zeta \quad (A - 82a, b, c)$$

The roughness lengths  $z_o$ ,  $z_{ot}$ , and  $z_{ov}$  are specified over land and are computed over water according to the following formulas:

$$z_o = \frac{\gamma u_*^2}{g} \quad (A - 83a)$$

$$z_{ot} = \frac{\alpha}{ku_*} \quad (A - 83b)$$

and

$$z_{ov} = \frac{\eta}{ku_*} \quad (A - 83c)$$

(see Reference 54; Reference 55), where  $\gamma$  is a constant whose numerical value varies from 0.008 to 0.032 for water surfaces varying from a lake to a rough ocean and  $\alpha$  and  $\eta$  are the molecular diffusivities for heat and water vapor, respectively. Integrations of Equations (A-76) to (A-78) may be performed easily (Reference 55). The scales  $u_*$ ,  $T_*$ , and  $Q_*$  may be obtained by solving iteratively Equations (A-71) to (A-81) under unstable conditions. Solutions may be obtained without iteration for stable conditions over land. Iterations are required over the water, however, since the roughness heights are also functions of  $u_*$ , as seen in Equations (A-82a-c.)

Solutions of Equation (A-69) may be obtained using the boundary conditions discussed above and following the algorithms described by Richtmyer and Morton (Reference 11, p. 200). Solutions are assumed to be given by a relation

$$\phi_\ell = E_\ell \phi_{\ell+1} + F_\ell \quad (A - 84)$$

where  $E_\ell$  and  $F_\ell$  are determined from

$$E_\ell = \frac{C_\ell}{B_\ell - A_\ell E_{\ell-1}}, \ell > 1, \quad (A - 85a)$$

$$F_\ell = \frac{D_\ell + A_\ell F_{\ell-1}}{B_\ell - A_\ell E_{\ell-1}}, \ell > 1, \quad (A-85b)$$

where coefficients  $A_\ell, B_\ell, C_\ell$ , and  $D_\ell$  are given in Table A-2. The first values  $E_1$  and  $F_1$  may be determined from the surface boundary conditions given by Equations (A-71) and (A-75). For example, for  $\mathcal{V}$  and  $\Theta_\ell$ ,

$$\mathcal{V}(z_1) = \frac{\ln\{(z_1 + z_o)/z_o\} - \psi_m(\zeta_1)}{\ln\{(z_2 + z_o)/z_o\} - \psi_m(\zeta_2)} \mathcal{V}(z_2) \quad (A-86)$$

and

$$\begin{aligned} \Theta_\ell(z_1) = & \frac{\ln\{(z_1 + z_{ot})/z_{ot}\} - \psi_h(\zeta_1)}{\ln\{(z_2 + z_{ot})/z_{ot}\} - \psi_h(\zeta_2)} \Theta_\ell(z_2) \\ & + \left[ 1 - \frac{\ln\{(z_1 + z_{ot})/z_{ot}\} - \psi_h(\zeta_1)}{\ln\{(z_2 + z_{ot})/z_{ot}\} - \psi_h(\zeta_2)} \right] \Theta_\ell(0) \end{aligned} \quad (A-87)$$

where  $z_1$  and  $z_2$  are the first and second grid levels above the surface, respectively. Comparison between Equation (A-84) and Equation (A-86), where  $\phi = \mathcal{V}$ , yields

$$E_1 = \frac{\ln\{(z_1 + z_o)/z_o\} - \psi_m(\zeta_1)}{\ln\{(z_2 + z_{ot})/z_{ot}\} - \psi_h(\zeta_2)} \quad (A-88a)$$

and

$$F_1 = 0. \quad (A-88b)$$

Similarly, comparison between Equation (A-84) and Equation (A-87), where  $d = R$ , yields

$$E_1 = \frac{\ln\{(z_1 + z_{ot})/z_{ot}\} - \psi_h(\zeta_1)}{\ln\{(z_2 + z_{ot})/z_{ot}\} - \psi_h(\zeta_2)} \quad (A-89a)$$

and

$$F_1 = (1 - E_1) \Theta_\ell(0). \quad (A-89b)$$

Similar expressions as in Equations (A-89a) and (A-89b) are valid for  $Q_w$ , except that  $z_{ot}$  is replaced by  $z_{ov}$ . When boundary values are specified, as in the case of  $q^2$  and  $q^2\ell$

[Equations (A-74) and (A-75)],  $E_1$  and  $F_1$  are easily obtained. By comparing Equation (A-84) with Equation (A-74) we obtain for  $q^2$

$$E_1 = 0 \quad (A - 90a)$$

and

$$F_1 = B_1^{2/3} u_*^2 (\phi_m - z_1/L)^{2/3} . \quad (A - 90b)$$

Similarly, by comparing Equation (A-84) with Equation (A-75) we obtain for  $q^2 \ell$

$$E_1 = 0 \quad (A - 91a)$$

and

$$F_1 = k z_1 q^2 (z_1) . \quad (A - 91b)$$

Once  $E_1$  and  $F_1$  are determined as described above,  $E_\ell$  and  $F_\ell (\ell > 1)$  may be computed according to Equations (A-85a) and (A-85b), respectively. Then solutions may be computed from Equation (A-84), provided the value at the upper boundary is determined from upper boundary conditions as follows. The boundary conditions at the top are assumed to be

$$U = U_g(\bar{H}); \quad V = V_g(\bar{H}) , \quad (A - 92a, b)$$

$$\Theta = \Theta(\bar{H}) , \quad (A - 93)$$

$$Q_w = Q_w(\bar{H}) = 0 , \quad (A - 94)$$

$$q^2 = 0 , \quad (A - 95)$$

and

$$q^2 \ell = 0 . \quad (A - 96)$$

At lateral boundaries, wind, temperature, water vapor,  $q^2$ , and  $q^2 \ell$  are computed from the one-dimensional versions of the corresponding Equations (A-2), (A-3), (A-10), (A-11), (A-12), and (A-13).

## REFERENCES

1. Stephens, J. B., and Stewart, R. B., Rocket Exhaust Effluent Modeling for Tropospheric Air Quality and Environmental Assessments, NASA TR R-473, 1977.
2. Bowman, C. R., and Bjorklund, J. R., User's Manual for the REEDM Computer Program for Launches at Vandenberg Air Force Base, Volumes 1 and 2, H. E. Cramer Company Technical Report TR-85-157-01. Prepared for Department of the Air Force, Eastern Space and Missile Center/AFSC, Patrick AFB, Florida, 1985.
3. Haugen, D. A., and Fuquay, J. J., editors, The Ocean Breeze and Dry Gulch Diffusion Programs, Volumes 1 and 2, AFCRL-63-791 (I, II), Air Force Cambridge Research Laboratories, Hanscom AFB, MA, 1963.
4. Hinds, W. T., and Nickola, P. W., The Mountain Iron Diffusion Program: Phase I South Vandenberg: Volume I, AEC Research Development Report, Pacific Northwest Laboratory, Richland, WA, AFWTR-TR-67-1, BNWL-572, Vol. 1, 1967.
5. Hinds, W. T., and Nickola, P. W., The Mountain Iron Diffusion Program: Phase I South Vandenberg: Volume II, AEC Research Development Report, Pacific Northwest Laboratory, Richland, WA, AFWTR-TR-67-1, BNWL-572, Vol. II, 1968.
6. Daubek, H. G., Dotson, W. L., Ramsdell, J. V., and Nickola, P. W., The Mountain Iron Diffusion Program, Phase II: South Vandenberg: Volume III, Pacific Northwest Laboratory, Richland, WA, AFWTR-TR-67-1, BNWL-572 (III) UC-53, 1969.
7. Kunkel, B. A., User's Guide for the Air Force Toxic Chemical Dispersion Model (AFTOX), AFGL-TR-88-0009, Hanscom AFB, MA, 1988.
8. Yamada, T., and Bunker, S., "A Numerical Model Study of Nocturnal Drainage Flows with Strong Wind and Temperature Gradients," J. of Appl. Meteor., **28**, 545-554, 1989.
9. Thykier-Nielsen, S., and Mikkelsen, T., "Modelling of Flow and Dispersion in a Coastal Area," Proceedings from a EURASAP Conference, Workshop III on the Øresund Experiment. Risø National Laboratory, Denmark, October 25-27, 1988.
10. Dyer, A. J. and Hicks, B. B., "Flux-Gradient Relationships in the Constant Flux Layer," Quart. J. Roy. Meteor. Soc., **96**, 715-721, 1970.
11. Richtmyer, R. D. and Morton, K. W., Difference Methods for Initial-Value Problems, Second Ed., Interscience Publishers, J. Wiley and Sons, New York, 405 pp., 1967.

12. Hunter, S. M., Winds on Critical Streamline Surfaces (WOCSS) Model – An Evaluation Using Vandenberg AFB Terrain and Meteorological Data, Risø National Laboratory, Denmark, 1988.
13. Thykier-Nielsen, S., Mikkelsen, T., Larsen, S. E., Troen I., de Baas, A. F., Kamada, R., Skupniewicz C., and Schacher, G., "A Real time Puff-model for Accidental Releases in Complex Terrain," Proceedings of 2nd International Real Time Workshop, CEC, Luxemborg, May 16-19, 1989.
14. Hanna, S. R., Briggs, G. A., and Hosker, R. P. Jr., Handbook on ATMOSPHERIC DIFFUSION Technical Information Center, U. S. Department of Energy, Oak Ridge, TN, 101 pp., 1982.
15. Gaffen, D. J., Benocci, C., and Olivari, D., "Numerical Modeling of Buoyancy Dominated Dispersal Using Lagrangian Approach," Atmos. Environ., 21, 1285-1293, 1987.
16. Mellor, G. L., "Analytic Predictions of the Properties of Stratified Planetary Surface Layers," J. Atmos. Sci., 30, 1061-1069, 1973.
17. Mellor, G. L. and Yamada, T., "A Hierarchy of Turbulence-Closure Models for Planetary Boundary Layers," J. Atmos. Sci., 31, 1791-1806. Corrigendum, J. Atmos. Sci., 34, 1482, 1974.
18. Yamada, T. and Mellor, G. L., "A Simulation of the Wangara Atmospheric Boundary Layer Data," J. Atmos. Sci., 32, 2309-2329, 1975,.
19. Yamada, T., "The Critical Richardson Number and the Ratio of the Eddy Transport Coefficients Obtained From a Turbulence Closure Model," J. Atmos. Sci., 32, 926-933, 1975.
20. Yamada, T. and Mellor, G. L., "A Numerical Simulation of the BOMEX Data Using a Turbulence Closure Model Coupled with Ensemble Cloud Relations," Quart. J. Roy. Meteor. Soc., 105, 915-944, 1979.
21. Yamada, T. and Kao, C.-Y. J., "A Modeling Study on the Fair Weather Marine Boundary Layer of the GATE," J. Atmos. Sci., 43, 3186-3199, 1986.
22. Yamada, T., "A Numerical Model Study of Turbulent Airflow In and Above a Forest Canopy," J. Meteor. Soc. Japan, 60, 439-454, 1982.
23. Yamada, T., "A Numerical Simulation of Pollutant Dispersion in a Horizontally-Homogeneous Atmospheric Boundary Layer," Atmos. Environ., 11, 1015-1024, 1977.

24. Mellor, G. L. and Durbin, P. A., "The Structure and Dynamics of the Ocean Surface Mixed Layer," J. Phys. Oceanogr., 5, 718, 1975.
25. Yamada, T., "An Application of a Three-Dimensional Simplified Second-Moment Closure Numerical Model to Study Atmospheric Effects of a Large Cooling-Pond," Atmos. Environ., 13, 693-704, 1979.
26. Briggs, M. S., Mellor, G. L., and Yamada, T., "A Second Moment Turbulence Model Applied to Fully Separated Flows," in Project Squid Workshop on Turbulence in Internal Flows: Turbomachinery and Other Applications, S.N.B. Murthy (Ed.) Hemisphere Publishing Corporation, Washington, 249-281, 1977.
27. Yamada, T., "Simulations of Nocturnal Drainage Flows by a  $q^2$  Turbulence Closure Model," J. Atmos. Sci., 40, 91-106, 1983.
28. Yamada, T., "A Numerical Simulation of Nocturnal Drainage Flow," J. Meteor. Soc. Japan, 59, 108-122, 1981.
29. Yamada, T. and Bunker, S., "Development of a Nested Grid, Second-Moment Turbulence-Closure Model and an Application to the 1982 ASCOT Brush Creek Data Simulation," J. Atmos. Sci., 27, 562-578, 1988.
30. Kao, C.-Y. J., and Yamada, T., "Use of the CAPTEX Data for Evaluations of a Long-Range Transport Numerical Model with a Four-Dimensional Data Assimilation Technique," Mon. Weath. Rev., 116, 292-306, 1988.
31. Yamada, T., Kao, C.-Y. J., and Bunker, S., "Air Flow and Air Quality Simulations Over the Western Intermountainous Region with a Four-Dimensional Data Assimilation Technique," Atmos. Environ., 23, 539-554, 1987.
32. Dobosy, R., "Dispersion of Atmospheric Pollutants in Flow Over the Shoreline of a Large Body of Water," J. Appl. Meteor., 18, 117-132, 1979.
33. Shaw, R. H., "Secondary Wind Speed Maxima Inside Plant Canopies," J. Appl. Meteor., 16, 514-521, 1977.
34. Burk, S. D., "The Moist Boundary Layer with a Higher Order Turbulence Closure Model," J. Atmos. Sci., 34, 629-638, 1977.
35. Miyakoda, K. and Sirutis, J., "Comparative Integrations of Global Models with Various Parameterized Processes of Subgrid Scale Vertical Transports: Descriptions of the Parameterization," Beitr. Phys. Atmos., 50, 445-487, 1977.

36. Freeman, B. E., "Tensor Diffusivity of a Trace Constituent in a Stratified Boundary Layer," J. Atmos. Sci., 34, 124-136, 1977.
37. Sun, W. Y. and Ogura, Y., "Boundary-Layer Forcing as a Possible Trigger to a Squall-Line Formation," J. Atmos. Sci., 36, 235-254, 1979.
38. Mellor G. L. and Yamada, T., "Development of a Turbulence Closure Model for Geophysical Fluid Problems," Rev. Geophys. Space Phys., 20, 851-875, 1982.
39. Yamada, T., "Numerical Simulations of the Night 2 Data of the 1980 ASCOT Experiments in the California Geysers Area," Arch. Met. Geoph., Ser. A34, 223- 247, 1985.
40. Sasamori, T., "The Radiative Cooling Calculation for Application to General Circulation Experiments," J. Appl. Meteor., 7, 721-729, 1968.
41. Garratt, J. R. and Hicks, B. B., "Momentum, Heat and Water Vapour Transfer To and From Natural and Artificial Surfaces," Quart. J. Roy. Meteor. Soc., 99, 680-687, 1973.
42. Panofsky, H. A., "Determination of Stress from Wind and Temperature Measurements," Quart. J. Roy. Meteor. Soc., 23, 495-502, 1963.
43. Kondrat'yev, K. Ya., "Radiation Regime of Inclined Surfaces," WMO, Technical Note No. 15, Secretariat of the World Meteorological Organization, Geneva, Switzerland, 82 pp., 1977.
44. Paltridge, G. W. and Platt, C. M. R., Radiative Processes in Meteorology and Climatology, Elsevier Scientific Publishing Company, New York, 1976.
45. Atwater, M. A. and Brown, P. S. Jr., "Numerical Calculation of the Latitudinal Variation of Solar Radiation for an Atmosphere of Varying Opacity," J. Appl. Meteor., 13, 289-297, 1974.
46. Kondrat'yev, K. Ya., Radiation in the Atmosphere, Academic Press, New York, 1969.
47. Legg, R. J. and Raupach, M. F., "Markov-Chain Simulation of Particle Dispersion in Inhomogeneous Flows: The Mean Drift Velocity Induced by a Gradient in Eulerian Velocity Variance," Boundary-Layer Met., 24, 3-13, 1982.

48. Yamada, T., Bunker, S., and Niccum, E., "Simulations of the ASCOT Brush Creek Data by a Nested-Grid, Second-Moment Turbulence-Closure Model and a Kernal Concentration Estimator," Proceedings of the Fourth Conference on Mountain Meteorology, Seattle, WA, Aug. 25-28, p. 175-179, 1987.
49. Taylor, G. I., "Diffusion by Continuous Movements," Proceedings of the London Mathematical Society, Ser. 2, 20, 196-211, 1921.
50. Peaceman, D. W. and Rachford, H. H. Jr., "The Numerical Solution of Parabolic and Elliptic Differential Equations," SIAM J. Appl. Math., 3, 28-41, 1955.
51. Roache, P. J., Computational Fluid Dynamics, Hermosa Publishers, Albuquerque, New Mexico, 434 pp., 1972.
52. Businger, J. A., Wyngaard, J. C., Izumi, Y., and Bradley, E. F., "Flux Profile Relationships in the Atmospheric Surface Layer," J. Atmos. Sci., 28, 181-189, 1971.
53. Businger, J. A., "Transfer of Momentum and Heat in the Planetary Boundary Layer," Proc. Symp. on the Arctic Heat Budget and Atmospheric Circulation, J. P. Feltcher, Ed., Jan. 31-Feb.4, Lake Arrowhead, California, The Rand Corp., Santa Monica, Calif., Memorandum RM-5233-NSF, 1966.
54. Sverdrup, H. U., "Evaporation from the Oceans," Compendium of Meteorology, Waverly Press, Baltimore, 1071-1081, 1951.
55. Sheppard, P. A., "Transfer Across the Earth's Surface and Through the Air Above," Quart. J. Roy. Meteor. Soc., 84, 205-224, 1958.
56. Paulson, Ca. A., "The Mathematical Representation of Wind Speed and Temperature Profiles in the Unstable Atmospheric Surface Layer," J. Appl. Meteor., 9, 857-861, 1970.